PHASE-FIELD MODELING ON SHEAR BANDING IN AMORPHOUS ALLOYS WITH IMPROVED DUCTILITY

ZHANG HONGYING

Ph.D

The Hong Kong Polytechnic University

2013

The Hong Kong Polytechnic University

Department of Mechanical Engineering

Phase-Field Modeling on Shear Banding in Amorphous Alloys with Improved Ductility

by

ZHANG HONGYING

A thesis submitted in partial fulfillment of the requirements for the degree of Doctor of Philosophy

May 2013

CERTIFICATE OF ORIGINALITY

I hereby declare that this thesis is my own work and that, to the best of my knowledge and belief, it reproduces no material previously published or written, nor material that has been accepted for the award of any other degree or diploma, except where due acknowledgement has been made in the text.

_____ (Signed)

Zhang Hongying (Name of student)

This dissertation is dedicated to my parents and loving Yexin!

Abstract

Metallic glasses (MGs) have attracted scientific and technological attention due to their excellent physical, mechanical and chemical properties. Although the brittle nature of bulk metallic glasses (BMGs) limits their practical applications, it has been found that some new kinds of amorphous alloys show improved ductility through introducing the pores or secondary phases in their microstructures. The improved ductility is also observed in MGs with decreasing sample sizes. To date, the mechanisms governing the improved ductility in those MG systems are still under debate. Thus for the design of MGs for engineering applications, it is urgent to explore the mechanisms of the improved ductility. In this work, we use the phase-field modeling methods to study the origin of improved ductility in porous BMGs, *in-situ* formed BMG matrix composites and nano-sized MGs which are typical MG systems showing ductility.

Through simulations on the plastic deformation in porous BMGs, we found that the pore with much smoother surface can detour the incident shear bands, resulting in the improved ductility. On the other hand, adiabatic shear banding occurs when the pores

are not filled with gas or are in vacuum, avoiding the brittle failure due to the generation and multiplication of new shear bands.

The development of the *in-situ* formed BMG matrix composites containing dendrite microstructures is another outstanding advancement of the applications of the metallic glasses. In this work, the effects of two factors of the dendrites, i.e., the rotation angle representing the dispersion pattern and the fracture energy of such crystalline phase, on the plastic deformation of BMG composites are discussed. It is observed that the tips of the dendrite play a major role in the bifurcation and detour of the shear bands when the rotation angle is from 0° to 15°. It is found that the dendrite with high fracture energy can achieve high crack resistance and then cause more obvious bifurcation and detour of the shear bands, while the ones with lower fracture energy can cause more fracture area (both in matrix and in crystalline phases) to absorb more strain energy, which could result in improved ductility of the BMG composites. These features observed from simulation are useful in explaining the mechanisms of the improved ductility in the BMG composites and are also helpful in guiding the design of those composites for engineering applications.

Besides, the improved ductility and mechanical strength are also observed in the simulation when the size of the sample decreases, especially to the nano-scale (20 nm - 200 nm). Furthermore, some meaningful features and phenomena such as the emergence of necking and ductility during deformation are revealed from the simulated results and are found to be consistent with the experimental results. In this work, we elucidate two factors that lead to the size effect on the mechanical properties of MG nanowires, i.e., the fractions of initial deformation defects in the nanowire interior and on the nanowire surfaces. With the decreasing diameter, it is noted that the initial states of the deformation defects on the surfaces which are difficult to be quantitatively measured by experiments, play an important role in the deformation of MG nanowires. Based on the results of simulations, the Hall-petch like relation between the fracture strengths and the sample diameters are derived, which can well explain the discrepancies among the previous reports in literatures.

Acknowledgement

I am glad to announce that I have completed my Ph.D thesis here, and sincerely appreciate those who helped me in my academic life. First of all, I would like to acknowledge my academic supervisor, Dr. Guangping Zheng, for his great encouragement, continuous support, and invaluable guidance throughout my whole Ph.D study. Dr.G.P. Zheng is an excellent scholar, his precise manner and great perseverance in research set a good example for me and have a strong influence on my future career.

Secondly, I would like to acknowledge the members, such as SHEN Ying and LI Yuekai in our research team. Just the discussion and technology assistance help and encourage me conquer several research issues. I would like to thank all of my friends, such as YANG Lijun, LI Xiaoyan, LIN Yufeng, LIU zhiyuan, and CHAN Wailun for their warm friendship. It is that the friendship makes my PhD life colorful.

Last but not least, I would like to express my deepest appreciation to my family for their tremendous support and love.

Table of contents

List of Figures

Chapter 1 Introduction

Metallic glasses (MGs) have attracted scientific and technological attention since the development of $Au_{25}Si_{75}$ MG using the rapid cooling method by Pol Duwez [Klement et al. 1960]. Unlike crystalline solids, the structure of metallic glass is topologically disordered without any translational or orientational long-range order. The chemical, physical and mechanical properties due to the random close packing atomic structure are promising for further potential applications. Some industrial applications are shown in Figure 1.1. Among them, making golf plate may be the first step for the application of MGs in the business field as shown in Figure 1.1 (d) [Johnson 1998; Inoue 2005]. Their low elastic modulus and the lower vibrational response could favor controlling the ball. It could also be useful in surgery implant due to their good biocompatibility and easy forming into desired shapes, as shown in Figure 1.1 (a-c) [Huang et al. 2009; Schroers et al. 2009]. Besides, it was also used as the Corilolis mass flowmeter or pressure sensors, as shown in Figure 1.1 (e) [Nishiyama et al. 2007], and it was reported that the sensitivity was much higher than those made from crystalline materials. With the development of the glass forming ability, new potential applications were further discovered [Schroers et al.

2007; Huang et al. 2009]. However, until now the application of this glassy system is still limited. The main reason is the brittle fracture due to the shear localization at room temperature. Thus, it is an urgent need to disclose the mechanism of their deformation behaviors, especially the failure behaviors at room temperature, and develop new kinds of MGs or their alloys that exhibit good ductility.

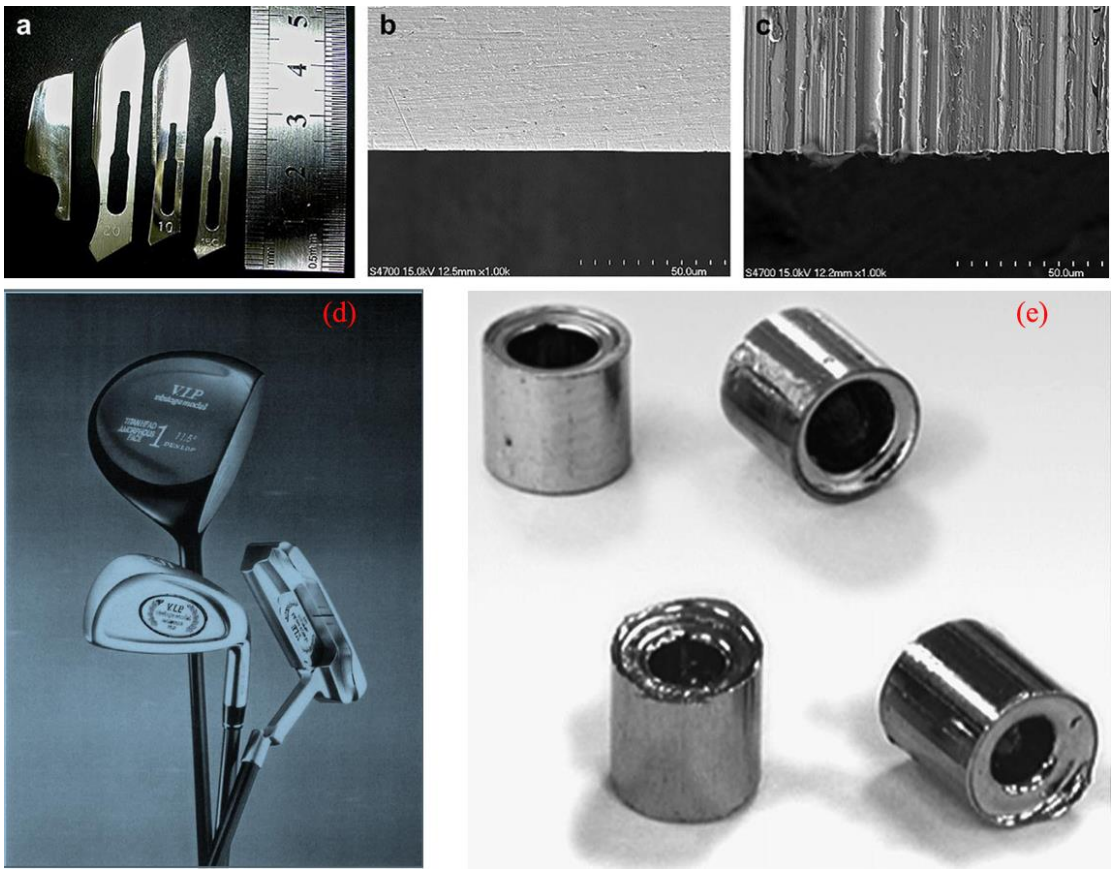

Figure 1. 1 Applications of glassy alloys in the industrial products. (a) Zr-based BMG surgical razors. (b). Zr-based BMG blade. (c). Commercial S-15C blade. [Huang et al. 2009] (d). Commercial application of glassy alloys in golf bars [Inoue 2005]. (e). Zr- and Ni-based glassy alloy diaphragms [Nishiyama et al. 2007].

In the present chapter, the deformation behaviors of the metallic glasses are first introduced. Some previous works in the literatures are reviewed to describe the

typical theories and models of the deformation mechanisms. The developments of the porous BMG and BMG composites containing *in-situ* dendrite phase are then introduced. The studies on the size effects on the mechanical properties of metallic glasses are discussed. It should be mentioned that the studies on the metallic glasses and their applications are widely conducted. The current brief review cannot cover all the aspects, and only the contents related with the present thesis research are focused on. The objectives of this thesis research are presented in the last section of this chapter.

1.1 Deformation behaviors of metallic glasses

The deformation modes of metallic glasses are complicated due to the various loading conditions and working environments. Until now, the localized deformation and the continuous viscous flow are found to be the main deformation modes in metallic glasses, which are reported to be affected significantly by the temperature and the strain rate. In the following sections, the deformation behaviors shall be described in details.

1.1.1 Homogeneous deformation of metallic glasses

The homogeneous deformation in metallic glasses usually occurs when the

temperature is greater than $0.7T_g$ [Argon 1979] and can be considered as the viscous flow in the supercooled liquid state. The significant ductility achieved through this deformation behavior results in a lot of potential applications of MGs.

It was found that the homogeneous deformation behaviors were significantly affected by the strain rates and the transition between the Newtonian and non-Newtonian behaviors could occur [Kawamura et al. 1996; Nieh et al. 1999; Bletry et al. 2004; Reger-Leonhard et al. 2000; Chu et al. 2003; Chiang et al. 2004; Bae et al. 2004].The transition between the Newtonian and non-Newtonian behaviors of homogeneous deformation depends on the applied stresses and the strain rates. The Newtonian behavior can be characterized as the relationship that the strain rate is proportional to the applied shear stress. On the other hand, it was found that the stress sensitivity of deformation decreased rapidly when the fluid flow changes into non-Newtonian deformation behavior. Stressed at low strain rates, the MGs deform as a Newtonian fluid, and become non-Newtonian flow at high straining rate. The critical straining rate for the deformation behavior transition depends on the temperatures.

In spite of the differences of the two homogeneous deformation behaviors, considerable plastic strains can be obtained in the supercooled liquid region. By using this high ductility resulting from the homogeneous deformation, some sophisticated structural components can be fabricated and have been used in the MEMS and biomedical structures [Saotome et al. 2001a; Saotome et al. 2001b; Chu et al. 2006].

1.1.2 Inhomogeneous deformation of metallic glasses

Compared with the homogeneous deformation at elevated temperatures, the localized deformation are special features observed in the deformation of MGs. The typical stress-strain curves under different strain rate were obtained by Mukai et al. [Mukai et al. 2002a] through the tensile test in the BMG as shown in Figure 1.2 (a). It was found the deformation is brittle in tension. On the contrary, the deformation in compression was characterized by a certain amount of plasticity after yielding. It was also found that the serrated flow usually featured the early stage of the plastic deformation before the occurrence of fracture as shown in Figure 1.2 (b) [Mukai et al. 2002b; Wright et al. 2001]. The formation and propagation of shear bands could cause a sudden drop in stress, which is characterized by one individual serration in

the stress-strain curve. The load could be recovered after the arrest of the shear band propagation by the surrounding material. During the shear banding extension, the formation and arrest of shear bands could occur repeatedly and result in the serrated flow, characterizing the typical stress-strain curves for the compression tests. Unlike crystalline solids, the tensile and compressive yield behaviors were found asymmetric in metallic glass through the experiment studies [Mukai et al. 2002b; Zhang et al. 2003]. It was proposed that the yield of metallic glasses should obey the Mohr-Coulomb criterion rather than the von Mises principle. This conclusion was also proved by the atomic calculation [Schuh and Lund 2003]. According to the Mohr-Coulomb criterion, the fracture angle of the samples under compression and tension should be different, consistent with the experiments [Mukai et al. 2002b].

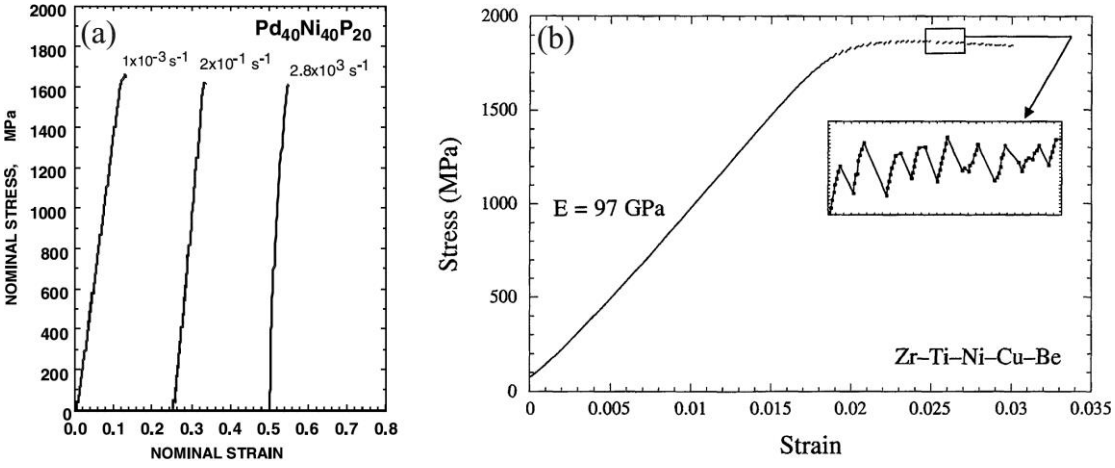

Figure 1. 2 The stress-strain curves of the tensile and compression tests. (a) Nominal tensile stress-strain curves at different strain rates [Mukai et al. 2002a]. (b). Stress-strain curve in uniaxial compression [Wright et al. 2001].

It was found that strain softening characterized the deformation in the metallic glass alloys if the temperature is lower than $0.7T_g$ [Argon 1979] or the strain rate is high, which was significantly different from the strain hardening in the crystalline solid. After yielding, an increase in strain softens the MGs and drives the material to deviate from the elasticity. It was also suggested that the strain softening was a direct reason for the shear localization and the formation of shear bands. Through experiments with a Zr-based BMG, it was found the hardness decreased with the increasing deformation strain [Bei et al. 2006]. The results suggested that the sheared region was weaker than its surrounding regions with undeformed amorphous structure during the deformation. Besides, it was found that the free volumes increased during the localized shear deformation in DSC measurements [Kanungo et al. 2003; Cao et al. 2005, Liu et al. 2007]. By quantitative analysis of high-resolution transmission electron microscopy results, it was found that high concentration of nano-scale voids, resulting from the coalescence of excess free volumes, was contained in the localized plastic deformation regions [Li et al. 2002]. The generation and coalescence of free volumes could decrease the density of the corresponding deformed regions, resulting in the softening of the materials. Another important structural evolution under plastic deformation was the localized melting

and the molten droplets observed on the fracture surfaces, which were considered as the results of temperature rise in the shear bands [Flores and Dauskardt 1999; Liu et al. 1998]. The results showed that the temperature rise could be as high as 200K in the shear band. The melting of materials could decrease the viscosity of the material, resulting in the less resistance to the loading.

These two important structural evolutions observed in the previous research were consistent with the assumptions made for the explanation of the strain softening. It was suggested that the main reason for the decrease of the viscosity in shear bands was the formation of free volumes during deformation. It was proposed that the reduction of viscosity was due to the local adiabatic heating. Based on these observations, the formation and propagation of shear band were considered as the local generation and accumulation of free volumes resulting from the dilatation or operations of the shear transformation zone (STZ) and local heating. Therefore, several models were proposed to describe the mechanisms of the deformation behavior, especially the inhomogeneous deformation.

1.2 Models of structures sustaining plastic flows

The structure of metallic glasses is generally considered as the icosahedral order proposed by Frank (Frank 1952) with highly close packed and the lack of translational periodicity. Similar to crystals, the dislocation line structures and the corresponding theory were introduced to explain the plastic flow in the metallic glass [Gilman 1973]. Through investigations on the properties of edge and screw dislocations in amorphous Lennard-Jones solid, the edge dislocation was found to be unstable while the screw was observed to be stable [Chaudhari et al. 1979]. Contrary to this, both the edge and screw dislocations were found to be stable in amorphous structure and could be moved to form a diffuse step on the surface of the model [Shi 1986]. While in MD simulation, the edge and screw dislocations were observed to be unstable in Ni-Y metallic glasses [Takeuchi et al. 2010]. Thus it may be difficult to use the dislocation theory to describe the deformation in metallic glasses.

Different from the dislocation model, the free-volume theory proposed that an empty space with volume comparable to that of one atom could help to facilitate the local structural rearrangement, avoiding much structural relaxation [Spaepen 1977]. Based on this model, several quantitative simulations have been conducted to study the

mechanical deformation in metallic glasses [Huang 2002; Dai et al. 2005; Thamburaja and Ekambaram 2007]. However, the structures of metallic glasses are different from the dense random packing of hard sphere, which is an ideal glassy structure for the definition of free volumes [Bernal and Mason 1960; Scott 1960]. Rather than one free volume or atom to accomodate the plastic strain in the metallic glasses, shear transformation zone (SZT) model suggested the local atomic cluster could act as the structural defects sustaining plastic deformation and facilitating the structural rearrangements [Speapen 1977; Argon 1979]. The fundamental process of deformation was caused by the evolution of shear transformation zone. Under the applied stress, STZ may switch between two orientational states and be more susceptible to structural rearrangement than the surrounding atoms in response to the applied stress.

Besides these theoretical studies, some experiments results are also helpful for us to understand the structural defects in metallic glasses. It was observed that either atomic jumps of a specific nature or similar localized reordering occurred during the structural relaxation, reflected by the height of the internal friction of MG sample [Kunzi et al. 1979]. By comparing the internal friction between the as-cast and

plastic deformed metallic glasses, it was found that the external stress could lead to the atomic shear rearrangements in relaxation centres and the increase of the number of these centres [Khonik 1996]. Using high-resolution transmission electron microscopy, it was also found that there was free volume variation for atoms in the shear band compared with those in the underformed regions, which suggested that free volumes could be the structure defects participating in the structural rearrangement during the plastic deformation. [Li et al. 2002].

Although the investigation of atomic structure of metallic glasses has advanced to a great extent, the understanding of defective structures are still challenging by the experimental techniques. Based on the existing experimental results, several theories of plastic flow have been developed to understand the deformation mechanism of metallic glasses.

1.3 Theories of plastic flows in metallic glasses

Understanding the deformation mechanism is important in the development of metallic glasses with high ductility. According to the macroscopic features of the deformation in MGs, some theoretical models have been proposed in the past

decades which shall be introduced in the following sections.

1.3.1 Free-volume theory

Similar to that of the hard sphere model [Bernal and Mason 1960], the free volume concept was introduced to describe the deformation behaviors of the metallic glasses by Spaepen and Argon [Spaepen 1977; Argon 1979]. The free volume is defined as the extra volume compared with the undeformed ideal densely packed amorphous structure. The deformation of the metallic glasses is considered as the diffusion or transformation of the free-volume defects. Argon [Argon 1979] proposed that the deformation defects should be in a typical size of 5-atom diameter. The shape might be sphere at high temperature and disk when the temperature was low. Besides, the explicit expression of the inhomogeneous flow rate was given by using this free-volume model [Spaepen 1977].

In term of this concept, the inhomogeneous deformation in metallic glasses could be considered as the results of the free-volume coalescence. The local free-volume density can be changed through diffusion, annihilation and stress-driven creation. Using free volume which is a function of position and time as the order parameter,

one microscopic model was proposed to describe the rate of free-volume generation and the resulting plastic flow in the metallic glasses [Huang et al. 2002]. The inhomogeneous deformation and strain localization were detected by using this free-volume model in a simple shear problem. Dai et al. [Dai et al. 2005] proposed a free-volume coalescence-diffusion Deborah number to determine whether there was shear banding instability in the MG systems to account for the competition between free volume coalescence softening [Spaepen 1977; Argon 1979; Steif et al. 1982; Johnson et al. 2002; Huang et al. 2002] and adiabatic heating softening [Leamy 1972; Liu et al. 1998]. Besides these two models developed from the concept of free volume, kinetic equations for free-volume were developed [Thamburaja and Ekambaram 2007] based on the principles of thermodynamics and the micro-force balance [Gurtin 2000]. The Helmholtz free energy of ideal amorphous alloys was supplemented by the energy which depends on the free-volume density and its spatial gradient. The proposed model was implemented by using the commercial finite-element software ABAQUS/Explicit through a user-material subroutine. According to this constitutive model, the stress-strain curves and the strain localization were well predicted.

However, it was found that the free volume of an atom in metallic glasses was just 10% of the volume of the atom [Ziman 1961], which was significantly smaller than the free space required for one atom jump. Thus, it is not appropriate to directly apply the original free-volume concept in the MG system. Actually as stated by Argon [Argon 1979], the plastic deformation may be accommodated by the diffusion of the atoms in the free-volume regions rather than the jump assisted by the atomic vacancies.

1.3.2 Shear transformation zone model

In the STZ model, it was assumed that the undeformed structure was solid-like for its shear modulus, while the structure with flow defects was liquid-like. It was also noted that the flow defects were considered as some structures consisting of STZs. These STZ regions could appear and disappear and could also orientate from one direction to another under the shear stress.

By incorporating the thermodynamics into the conventional STZ theory [Falk et al. 2004], the macroscopic deformation behaviors were described in the metallic glass systems [Langer 2006; Manning et al. 2007]. An effective disordered temperature was

introduced to govern the density of the shear transformation zones in the metallic glasses during the deformation [Langer 2006; Manning et al. 2007]. One constitutive equation describing the plastic rate of deformation tensor D_{ij}^{pl} was proposed to relate it to the deviatoric stress tensor s_{ij} as,

$$\tau_0 D_{ij}^{pl} = e^{-e_Z/\chi} f_{ij}(s,\theta) \quad , \tag{1.1}$$

where *s* is the stress tensor; $\theta = k_B T$ and $\chi = k_B T_{eff}$ are the common and effective temperature in energy units; e_Z is the formation energy of one STZ; τ_0 is the molecular time scale. On the other hand, D_{ij}^{pl} is also related to two internal state parameters: the density of the STZ Λ and the tensor m_{ij} that represents the orientational deformation. During the deformation, the two state variables obey the thermodynamic equations of motion, respectively.

The motion of effective temperature can be described as the following equation,

$$\tau_0 \frac{\dot{\chi}}{e_Z} = \kappa_1 e^{-e_Z/\chi} \Gamma(s,\theta)\left[1 - \frac{\chi}{\chi_{ss}(q)}\right] + \kappa_2 e^{-e_A/\chi} \rho(\theta)(1 - \frac{\chi}{\theta}) \quad . \tag{1.2}$$

Where, κ_1 and κ_2 are dimensionless constants. The term $\exp(-e_z/\chi)\Gamma(s,\theta)$ is proportional to the rate of entropy being produced. $\Gamma(s,\theta)$ is a temperature-dependent noise intensity, which is non-negative. The parameter $\chi_{ss}(q)$ refers to the steady state value of the effective temperature. e_A, different from e_Z, is

the formation energy during the configurational fluctuation which is coupled to the ordinary thermal fluctuation. Combined with the motion equations of the density and the orientational transformation of the STZ, the shear localization can be obtained.

Considering the thermal or mechanical noise which makes rapid and small-scale motions, the athermal limit of plasticity theory was also built. In the athermal STZ model, the number of STZs in $\pm$ direction can be described as,

$$\tau_0 \dot{N}_{\pm} = R(\pm s)N_{\mp} - R(\mp s)N_{\pm} + \Gamma(s)(\frac{N_{eq}}{2} - N_{\pm}) \quad , \tag{1.3}$$

where N is total number of molecular sites. The STZs were assumed to rotate just in the $\pm$ directions relative to the shear stress. $R(\pm s)/\tau_0$ represents the rate of the STZ transitions between + and – direction rotations, and $\Gamma(s)/\tau_0$ is the rate of the density change of STZs created and annihilated driven by the noise. By integrating the equations, the shear localization was derived in a simple shear geometry study with periodic Lees-Edwards boundary conditions. One localization criterion was also gained to describe the deformation of the metallic glassy alloys.

1.3.3 Phase-field model

One featured phenomenological model describing the deformation behaviors is the

phase-field model proposed by Zheng [Zheng and Li 2009]. The plastic deformation is accommodated by the deformation defects, which consist of sites with free volumes and are more vulnerable to atomic rearrangement than the densely packed structures. These deformation defects are randomly distributed in the metallic glasses, and can be activated by thermal or mechanical stimulation. Under the external applied stress, the activated deformation defects can accumulate, which could result in shear bands at room temperature. What is deserved to state is that the model treats the shear banding as the consequence of the structural transformation of the deformation defects.

According to the Landau theory, the system states can be described by the free energy including the energy generated by the introduction of deformation defects. Combined with the variational principle, the dynamic equations describing the displacements of the system and the evolution of the deformation defects can be derived to represent the deformation behaviors (e.g. the localized plastic strain) in the metallic glasses.

Based on this theory, several simulations were conducted and some valuable features were observed from the results. The shear localization and the crack propagation were observed in the simulation in a two-dimensional (2D) MG plate containing one initial

crack [Zheng and Li 2009]. From the calculation, the relationship between the crack propagation velocity and local heat was evaluated. Besides, the interaction between two shear bands was also predicted [Shen and Zheng 2010]. It can be concluded that the phase-field model is effective in studying the mechanical properties of the metallic glass compared with the molecular dynamics (MD) or other numerical simulations. Since the shear bands, especially those in spreading, are either too large for the MD simulation to simulate their instability evolution (the branching and interaction), or too small for the finite element method (FEM) to capture the atomic structural evolution. Therefore, the work in the present thesis shall be conducted according to this model theory. The detailed formulation of the model shall be introduced in Chapter 2.

1.4 New kinds of metallic glass alloys

During the development of the MG materials in the past decades, new kinds of glassy alloys and composites are developed to overcome the ductile limitation in engineering applications. Several kinds of MG alloys have been developed, such as the porous MG, the MG containing crystalline particles or some dendrite phases. It is found that these MG alloys avoid the brittle fracture and show ductility in a certain degree. Thus

it is necessary to investigate the mechanism where this ductile feature comes from in these new MG alloys, which will benefit the development of MG and its alloys with improved ductility.

1.4.1 Porous metallic glasses

As early as in 1996, Apfel and his coworker [Apfel and Qiu 1996] proposed the BMG foam could be developed. Soon after such theoretical investigation, the first MG foam was produced by mixing the $Pd_{43}Ni_{10}Cu_{27}P_{20}$ with the hydrated B_2O_3 under water vapor releasing [Schroers et al. 2003]. The same MG foam was also made by water quenching the Pd-Cu-Ni-P alloy around the granular salt (NaCl) followed by the elimination of the salt [Wada and Inoue 2003]. The method of introduction of the melt infiltration of hollow carbon microspheres was used to make the commercial $Zr_{57}Nb_5Cu_{15.4}Ni_{12.6}Al_{10}$ foam.

It is noted that the properties of the pores could affect the mechanical performance of the MG foams. Several studies were conducted to investigate their mechanical properties by varying the pores features. By controlling the hydrogen pressure of the atmosphere, the samples with different volume fractions and sizes of pores were

obtained. From experiments, it was noted that there was no significant differences for the thermal stability between the porous Pd-Pt-Cu-P glassy samples and those of the pore-free ones [Wada et al 2005]. During the uniaxial compression experiments on the Zr-based amorphous metallic foams, the relationships between the plastic strain, energy absorption and the pore properties were obtained [Brothers and Dunand 2005a]. Soon after this study, it was also found that the plastic strain and energy absorption were dramatically increased without much reduction in the yield strength under the compressive tests by controlling the pore size and the volume fraction [Inoue et al. 2007]. It was concluded that the ductility should be originated from the branched and wavy shear bands due to the stress concentration around the pores. Besides these experiment investigations, molecular dynamic (MD) simulations were conducted to model the nano-indentation and the uniaxial compression tests of the $Cu_{46}Zr_{54}$ metallic glasses foams [Wang et al. 2010]. It was also found that the size of the pores played a vital role in the initiation and propagation of the shear bands. The improved ductility and energy absorption ability could be gained when the pores collapse or the shear band was blocked.

From the above mentioned studies, it can be concluded that the porous MGs could

gain ductility under compression when the volume fraction and pore size were properly controlled. Nevertheless, the theoretical explanations on the origination of the improved ductility are still limited. To develop porous BMGs for structural or functional applications, it is an urgent need to investigate the mechanisms of ductile deformation in porous BMGs, especially how the pores affect the shear band initiation and propagation.

1.4.2 BMG composites containing *in-situ* dendrite phase

In the past decade, various bulk metallic glass composites were developed, such as the Zr- [Hays et al. 2000; Kuhn et al. 2002; Liu et al. 2007; Hofmann et al. 2008a], Fe- [Gu et al. 2006; Yao and Zhang 2007; Guo et al. 2010], Ti- [Hofman et al. 2008b], Ni- [Choi-Yim et al. 2005], Pd- [Hu et al. 2003], La- based [Tan et al. 2002; Lee et al. 2004] BMG composites. Two important methods were used to introduce the second phases into the BMGs [Lewandowski et al. 2006]. The *ex situ* method was to add the crystalline phase artificially into the melting during being cast into the solid. By using this method, Conner et al. [Conner et al. 1998] produced the $Zr_{41.25}Ti_{13.75}Cu_{12.5}Be_{22.5}$ glass reinforced by addition of continuous tungsten fibers or 1080-steel wires. It was found that the fracture strain and the toughness were

dramatically enhanced. On the other band, the *in situ* approach was used to form the second phase in the dendrite pattern during the solidification processes through controlling the composition. By tunning the composition in the Zr-Ti-Cu-Ni-Be system, the ductile metal-reinforced MG matrix composite was developed [Hay et al. 2000]. In the *in-situ* formed BMG composites, the plastic strain at failure, impact resistance and the ductility were significantly improved due to the formation of the dendrite phase.

In the BMG composites containing dendrite phases, the mechanical properties should depend on the properties, size, volume fraction and the distribution pattern of the crystalline dendrite. It was found that different shapes of the second phases resulted in various plastic deformation behaviors of the metallic glass composites [Schuh et al. 2007]. Compared with the dendrite shape reinforcements [Szuecs et al. 2001; Hays et al. 2000], the spherical morphology of the crystalline phase could lead to much higher ductility of the composite [Sun et al. 2006; Sun et al. 2007]. The volume fraction of the crystalline phase was another important factor affecting the mechanical properties. It was reported that the plastic strain was obviously enhanced with the increasing of the volume fraction of the dendrite phase [Szuecs et al. 2001;

Sun et al. 2006].

Based on the experiments results, the improved ductility was considered to be caused by the generation of multiple shear bands, and the restriction of the shear band propagation. To date, microscopic observation on the interaction between the dendrite and the shear band is still too difficult to be conducted by experiments. It is still ambiguous how the shape and the mechanical properties of the dendrite affect the mechanical performance of the composites.

1.5 Size effects on mechanical properties of metallic glasses

1.5.1 Size effect on mechanical properties of micro-scale metallic glasses

Several parameters have been proposed to describe the ductility of the micro-sized MG alloys. One of the most commonly used parameters is called ‘critical shear offset’, which is the shear offset within one shear band operation. It can be used to explain the size effect on the type of tensile fracture in the metallic glass system [Wu F.F. et al. 2009]. It was found that a certain amount of tensile plasticity could be derived when the sample size was smaller than the equivalent shear offset. Assuming

the similarity between the shear offset formation in MGs and the dislocation gliding in the crystalline solid, the fracture mechanics was introduced and the plastic zone size in front of the shear band was proposed to study the size effect [Yu et al. 2009; Ashby and Greer 2006; Yuan and Xi 2011; Wu F.F. et al. 2008; Wu W.F. et al. 2008; Wu et al. 2010a]. The sizes of the plastic zones were estimated for a variety of MG systems and the origin of plasticity was found to correlate to its size [Yu et al. 2009]. Similar to this plastic-zone theory to predict the fracture type, a critical plane energy density was proposed to estimate the catastrophic failure [Wu et al. 2010a]. The transition between the ductile and brittle failures was also systematically studied by Han [Han et al. 2009] and an equation for the critical instability index was given. Based on the instability index proposed by Han, another instability index was derived by simplifying the elastic support of a BMG compression sample as a spring [Cheng et al. 2009]. Both these indexes supplied us convenient ways to understand the size effects on the fracture modes of MGs.

Besides the size effect on the fracture modes, the plastic zone theory was further used to study the influence of sample size on the mechanical properties, such as the yield stress and fracture toughness [Ashby and Greer 2006: Yuan and Xi 2010; Wu

F.F. et al. 2008; Wu W.F. et al. 2008]. The results showed that the fracture toughness increased with the reduction of the sample size. Nevertheless, the results about size effect on the yield strength in the literatures are contradictory. Some researchers found that the yield strength increased as the sample size decreased [Lai et al. 2008; Cheng et al. 2007; Lee et al. 2007], while Dubach et al. did not detect any size-dependent yield stress of MGs [Dubach et al. 2009]. These diverse results might be caused by the imperfect pillar geometry of the samples, the various artificial defects or some inconsistent testing conditions.

1.5.2 Size effect on mechanical properties of nano-scale metallic glasses

Cheng [Cheng et al. 2009] found that the shear-band speed would be slow down and the temperature in the shear band would get lower when the sample size was decreased, i.e., the shear banding was hindered or slowed down. According to the principle of energy balance, whether the shear band is activated or not can be determined according to the comparison between the strain energy and the energy of the shear band. Thus in the pillar sample there should be a critical stress or critical strained volume that is required for the shear band formation [Wu F.F. et al. 2009; Li

and Li 2006]. Volkert and his coworkers [Volkert et al. 2008] estimated that the critical stress required for shear band formation should increase with decreasing column diameter. There might be no sufficient strained volume to reach the energies or local stress to form the shear band when the sample size decreases to below 400 nm, resulting in homogeneous deformation without localised shear banding. On the other hand, removing the correlation among a certain number of the free volumes was also helpful in avoiding the localized deformation. Through the MD simulation, Delogu [Delogu 2009] stated that the correlation between consecutive STZs was prevented by decreasing the sample size, which could result in the change of the deformation modes of MGs. Chen [Chen et al. 2011] also found that the homogeneous deformation occurred when the sample size decreased to 70 nm.

Compared with the above mentioned results concerning the compressive tests, a fewer reports were focused on the size effect on the tensile properties of MGs. It may be because that it was very difficult to conduct the tensile tests of the nano-scale regular samples. However, some interesting and meaningful phenomena have been reported. The necking was obviously observed without any localized deformation during the tensile tests. By adding some unevenness on the surface, the

sample obtained 23% elongation until fracture through necking, and no shear banding appeared during the tensile test [Guo et al. 2007].

1.6 Motivations and objectives

Although the studies on the MGs were conducted for more than half a century, our understanding on the deformation mechanism of MGs is still not complete. The free-volume theory seems improper to describe the localized strain in the metallic glass (MG) systems, since the hole for the atomic jump was not necessary for the deformation in MG system. In the past decades, some amorphous alloys (e.g. porous BMGs, BMGs containing *in-situ* dendrite phase and the nano-scale MGs) have been produced. They are found to show improved ductility compared with conventional BMGs. However, theoretical and simulation investigation on the origin of resulting ductility of these amorphous alloys are still limited. It should be noted that the span of the length and time scales are so vast. Thus the shear-band propagation is too large for the molecular dynamic (MD) simulation to simulate the unstable states, such as the branching and interaction functions. It was also found that the atomic scale deformation details were so small that the finite element method was unable to capture its features. Nevertheless, the phase-field model in mesoscopic scale can be

used to bridge this gap and describe the shear-band initiation, propagation, even the branching and interaction in the MG systems and its composites, which can help us to disclose the mechanism of improved ductility of the MG systems.

In this work, the phase-field model on MG systems will be used to numerically investigate the above-mentioned issues concerning the metallic glasses and the MG composites, which are found to exhibit improved mechanical properties of the MGs, copping with the fatal brittle failure in the BMGs.

Chapter 2 Simulation methodology—Phase-field modeling methods

Phase-field modeling is an effective method to study the phase transitions, microstructure evolutions and the properties of various ordered microstructures. Shear banding at room temperature in MGs results from the competition among creation, accumulation and the annihilation of the defective glassy regions, accompanied by changes in structural order in the system. Thus it is suitable to investigate deformation mechanisms concerning the shear banding in MGs based on the phase-field theory. In this Chapter, we describe the theoretical framework of phase-field modeling methods that are used for the simulation of mechanical deformation issues related with shear banding in MGs.

2.1 Phase-field modeling on microstructure evolution

2.1.1 Phase-field modeling on kinetics of phase transitions

The thermodynamics can only tell us the general microstructure evolution trend during phase transformation [Haasen 1974], but it is the highly non-equilibrium

microstructure rather than the state close to the equilibrium state that determines the material properties [Raabe 1998]. Compared with the empirical methods, computer simulation based on theoretical state variable approach can tackle the phase-transformation kinetics, describing both the spatial and temporal changes in the chemical, crystallographic and structural orders of the materials, which are defined as the phase-field variables.

As early as 1930s, Landau developed a thermodynamic theory of secondary-order (continuous) phase transition [Landau 1937a; Landau 1937b]. Subsequently, various authors applied Landau's theory to a great variety of phase transitions. Among those, Cahn-Hilliard and Allen-Cahn kinetic phase-field models [Cahn and Hilliard 1958; Cahn 1961; Cahn 1962; Cahn 1965; Allen and Cahn 1979], being considered as the metallurgical derivatives of the Onsager [Onsager 1931a; Onsager 1931b] and Ginzburg-Landau theories [Landau 1937a; Landau 1937b], are versatile to describe the continuous and quasi-discontinuous phase transition phenomena in the coherent and non-coherent metallic systems. By extending the Cahn-Hilliard model, the Allen-Cahn model aims to cope with the nonconserved-variable based phase transformation (e.g. Long-range order, crystal structure)[Allen and Cahn 1979].

The original Ginzburg-Landau approach was based on the general Onsager or Ginzburg-Landau kinetic equation written as,

$$\frac{\partial \psi_i}{\partial t} = -\hat{M}_{ij} \frac{\delta \hat{F}}{\delta \psi_j} \quad , \tag{2.1}$$

where $\hat{F}$ is the free energy functional of various functions ψ_j , t means the time and $\hat{M}_{ij}$ is the symmetric Onsager kinetic operator matrix, $i, j = 1, 2, \ldots$.

In a magnetic system, based on the assumption that the potential energy of the system can be expanded as a power-law series close to the critical temperature T_c [Landau 1937a; Landau 1937b], the free energy of Landau form can be developed in terms of all the nearest neighbor binding enthalpies and their configurational entropy. Then for the introduction of a concentration field $\psi(\mathbf{r},t)$, the local free energy density close to the critical points T_c and ψ_{crit} can be described as,

$$f(\psi(\mathbf{r},t)) = f_0 + \frac{A}{2}(\psi(\mathbf{r},t) - \psi_{crit})^2 + \frac{B}{4}(\psi(\mathbf{r},t) - \psi_{crit})^4 + \frac{C}{6}(\psi(\mathbf{r},t) - \psi_{crit})^6 + \ldots, \tag{2.2}$$

where, A, B, C are the phenomenological constants which must be fitted from the relevant theory or experiments.

This magnetic second-order phase transition theory supplies fundamental for some other kinds of phase transition issues in materials science. The successful introduction

of metallurgical variants allows us to address the phase transformations in metallic systems according to the chemical or structural phase-field variables [Cahn and Hilliard 1958; Cahn 1961; Cahn 1962]. As early as 1958, Cahn and Hilliard theoretically investigated the isostructural decomposition phenomena [Cahn and Hilliard 1958]. Being furnished with this Landau type potential and a gradient interface term, the classical Cahn-Hilliard equation can be obtained as,

$$\frac{\partial c(\mathbf{r},t)}{\partial t} = M\nabla^2[(\frac{\partial F}{\partial c(\mathbf{r},t)})_T - \kappa\nabla^2 c(\mathbf{r},t)] \quad , \tag{2.3}$$

which is used to describe the concentration evolution in the alloys [Cahn 1965]. κ represents the interfacial energy, and $c(\boldsymbol{r},t)$ is the field variable describing the concentration of the impurity in the material.

However, there always are issues concerning the non-conserved parameters, such as the crystal orientation, long-range order or crystal structure, during the microstructure evolution. Thus it is necessary to further introduce the nonconserved fields to predict the non-isostructural phase transformation phenomena. At the same time, the free energy should also be modified through adding the function of one or more structural variables $\eta_i(\boldsymbol{r},t)$ and i=1, 2, …, 9. For example, the local free energy density can be obtained as the following statement when there is only one structure variable $\eta(\boldsymbol{r},t)$,

$$f_{loc}(c(\mathbf{r},t),\eta(\mathbf{r},t)) = \frac{D_1}{2}(c(\mathbf{r},t)-c_{crit1})^2 + \frac{D_2}{4}(c_{crit2}-c(\mathbf{r},t))\eta^2(\mathbf{r},t) - \frac{D_3}{4}\eta^4(\mathbf{r},t) + \frac{D_4}{6}\eta^6(\mathbf{r},t) \quad , \qquad (2.4)$$

where D_1, D_2, D_3, D_4, c_{crit1}, c_{crit2} are phenomenological constants which should be fitted from the relative theory or experiments.

Considering the non-conserved ordering process, the kinetic equation for the non-conserved phase-field variable was derived through studying the curved antiphase boundary motion [Allen and Cahn 1979],

$$\frac{\partial \eta}{\partial t} = M_\eta \nabla^2 \eta - \alpha \frac{\partial \Delta f(\eta)}{\partial \eta} \quad , \qquad (2.5)$$

where $M_\eta = 2\alpha\kappa$ is in units as a diffusion coefficient m^2/s, α is the positive kinetic coefficient, f is the free energy density and η is the nonconserved order parameter. This non-linear equation is similar to the time-dependent Ginzburg-Landau equation (TDGL) in which there is no conservation. It supplies theoretical foundation for us to investigate the kinetics of the order parameter describing the process of the phase separation in alloys (e.g. the order-disorder transitions).

The generalized phase-field models are developed by furnishing the Ginzburg-Landau or Onsager kinetic equation (as shown in Eq. (2.1) with an

appropriate well-fitted Landau free energy density functional of both the conserved and nonconserved phase-field variables.

2.1.2 Phase-field modeling on deformation behaviors of solids

2.1.2.1 Fracture dynamics

The dynamic fracture is a challenging topic for the classical approaches of mechanics [Freund 1990], especially it is difficult to predict the instability of the tip dynamics. For the mode III dynamic fracture, one scalar field, distinguishing the "broken" and "unbroken" states of the system, was introduced in the phenomenological continuum model [Karma et al. 2001; Karma and Lobkovsky 2004]. The order parameter ϕ ranges from 0 to 1.0. $\phi = 0$ represents the unbroken state and $\phi = 1$ means the fracture state of the system with crack occurring. By coupling the order parameter to the displacement field $\boldsymbol{u}$, the main dynamic equations are stated as [Karma et al. 2001; Karma and Lobkovsky 2004],

$$\chi^{-1}\partial_t\phi = -\frac{\delta F}{\delta \phi} = \kappa\nabla^2\phi - hf'(\phi) - \mu g'(\phi)(\left|\nabla \mathbf{u}\right|^2 - \varepsilon_c^2) \quad , \tag{2.6a}$$

$$\rho_0\partial_t^2\mathbf{u} = \nabla\cdot\boldsymbol{\sigma} = \mu\nabla\cdot[g(\phi)\nabla\mathbf{u}] \quad . \tag{2.6b}$$

The Eq. (2.6a) describes the dynamic evolution of the order parameter, and the crack

should occur when the value of ϕ reaches 1.0. The deformation process can be represented through Eq. (2.6b) under external loading. Here, the function $g(\phi)$ is a monotonously increasing function of field variable ϕ with limit $g(0) = 0$ and $g(1) = 1$, controlling the softening of the system when the strain is large. $f(\phi)$ is a double-well potential with minimum at $\phi = 0$ and $\phi = 1$. μ is the elastic shear modulus and ε_c is the critical strain of yielding. κ is the interfacial energy and the length scale describing the process zone size is defined as $\xi = \sqrt{\kappa/\mu\varepsilon_c^2}$. The characteristic time for the energy dissipation is $\tau = 1/\chi\mu\varepsilon_c^2$. ρ_0 means the density of the material. $e_c = 0.5\mu\varepsilon_c^2$ can be considered as a measure of the fracture energy of the solid.

In contrast to this non-conserve field introduction, Eastgate et al. proposed a phase-field model by using the normalized mass density, coupling the displacement field as the order parameter to describe the fracture of mode I [Eastgate et al. 2002]. This theory was similar to the model simulating the structure evolution as the solidification [Langer 1980]. This order parameter ϕ ranges from 0 to 1.0, where ϕ = 0 is the vacuum state characterizing the crack occurring and ϕ = 1.0 represents the unstrained material. The free energy of the system was obtained as the integral,

$$F = \int \left\{ \left(\frac{w^2}{2} \right) |\nabla \phi|^2 + g[\phi, \varepsilon] \right\} dV \quad , \tag{2.7}$$

where,

$$g[\phi, \boldsymbol{\varepsilon}] = \frac{h^2}{4} \phi^2 (\phi_s [\boldsymbol{\varepsilon}] - \phi)^2 + \phi^2 e[\boldsymbol{\varepsilon}] \quad . \tag{2.8}$$

The first term in Eq. (2.7) characterizes the spatial fluctuation of the phase field. The second term is described as Eq. (2.8), in which the first term is a Ginzburg-Landau double well potential controlling the phases of vacuum state and the solid phases. $\phi_s[\varepsilon] \equiv 1 - \varepsilon_{mm}$ and if the material is in unstrained state, $\phi_s \equiv 1$, otherwise this value can be higher or lower according to the loading situation (compression or tension). The factor $\phi_s[\boldsymbol{\varepsilon}] - \phi$ can be considered as the density of vacancies or interstitials. The parameter h controls the energy barrier between the solid and vacuum states, and w/h governs the width of the solid-vacuum interface. $e[\varepsilon]$ is the strain energy of the system. The motion of the phase field ϕ and the displacement $\boldsymbol{u}$ are overdamped and Eulerian, moving the fields along the direction of net force. The time derivative is thus proportional to the force on the field. Specifically it can be described as,

$$\frac{\partial \phi}{\partial t} = -\nabla \cdot J \,, \quad J = -D \nabla \frac{\delta F}{\delta \phi} + \phi \frac{\partial \mathbf{u}}{\partial t} \quad , \tag{2.9a}$$

$$\frac{\partial \mathbf{u}}{\partial t} = -\frac{1}{\eta} \frac{DF}{D\mathbf{u}} = -\frac{1}{\eta} \left(\frac{\delta F}{\delta \mathbf{u}} + \phi \nabla \frac{\delta F}{\delta \phi} \right) \quad , \tag{2.9b}$$

where, η and D are the viscosity and the diffusion constant respectively. Eq. (2.9a) is

the continuity equation. The first term in *J* is a diffusion term, while the second term makes sure that the mass follows the motions of the displacement field. In fact this model seems to describe the fracture of a colloidal crystal.

2.1.2.2 Dislocation dynamics

Other typical applications of phase-field model are to describe the motions of the dislocation, vacancies and grain boundary in the crystalline solid [Wang et al. 2001]. Dislocations play a key role as the plastic deformation carrier during the deformation in metallic materials. By introducing the density functional field $\eta(\alpha, m_\alpha, \boldsymbol{r})$ which equals to the number of slip modes determined by the crystallography of the system, the free energy can be described as,

$$E^{cryst} = \int \left(\sum_{\alpha=1}^{p} \sum_{m_\alpha=1}^{q} \sum_{n=1}^{\infty} A_n \sin^2 n\pi\eta(\alpha, m_\alpha, \mathbf{r}) \right) d^3r \quad , \tag{2.10}$$

where m_α is the Burgers vector in the slip plane α. On the other hand, the gradient energy in the case of dislocation system can be written as,

$$E^{grad} = \frac{1}{2} \int \left(\sum_{\alpha_1=1}^{p} \sum_{\alpha_2=1}^{p} (\beta_{ijkl}(\alpha_1, \alpha_2) \times \frac{\partial b_i(\alpha_1, \mathbf{r})}{\partial r_j} \frac{\partial b_k(\alpha_2, \mathbf{r})}{\partial r_l} \right) d^3r \quad , \tag{2.11}$$

where

$$\mathbf{b}(\alpha, \mathbf{r}) = \sum_{m_\alpha=1}^{q} \mathbf{b}(\alpha, m_\alpha) \eta(\alpha, m_\alpha, \mathbf{r})$$

represents the Burgers vector density in all slip planes of the type α. $\beta_{ijkl}(\alpha_1, \alpha_2)$

is a constant tensor which is positive and provides a vanishing interfacial energy along the slip planes of the inclusions. Then the stress-free strain ε_{ij}^{0} produced by the Burgers vector is described as,

$$\begin{aligned}\varepsilon_{ij}^{0}(\mathbf{r}) &= \sum_{\alpha=1}^{p}\sum_{m_\alpha=1}^{q}\varepsilon_{ij}^{0}(\alpha,m_\alpha)\eta(\alpha,m_\alpha,\mathbf{r}) \\ &= \frac{1}{d}\sum_{\alpha=1}^{p}\sum_{m_\alpha=1}^{q} b(\alpha,m_\alpha)_i n(\alpha)_j \eta(\alpha,m_\alpha,\mathbf{r})\end{aligned} \quad . \tag{2.12}$$

Based on this definition, the elastic energy of the elastically homogeneous but structurally inhomogeneous coherent system under applied stress σ_{ij}^{appl} can be described as,

$$\begin{aligned}E^{elast} = \frac{1}{2} f(\int [C_{ijkl}\tilde{\varepsilon}_{ij}^{0}(\mathbf{k})\tilde{\varepsilon}_{kl}^{0}(\mathbf{k})^{*} - e_i\tilde{\sigma}_{ij}^{0}(\mathbf{k})\Omega_{jk}(\mathbf{e})\tilde{\sigma}_{kl}^{0}(\mathbf{k})^{*}e_l]\frac{d^3k}{(2\pi)^3}) \\ -\sigma_{ij}^{appl}\int \varepsilon_{ij}^{0} d^3r\end{aligned} \quad , \tag{2.13}$$

where the symbol *f* represents a principle value of the integral and the superscript $*$ defines a complex conjugation. C_{ijkl} is the elastic modulus tensor. $\Omega_{ik}(e)$ is the Green function defined as the inverse of the tensor $\Omega_{ik}^{-1}(e) = C_{ijkl}e_j e_l$, $\boldsymbol{e}=\boldsymbol{k}/|\boldsymbol{k}|$ is a unit vector in reciprocal space along $\boldsymbol{k}$.

The total energy of an arbitrary dislocation system can be obtained by the summation of the crystal energy, the elastic strain energy and the gradient energy,

$$E = E^{elast} + E^{cryt} + E^{grad} \quad . \tag{2.14}$$

According to the phenomenological time-dependent Ginzburg-Landau (TDGL) equation, the kinetic equation for the fields $\eta(\alpha, m_\alpha, r)$ can be obtained,

$$\frac{\partial \eta(\alpha, m_\alpha, \mathbf{r}, t)}{\partial t} = -L \frac{\delta E}{\delta \eta(\alpha, m_\alpha, \mathbf{r}, t)} \quad , \tag{2.15}$$

where L is the kinetic coefficient characterizing the dislocation mobility. By solving Eq. (2.15), the evolution and motions of the dislocation in the crystalline system can be obtained. The distribution of the inelastic strain around the dislocation can also be derived through Eq. (2.12).

2.2 Phenomenological models of structure defects in metallic glasses

Compared with the dynamical equilibrium state of the density of free volumes in liquid, the free volumes in metallic glasses are unstable and dispersed [Bennett et al. 1979]. Through the atomic force microscopy (AFM), it was found that the structure of MGs consisted of ideal regions (densely-packed atomic cluster) and defective locations (loosely packed atomic cluster) [Liu et al. 2011]. The similar feature of structure heterogeneity was also found in the annealed MGs [Yang et al. 2012]. Thus it is reasonable to assume the structure model of the metallic glass as the composite of ideal glassy matrix and the defective regions. It is difficult to directly detect the shape

and size of the defective region in the metallic glasses due to the limitation of the experimental method, although the densely packed regions were considered as fractal [Yang et al. 2012]. The average size of the defective regions was estimated as 1~4 nm in radius as dedicated in AFM results [Yang et al. 2012], while the volume of the activation cluster was calculated as 0.135 nm^3 for Pd-based BMG through the internal friction tests [Shen 2013].

The kinetics of the loosely packed regions controls the mechanical properties of the metallic glasses. Through the internal friction experiments, it was found that the obvious variation of the structural defects took place during the structural relaxation [Khonik and Spivak 1996; Khonik 1996]. Compared with the as-cast $Ni_{60}Nb_{40}$ sample, the larger internal friction peak and more than 10% modulus deficiency were detected for the cold rolling (inhomogeneous deformation) BMG [Khonik and Spivak 1996]. It was indicated that significant modification of defective structure had taken place, and especially the new defective structures were created. Combined with the hysteresis observed, it was suggested that the external applied stress caused the creation of the dislocation-like defects and their motions [Khonik and Spivak 1996], which can be considered as the phase transition during the plastic

deformation. In addition, it was found that the internal friction peak disappeared for the cold-rolling sample after annealed at sub-T_g temperature [Khonik and Spivak 1996]. It was also found that the MGs annealed at higher temperature could cause the lower internal friction, which indicated the annihilation of the defects [Shen 2013]. Hence, it can be concluded that the structural defects in MGs could be created and activated through the external loading and the as-cast defects could also be annihilated through the thermal treatment at elevated temperatures.

As shown in Figure 2.1, the original defects or the as-synthesized defects which are defined as the "relaxation centre" in Khonik's internal friction test could change their structures into those of the deformed defects (containing metastable phase) during the room-temperature deformation process. Under external thermal stimulation, the initial defective structure can relax to the ideal glassy structure. Transformation between the ideal glass and the deformed defects occurs under mechanical deformation or thermal fluctuation. Such as-synthesized defects whose structures change significantly with external loading could be considered as deformation defects.

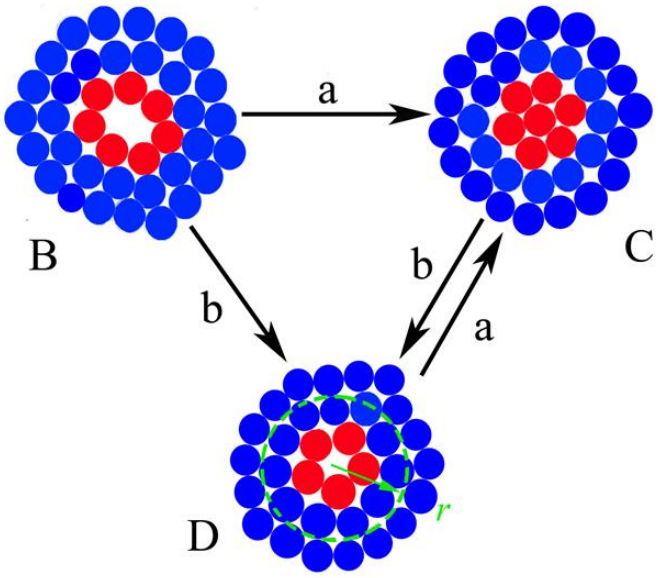

Figure 2. 1 Models of the structural changes in MGs under thermal and mechanical fluctuation. ”B” represents the atomic configuration of the as-synthesized defects. “C” is the ideal randomly close packed glassy structure. “D” marks the structure configuration of the deformed defects. Arrows “a” and “b” denote the thermal and mechanical activation process respectively.

The shape of the structural defects is difficult to be detected directly. Nevertheless, it was found there were free volume variations per atom in the shear band compared with the underformed regions, which was observed through the high-resolution transmission electron microscopy [Li et al. 2002]. During the deformation in metallic glass, free volume is one of the dominant structure defects participating in the structural rearrangement. Thus it is reasonable to consider the atomic cluster consisting of free volumes as the deformation defects.

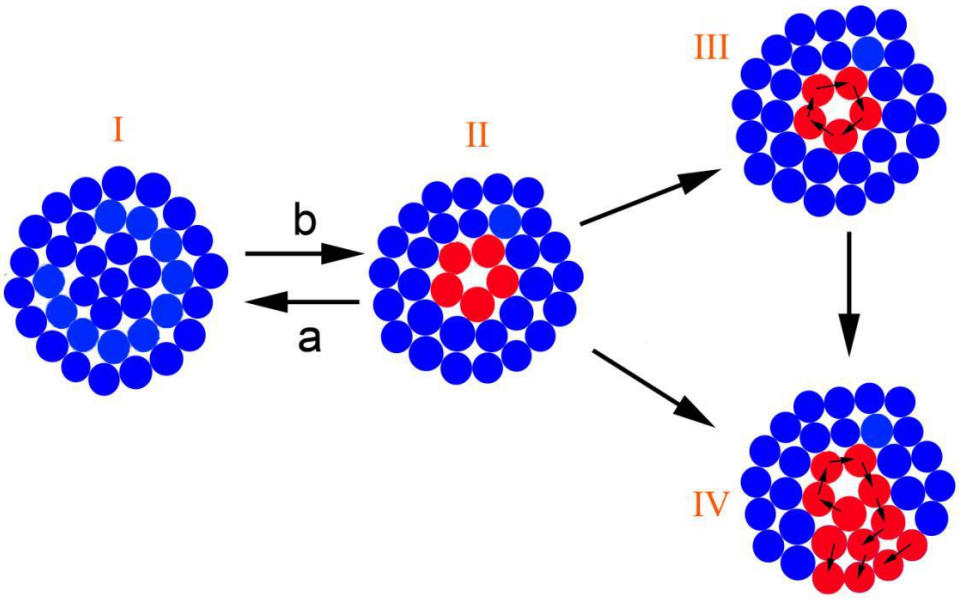

Figure 2. 2 Schematics of atomic configurations in: (I) ideal glass; (II) defect and atomic rearranging movement; (III) Structural relaxation and (IV) An atomic arrangement into plastic flow. Each energy state and atomic movement event can be activated through thermal or/and mechanical stimulation. Meanings of "a" and "b" are the same as those in Figure 2.1.

Under external fluctuation, the deformed deformation defects (marked as "D" in Figure 2.1 and "II" in Figure 2.2) will resort to more stable state. Under weak external stimulation, the atomic rearrangement is confined by the surrounding matrix marked by the transformation from II to III in Figure 2.2. With increasing applied shear strain, more strain energy need to be absorbed and relaxed by the glassy matrix around the defects, resulting in atomic rearrangement marked as structure IV in Figure 2.2 to sustain the plastic flow. The irreversible transformation is named as α relaxation [Shen 2003]. The accumulation and continue creation of structure IV shall make the sample fail. Besides, cooperative motions of local atoms

can lead to the irreversible structural transition in MGs [Ladadwa and Teichler 2006] as shown as transition from structure II to IV in Figure 2.2. This irreversible event corresponds to the localised motions of atomic defects and is a result of the creation and annihilation of the deformation defects. On the other hand, the defective structure can be recovered to the initial ideal glass state under the thermal activation as the transition from the state II to I shown in Figure 2.2. The structures and transitions among them shown in Figure 2.2 could exist during the deformation and the deformation mode can be determined by the competition among the transitions.

Thus, the phase-field theory is suitable to be applied to describe the deformation behaviours in metallic glass at room temperature similar to those describing the fracture and dislocation in crystalline solids. In the following sections, the phase-field model for the shear banding in MGs shall be described.

2.3 Formulisms of phase-field modeling on deformation of metallic glasses

Shear banding characterizes the deformation of MGs below $0.7T_g$. The shear band originates from the stress concentration caused by the initial crack or some other

initial deformation defects, while the evolution of shear band is a complex procedure concerning many factors. In the phenomenological description of shear banding, the plastic deformation is considered to be carried by the deformation defects consisting of sites with free volumes. As other theories [Falk and Langer1998, Spaepen 1977, Argon 1979] proposed, it could be assumed that the amorphous materials consisting of ideal glasses which possess a shear modulus, and the deformation defects which may behave like a liquid. The deformation defects may appear and disappear under the thermal or mechanical activations. When the applied stress is higher than the yield or flow strength, the activated free volume sites accumulate and the deformation defects can transform irreversibly to another more stable structure. When the collection of the deformation defects consisting of sites with activated free volumes reaches a certain level, shear band occurs.

As discussed above, the shear band in MGs could be considered as a consequence of the structural transformation of deformation defects, which represents that the structures consisting of free volumes are more vulnerable to external rearrangement than those of the ideal glass. Activated thermally or mechanically, the structures of the deformation defects shall rearrange, and the shear band shall be represented as a result

of accumulation and nucleation of the deformed deformation defects when the local deformation reaches a certain level. Thus in the phenomenological model, the density of deformation defects could be chosen to represent the occurrence of the shear band based on the assumption that this scalar quantity can also reflect the change of other quantities such as local atom packing, chemical composition, short- and medium-range topological order and so on. Without this assumption, the deformation state of the system in the completely disordered materials such as MGs would be too complicated to be described by this phenomenological model. Thus the density of deformation defects is usually used as the order parameter in the model.

The normalized density of deformation defects can be defined as $\rho(\boldsymbol{r})=(v_i-v_0)/(v_m-v_0)$, where v_i is the atomic volume of the ith atom, v_m is the maximum dilated volume when complete decohesion occurs at the sites, and v_0 is the volume in the ideal random close packed state. When the temperature is below the glass transformation temperature T_g and the applied load is lower than the flow stress, few sites with large density of deformation defects could be activated and thus the MGs act like an elastic solid. When the applied load approaches the flow stress or the local heating is involved, e.g., from excessive plastic deformation, more sites with large density of deformation

defects could be activated [Spaepen 1977; Flores et al. 2002; Pampillo 1975; Chen et al. 1994]. As the above mechanism states, the ideal un-deformed state can be described as the structure with $\rho(\boldsymbol{r})=0$, and the presence of disorder structure compared with the reference state can be represented as $\rho(\boldsymbol{r})\neq 0$. The shear band can be described as the states when the density of deformation defects is greater than one critical value, defined as $\rho(\boldsymbol{r})\geq 0.8$, while the fracture occurs when $\rho(\boldsymbol{r})\rightarrow 1.0$.

According to the phenomenological description on the deformation and fracture features in the MGs from the atomic scale, the free-energy density can be written as a function of the density of deformation defect $\rho(\boldsymbol{r})$ according to the Ginzburg-Landau formulism when the system is free of external stress,

$$f_\rho = \frac{a}{2}\rho^2 + \frac{b}{3}\rho^3 + \frac{c}{4}\rho^4 + \cdots, \tag{2.16}$$

where *a*, *b* and *c* are the coefficients depending on temperature, strain, chemical composition, or other state variables. From Eq. (2.16), we can also note that when the order parameter $\rho(\boldsymbol{r})\rightarrow 0$, the free energy $f(\rho)=0$, which means the structure is kept as the undeformed ideal randomly close packed (RCP) state. Any deviation from the reference state will cause the increase of the free energy. When $\rho(\boldsymbol{r})\rightarrow 1.0$, the system is full of activated deformation defects and the glassy structure shall fail.

According to the characteristic of shear band, the regions around the deformation defects still remain elastic, and the strain energy which corresponds to the long-range elastic field originated from the external applied stress can be written as,

$$e\left[\varepsilon_{ij}\right]=\frac{1}{2}C_{ijkl}\varepsilon_{kl}\varepsilon_{ij} \quad , \tag{2.17}$$

where ε_{ij} is the component of the strain tensor defined by the displacement field $\boldsymbol{u}$ as

$$\varepsilon_{ij}=(\partial u_j/\partial x_i+\partial u_i/\partial x_j)/2, \quad i,j=1,2,3;$$

C_{ijkl} is the component of the stiffness matrix, which is defined as,

$$C_{ijkl}=\mu(\delta_{ij}\delta_{kl}+\delta_{il}\delta_{jk})+\lambda\delta_{ik}\delta_{jl} \quad ,$$

where μ is the shear modulus and λ is Lame constant. Under external loading, the total free energy can be described as the following equation,

$$f(\rho,\varepsilon_{ij})=e\left[\varepsilon_{ij}\right]+f_\rho=e\left[\varepsilon_{ij}\right]+\frac{a}{2}\rho^2+\frac{b}{3}\rho^3+\frac{c}{4}\rho^4+o(\rho^5). \tag{2.18}$$

In Eq. (2.18), the coefficients *a*, *b* and *c* can be expanded as a Taylor's series of the plastic strain energy Δe according to the perturbation scheme usually used in the Landau theory as,

$$\begin{aligned} a &= a_0+a_1\Delta e+a_2\left(\Delta e\right)^2+\cdots, \\ b &= b_0+b_1\Delta e+b_2(\Delta e)^2+\cdots, \\ c &= c_0+c_1\Delta e+c_2(\Delta e)^2+\cdots, \end{aligned} \tag{2.19}$$

where $\Delta e=e[\varepsilon_{ij}]-e_0$, and e_0 is the strain energy at the elastic limit when $\sigma\rightarrow\sigma_f$. The coefficients a_0, b_0 and c_0 in Eq. (2.19) depend on external state variables except the strain. In MGs, the plastic deformation only causes limited strain increment at the onset of plastic flow, thus it is reasonable to expand the coefficients in the power series function of the Δe to describe the coupling between the plastic deformation and the order parameter (density of the deformation defects). By considering the fourth order of the product of Δe and ρ as the leading error term, we can obtain the local free energy density of the MGs as the following approximation,

$$f(\rho,\varepsilon_{ij})=e\left[\varepsilon_{ij}\right]+\frac{a_0}{2}\rho^2+\frac{b_0}{3}\rho^3+\frac{c_0}{4}\rho^4+(\frac{a_1}{2}\rho^2+\frac{b_1}{3}\rho^3)(e\left[\varepsilon_{ij}\right]-e_0). \qquad (2.20)$$

This equation describes the contribution from the deformation defects and the plastic deformation due to the external applied stress. On the other hand, the local softening can also be caused by the creation or annihilation of the deformation defects [Stief et al. 1982]. We could couple local heating and the order parameter by assuming the linear relation between the temperature T and a_0 as, $a_0=a'(T_g-T)/T_g$ where a' is a constant.

Under external load, the free energy of the system consists of the kinetic energy and the gradient energy between the regions with different density of the deformation

defects. Thus the free energy can be described as an integral of the free-energy density, the gradient of the density of deformation defect and the kinetic energy over the whole volume of the medium,

$$F = \int \left\{ \frac{\rho_0}{2} \left[\dot{\mathbf{u}} \right]^2 + f(\rho, \varepsilon_{ij}) + \frac{\kappa}{2} \left| \nabla \rho \right|^2 \right\} dV, \tag{2.21}$$

where ρ_0 is the mass density of the sample, κ is the surface tension between the regions with different density of the deformation defects. In this expression, the first term describes the kinetic energy of the system, the second term represents the local density of free energy and the last one is the gradient energy of the structure.

Based on the TDGL, the equations of motions for $\boldsymbol{u}$ and ρ can be described as the variation of the free-energy of the system,

$$\rho_0 \frac{\partial^2 \mathbf{u}}{\partial t^2} = -\nabla \cdot \left[\frac{\delta F}{\delta \varepsilon_{ij}} \right] = \mu \nabla \cdot \left[\left(1 + \frac{a_1}{2} \rho^2 + \frac{b_1}{3} \rho^3 \right) \nabla \mathbf{u} \right], \tag{2.22a}$$

and,

$$\tau_\rho \frac{\partial \rho}{\partial t} = -\frac{\delta F}{\delta \rho} = \kappa \nabla^2 \rho - (a_0 \rho + b_0 \rho^2 + c_0 \rho^3) - \rho (a_1 + b_1 \rho) \left(e\left[\varepsilon_{ij} \right] - e_0 \right), \tag{2.22b}$$

where τ_ρ is the characteristic time for deformation defects activation. Eq. (2.22a) controls the deformation of the material, especially the localized strain. Eq. (2.22b) describes the structural evolution of the material, especially the accumulation of the deformation defects under the influence of the plastic strain. It is noted that the

effective shear modulus obtained from Eq. (2.22a) for a locally homogeneous system is dependent on the amount of the deformation defects, which is consistent with the observation of the softening of the material in atomistic simulation [Li and Li 2007] and the experiments [Johnson 2002; Inoue and Takeuchi 2004; Pampillo 1975].

Furthermore, it is believed that the heat conduction equation can be used to describe the local heating due to the localized plastic strain in the material systems. The conduction equation can be stated as,

$$k\nabla^2 T + \beta \frac{\partial Q}{\partial t} = C_p \rho_0 \frac{\partial T}{\partial t} \quad , \tag{2.22c}$$

where Q is calculated as $Q = \int \sigma_{ij} d\varepsilon_{ij}$ with σ_{ij} and ε_{ij} in the calculation being the components of the local stress and plastic strain, respectively. Therefore Q is non-zero only near the shear bands in the model system under tensile deformation. Because of the localized nature of shear banding, plastic strains inside and near the shear bands could be much larger than the elastic strains. Thus Q is much close to the mechanical work and the contribution of elastic energy to Q can be neglected. The parameter β is the coefficient representing the percentage of conversion of mechanical work into heat, or the Taylor-Quinney coefficient. The situation $\beta = 1$ means the adiabatic

situation, while $\beta = 0$ represents isothermal deformation process. The parameter *k* is the thermal conductivity and C_p is the heat capacity. Therefore, the dynamic process of deformation and fracture behaviors in MGs can be described by solving Eqs. 2.22(a) ~ 2.22(c).

According to the phase-field model on bulk metallic glass [Zheng and Li 2009], the shear band propagation and branching have been successfully simulated in a rectangle sample with an initial crack perpendicular the loading direction. It is stated that the extension of shear band change with the amplitude of the applied load. When the stress intensity is moderate, the shear band occurs from the tip of the initial crack. The wavy shear band and branching occur when the load increases. All these phenomena observed during simulation are consistent with the experiment [Lowhaphandu and Lewandowski 1998].

2.4 Summary

Phase- field theory is a useful tool to study the mesoscopic properties of solids under external loading. Especially, it is an effective method to investigate the phase transition and structural ordering in the complicated structures. Shear banding, the

typical characteristics of the room-temperature deformation in MGs, can be considered as the structural transition between the ideal glass and the defective regions. The deformation modes can be determined through the competition between the creation of the new defects and the annihilation driven by the continuum strain or/ and thermal field. Thus it is feasible to study the deformation mechanism at room temperature in MGs through the phase-field theory. Compared with other methods, such as the molecular dynamics and the finite element method, the phase-field is a mesoscopic theory comparable with the length scale of the shear banding. It was proved that the dynamic features can be effectively captured by this model.

Thus the phase-field model is useful in probing the deformation mechanism in MGs, especially the localized plastic deformation at room temperature. It is suitable to introduce the model to simulate the shear banding in BMGs and BMG composites. The model is appropriate for both the 2D and 3D simulations, and the size effect can also be studied by this theory through choosing the suitable system parameters.

Chapter 3 Simulation of shear banding in porous bulk metallic glasses

Porous BMG is a fascinating amorphous alloy which aims to solve the problem of brittle fracture of BMG at room temperature. It has been found that the ductility could be improved by controlling the properties of the pores introduced into it, which can block shear band propagation or induce branching of shear bands. In this Chapter, the mechanism of the improved ductility is studied by phase-field modeling. In particular the interaction between the pores and the shear bands is elucidated through the simulation on the shear-banding behaviors in porous BMG with different characteristics of pores.

3.1 Background of research on porous BMGs

Metallic foam materials have amazing mechanical properties such as low density and Young's modulus, high specific strength, and high energy absorption capacity [Evans et al. 1998; Gibson and Ashby 1997; Ashby et al. 2000]. They have many engineering applications, such as energy absorption during the separation of spacecraft from space station, and screw protection in cab seats mounted in military vehicles and even in commercial automobiles [Evans et al. 1998; Gibson and Ashby 1997; Ashby et al.

2000]. On the other hand, metallic glasses exhibit distinguish mechanical properties such as high strength, corrosion and wear resistances. Thus porous BMGs have received increasing attention since they have the advantages of both metallic foams and metallic glasses [Brothers and Dunand 2004; Brothers and Dunand 2005b; Brothers and Dunand 2006; Schroers et al. 2003; Wada and Inoue 2003; Jayaraja et al. 2006; Lee and Sordelet 2006], and are found to be very promising in functional applications such as fluid filters, catalytic substrates, and biomedical implants.

With the development of the preparation techniques, the metallic foams with different properties (including the pore shapes, the volume fraction of pores and the distribution pattern of the pores) could be synthesized [Schroers et al. 2004; Brothers et al. 2005; Wada and Inoue 2003; Brothers and Dunand 2004; Jarayaj et al. 2006; Wada et al. 2007]. Without much degradation of their strength, the improved ductility was obtained through controlling the pore size and volume fraction [Brothers and Dunand 2005a; Brothers and Dunand 2005b; Inoue et al. 2007]. Through systematic study, it was found that there were branched and wavy shear bands in the porous BMGs under compression as shown in Figure 3.1 from SEM investigations [Inoue et al. 2007]. It was suggested that the resulting ductility came from the blocking and

branching functions of the pores that affected shear bands evolution. Another important reason of the improved ductility was that the pores acted as the stress concentrator, stimulating proliferation of shear banding. It was also found that the pore sizes and the pore volume fraction could significantly affect the ductility and the energy absorption of the porous BMGs, and even the geometry of the pores could affect their yield strength [Inoue et al. 2007]. Higher volume fraction of pores could improve the plasticity of the porous BMG but its strength might decrease. In order to develop porous BMGs with excellent mechanical properties such as a combined large fracture toughness and ductility, understanding the mechanism of interaction between the pores and the shear bands is important and could provide guidelines for the design of the porous BMGs.

Although significant advances in experiments have been made in the understanding of shear banding behaviors in deformed porous BMG, little is known about the interaction between the pores and shear bands, especially the evolution of shear band affected by the introduction of the pores. Thus in the following sections, we shall focus on the simulation of the interaction between the shear band and pores using the phase-field model [Zheng and Li 2009]. In the simulation, we will consider

different conditions of deformation of porous BMG such as the athermal shear banding, the shear banding with local heating, the vacuum pore and the pore filled with helium.

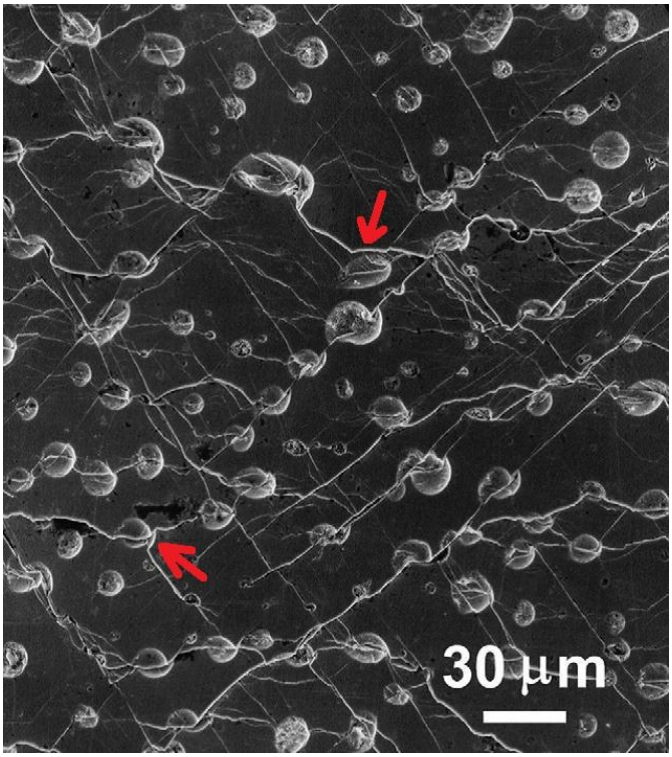

Figure 3. 1 SEM image of porous BMG sample subjected to 0.1 compressive plastic strain [Inoue et al. 2007].

3.2 Simulation details

According to the phase-field model [Zheng and Li 2009] as described in Section 2.3, the shear band propagation and the evolution of shear banding in porous BMG could be simulated by solving Eqs. 2.22(a) ~ 2.22(c). In this work, some typical examples are investigated to study the shear banding in the porous BMGs. A Zr-based BMG plate with dimensions of $20\times20\times2$ μm^3 is considered. One initial crack with length of

l_0=0.4 μm and a pore with a diameter of 2 μm are introduced prior to the tensile load applied in this BMG sample, as shown in Figure 3.2 (b). The tensile loads are applied perpendicular to the initial crack and on the boundaries. The materials properties are list as follows, the glass transition temperature T_g=625 K*;* the Young's modulus E=95 GPa; Poisson's ratio ν=0.35; the mass density ρ_0=6050 kg/m^3, the heat capacity c_p=475 (J/kg)K^{-1}, and the thermal conductivity k=5 (W/m)K^{-1}. The elastic strain limit under uniaxial tension is 0.02. The characteristic time of deformation defects activation is τ_ρ=0.25 ns.

One important parameter, the deformation defect activation energy ΔG proposed by Argon and Spaepen [Argon 1979; Spaepen 1977], is generally determined by the strain-rate-sensitivity of plastic flow at different temperature below T_g [Krishnanand and Cahn 1975]. This activation energy features the microscopic deformation behaviors of metallic glasses. In this work, ΔG is chosen as 4.6 eV at T=300 K for Zr-based BMG, equivalent to the energy barrier of deformation defect activation described in the phase-field model. The coefficients in Eq. (2.20) can be described as, a_0=4(2-T/T_g)ΔG, b_0=-24ΔG, c_0=16ΔG. Choosing a_1=-6 and b_1=6 aims to stabilize the activated deformation defect state at $\rho(\boldsymbol{r})$=1.0 under plastic deformation.

Remark: In order to differentiate the density of deformation defects, the density of the materials and the distance used in Section 3.3.1, the function notation $\rho(\boldsymbol{r})$ is used to represent the density of deformation defects in the chapter.

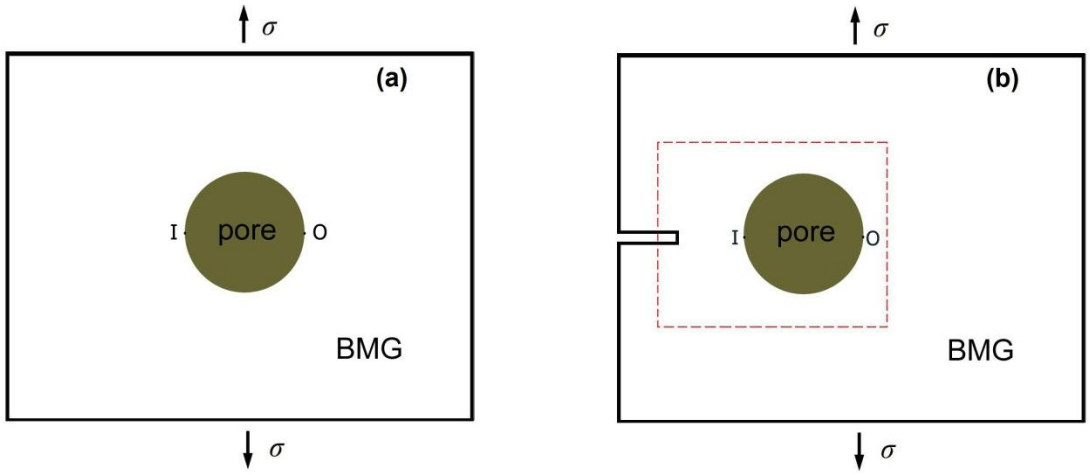

Figure 3. 2 (a) Schematic of the model system of porous BMGs. (b) Schematic of the model system with an initial crack. The length of the initial crack is l_0=0.4 μm. Tensile stress is perpendicular to the initial crack.

The boundary condition of Eq. (2.22b) at the pore surface is $\rho(\boldsymbol{r})=\rho_0$, and on the other surfaces of the porous BMG it is assumed that $\rho(\boldsymbol{r})=0$ except at the surfaces of the initial crack where $\rho(\boldsymbol{r})=1.0$ is used as boundary condition. Because $\rho(\boldsymbol{r})$ represents deformation defect density, ρ_0 between 0 and 1 could be a measure of the roughness of the pore surface. During the simulation, $\rho(\boldsymbol{r})=0$ represents the smooth surface of the pore, while $\rho(\boldsymbol{r})=1.0$ represents the rough surface of the pore. In order to solve the partial differential Eqs. 2.22(a) ~ 2.22(c), the length rescale factor $l_r = \sqrt{\kappa/\mu e_0}$ and time rescale factor $t_0 = l_r/\sqrt{\mu/e_0}$ are applied to make Eqs. 2.22(a) ~ 2.22(c)

dimensionless and they could characterize the length and time scales of the system, respectively. The parameter κ can be estimated from the surface energy γ by $\kappa = \gamma R$, and the characteristic length for Zr-based BMG is R= 0.56 μm [Zheng and Li 2009]. For the fracture surface of the $Zr_{41}Ti_{14}Ni_{10}Cu_{12.5}Be_{22.5}$ BMG, the surface energy was calculated as γ~1.97 J/m^2 [Zheng and Li 2009]. In the numerical analysis, triangles are used to discrete space domain and the backward differentiation formula (BDF) scheme is employed to discrete and integrate time. In order to investigate the fracture modes of this porous bulk metallic glass sample, the uniaxial tension loads are applied on the upper and bottom boundaries in the direction perpendicular to the initial crack, and the other edges are kept free. By solving Eqs. 2.22(a) ~ 2.22(c), shear banding in porous BMG could be investigated under different external loading conditions and pore microstructures.

Remark: It should be noted that if thermal effects or local heating are not considered, only Eq. (2.22a) and Eq. (2.22b) need to be solved simultaneously, otherwise, Eqs.2.22(a) ~ 2.22(c) are required to be solved simultaneously.

3.3 Simulated results

The pore can lead to the initiation of the shear bands and the shear band detouring

during the deformation of porous BMGs [Inoue et al. 2007]. The properties of the pores and local heating could also significantly affect the shear band propagation and evolution. Strain and stress distribution around shear band are key factors that affect shear band evolution. Thus in this section we first compare the strain distribution in porous BMG and that of the elastomer around the pores. Then we will investigate the stress distribution when the shear band touches the pore. Finally, effects of local heat around the pores with and without filling of gas on the shear banding are investigated.

3.3.1 Strain localization in porous BMGs under deformation

It is generally accepted that the deformation (the plastic strain) in BMGs is localized into the shear band. To understand the micromechanics of shear band, we compare the strain fields of a shear band which is just initiated at the position O with those of an elastomer containing a pore with the same size, which in the (ρ, θ) polar coordinate system are written as [Goodier 1933].

$$\begin{aligned}
\varepsilon_{\rho\rho} &= \frac{\sigma}{2E}(1-r_0^2/\rho^2) - \frac{\sigma}{2E}(1-r_0^2/\rho^2)(1-3r_0^2/\rho^2)\cos 2\theta \\
\varepsilon_{\theta\theta} &= \frac{\sigma}{2E}(1+r_0^2/\rho^2) + \frac{\sigma}{2E}(1+3r_0^4/\rho^4)\cos 2\theta \qquad , \qquad (3.1) \\
\varepsilon_{\rho\theta} &= \frac{\sigma}{2E}(1-r_0^2/\rho^2)(1+3r_0^2/\rho^2)\sin 2\theta
\end{aligned}$$

where r_0 represents the pore radius. The strains near shear band by taking O as the origin are shown in Figure 3.2. ρ is the distance between the point calculated and the origin O. θ represents the angle between the line (passing through the origin and parallel with the loading direction) and the line (passing through the origin and the point calculated). Through algebraic calculation, the normalized results including the normal and shear strains (marked as black) are derived and shown in Figure 3.3.

Then we consider the deformation of porous BMG system shown in Figure 3.2 (a) by solving Eqs. 2.22(a) and 2.22(b) with the interior boundary condition that the pore surface is rough, i.e., $\rho(\boldsymbol{r})=\rho_0=1.0$ on the pore surface. Shear bands could be initiated from two utmost positions labeled as O and I at the pore surface. Since the plastic strains in porous BMG can be taken as the differences between the strains of porous BMG and the elastomer, it can be seen that the plastic strains near shear band are highly localized and decrease with increasing distance to the origin following a relation much like an exponential function, which has been predicted by the theoretical model in Ref. [Zheng 2011]. Moreover, the strain components are almost zero at positions with $\rho>0.5r_0$ except the shear strain at positions with $\theta=\pi/2$.

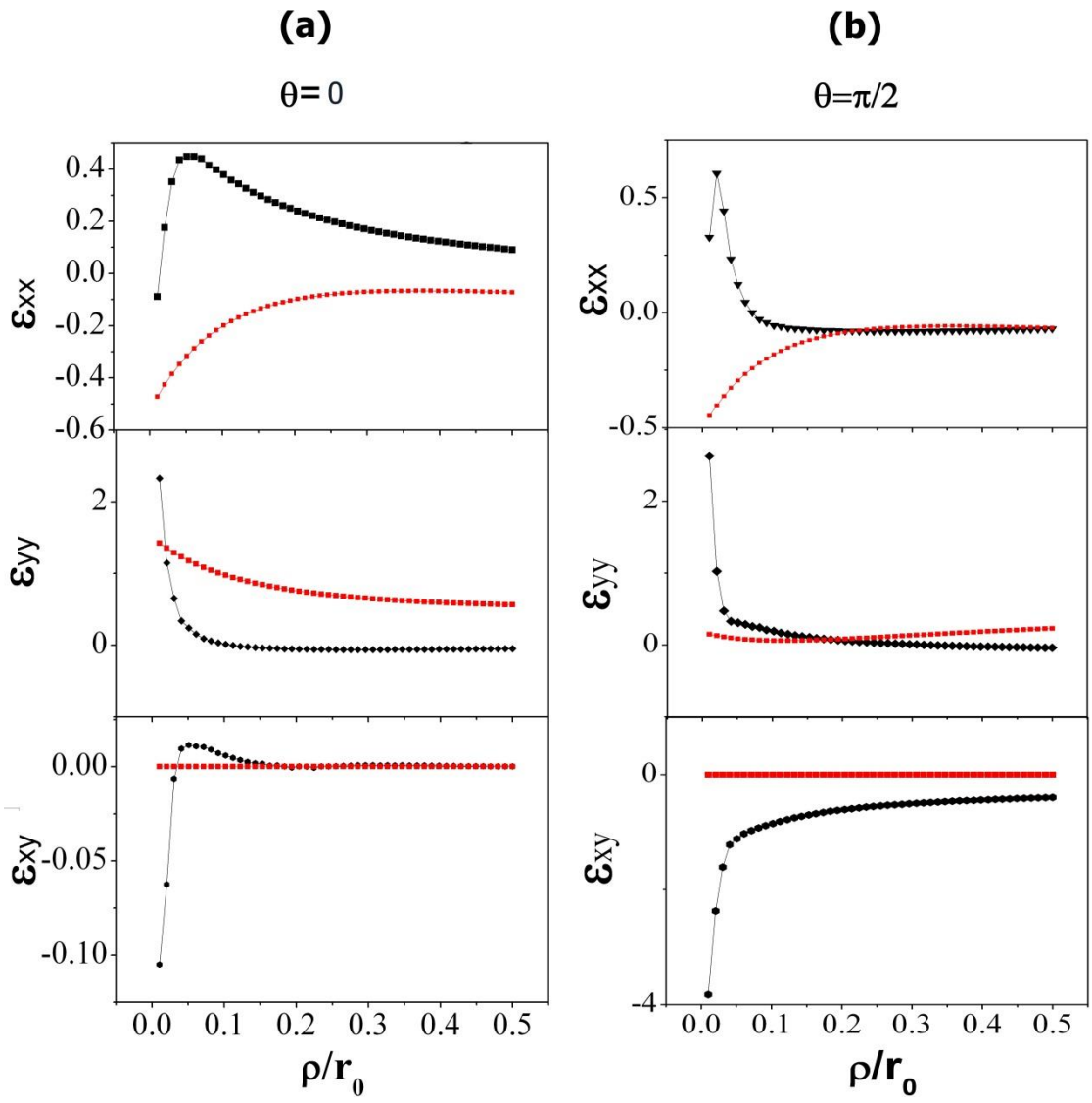

Figure 3. 3 The strain fields at a point (ρ, θ) near the shear band initiated from the pore surface. The red curves are those of an elastomer containing a pore.

3.3.2 Shear banding in porous BMGs without considering local heating

We first investigate shear banding without considering local heating and the deformation of porous BMGs is simulated using Eqs. 2.22(a) and 2.22(b). As shown

in Figure 3.2 (b), shear bands can be generated from an initiation crack, and then propagate along the direction perpendicular to the applied tensile stress σ. The presence of pores, certainly, will make the shear bands discontinuous.

From the simulation, we find out that there are two ways in which the discontinuous shear band extends in the porous BMG as shown in Figures.3.4 (a) and (b), which are denoted as mode-A and mode-B shear banding, respectively. When the pore surface is smooth ($\rho_0(\boldsymbol{r})\rightarrow 0$), shear band can be detoured by the pore where the shear band touches the pore which is observed in experiments [Inoue et al. 2007], resulting in mode-A shear banding. When the pore surface is rough $\rho_0(\boldsymbol{r})\rightarrow 1.0$, shear band is initiated from the side of the pore opposite to where the shear band touches the pore, resulting in mode-B shear banding, and the porous BMG is still brittle. The porous BMG with mode-A shear banding during deformation is considered as the material with improved ductility.

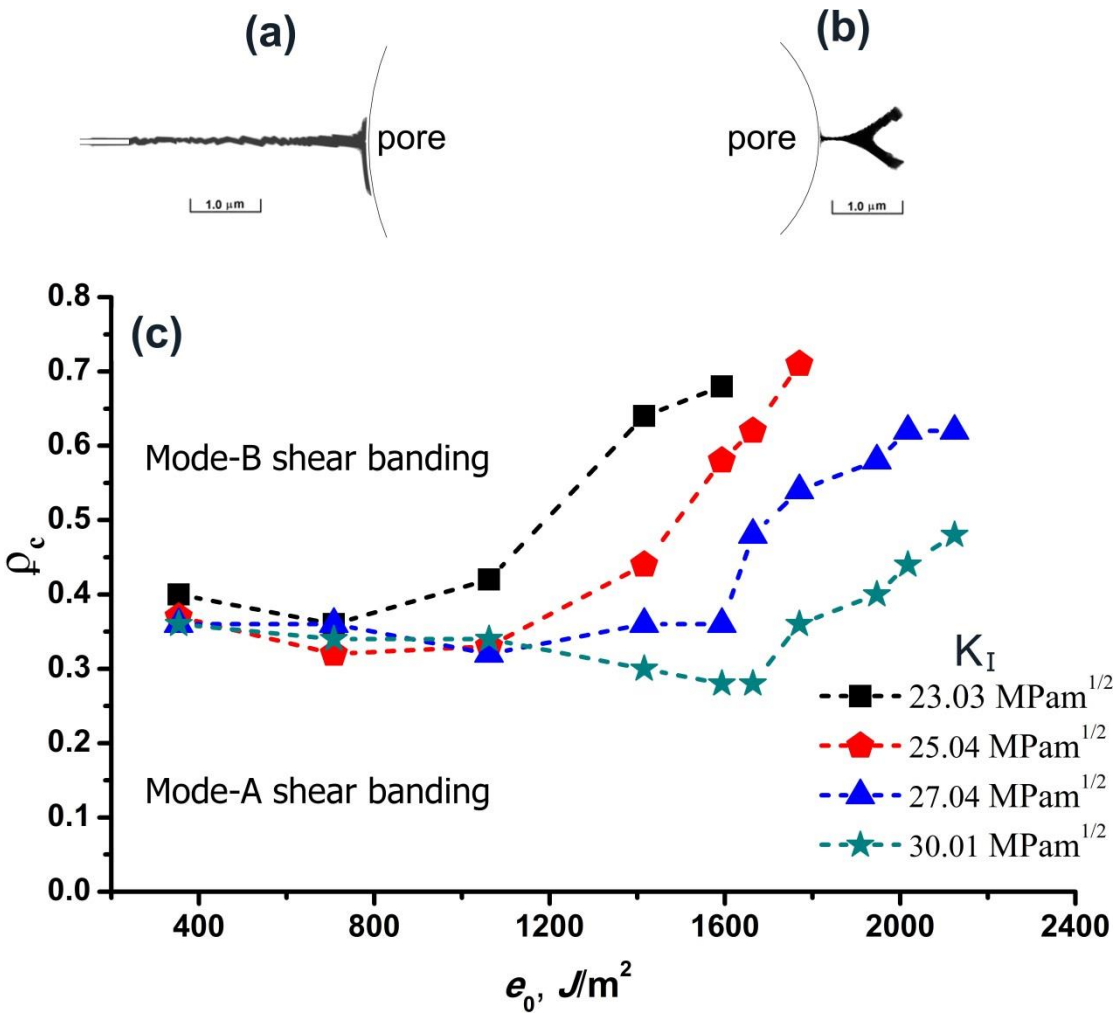

Figure 3. 4 (a) Mode-A shear banding: the shear band is impeded by the pore. (b) Mode-B shear banding: the shear band goes through the pore. Only porous BMG plate near the pore is shown and the length bar is indicated. (c) The critical $\rho_0(\boldsymbol{r})$(represented as $\rho_c(\boldsymbol{r})$) as a function of strain energy at the elastic limit e_0 under different stress intensity factors K_I.

Three factors, the applied tensile stress, the strain energy at the elastic limit e_0, and the roughness of the pores $\rho_0(\boldsymbol{r})$, actually control these modes. Under a fixed applied stress, mode-A shear banding changes into mode-B shear banding when the roughness of the pores $\rho_0(\boldsymbol{r})$ changes from 0 to 1.0, and there should exist a critical $\rho_0(\boldsymbol{r})$ represented as $\rho_c(\boldsymbol{r})$ for such transition of shear banding mode. In Figure 3.4(c), the $\rho_c(\boldsymbol{r})$ as a function of the strain energy at the elastic limit e_0 is shown for a given

applied stress. According to the curves shown in Figure 3.4 (c) for various applied stresses, it is seen that $\rho_c(\boldsymbol{r})$ is not significantly affected by e_0 and the applied stress when the strain energy at the elastic limit e_0 is smaller than 1062 J/m^2, and the critical roughness of the pore $\rho_c(\boldsymbol{r})$ is about 0.3-0.4. That means porous BMG with e_0 smaller than 1062 J/m^2 could be tougher if the pore surface is made to have a roughness $\rho_0(\boldsymbol{r})\leq 0.3$. On the other hand, the enhanced toughness of the porous MGs can still be kept with a little rougher surface when the strain energy at the elastic limit e_0 is larger than 1062 J/m^2. These results obtained can provide an important guideline for the design of porous BMG with enhanced fracture toughness.

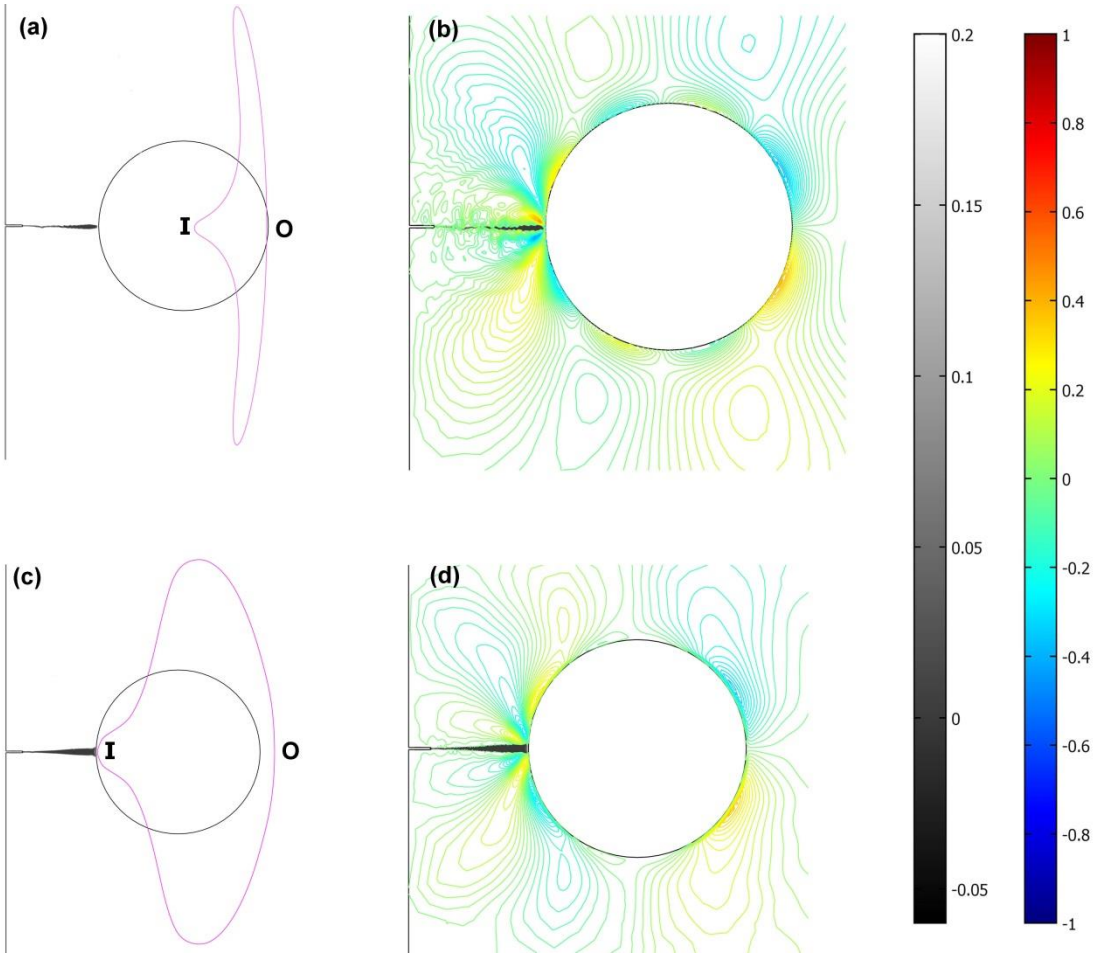

Figure 3. 5 (a) Pore surface before (colored in black) and after (colored in pink) mode-A shear banding. (b) Contour plots of shear stresses in mode-A shear banding. (c) Pore surface before (colored in black) and after (colored in pink) mode-B shear banding. (d) Contour plots of shear stresses in mode-B shear banding. The color bar is for the contour plots of shear stresses. The gray bar corresponds to the value of $1-\rho_c(\boldsymbol{r})$.

The deformation of the pore and the stress distribution around the pores are further analyzed when the shear band touches the pore for these two shear banding modes, respectively, as shown in Figure 3.5. In mode-B shear banding, shear stress on the pore surface is heterogeneous. Shear stress tends to build up at the side of the pore surface opposite to where the incident shear band touches the pore; and shear

stresses at other places on the pore surface are relaxed as shown in Figure 3.5 (d). The shear band could be initiated at the place marked as ‘O’ where the stresses concentrate on the pore surface. In mode-A shear banding, shear stresses are built up on several places on the pore surface and are relatively homogeneous as shown in Figure 3.5 (b), and no obvious stress concentration can be observed. The stress distribution after the interaction between the incident shear band and the pore can be further revealed by the change of pore geometry under the deformation caused by the stress field of the incident shear band. As shown in Figure 3.5 (c), in mode-B shear banding, the shear deformation of the pore surface is mainly at the side opposite to where the shear band touches the pore, which is marked as ‘O’. Thus shear band could be generated at ‘O’. On the contrary, in mode-A shear banding, shear deformation of the pore surface occurs at its side close to the shear band, which is marked as ‘I’. The shear band is thus impeded by the pore surface near the side marked as ‘I’, as shown in Figure 3.5 (a).

3.3.3 Effects of heat conduction around pores on shear banding

Although in what stage and in what form it is relevant to shear banding remains

unclear, local heating is an important characteristic of shear banding. In porous BMGs, local heating could play a dominate role in shear banding since shear bands will be significantly affected by the heat conduction conditions around the pores. For example, shear bands among vacuum pores could be generated by adiabatic deformation, while shear bands around pores filled with gases are formed in a relatively homogeneous thermal environment.

To investigate the shear banding by considering local heating, we solve the coupled equations Eqs. 2.22(a) ~ 2.22(c). The initial condition of heat conduction equation Eq. (2.22c) is T=300 K. Other conditions of Eqs. 2.22(a) and 2.22(b) are the same as those in Section 3.3.2.

3.3.3.1 Shear banding around vacuum pores.

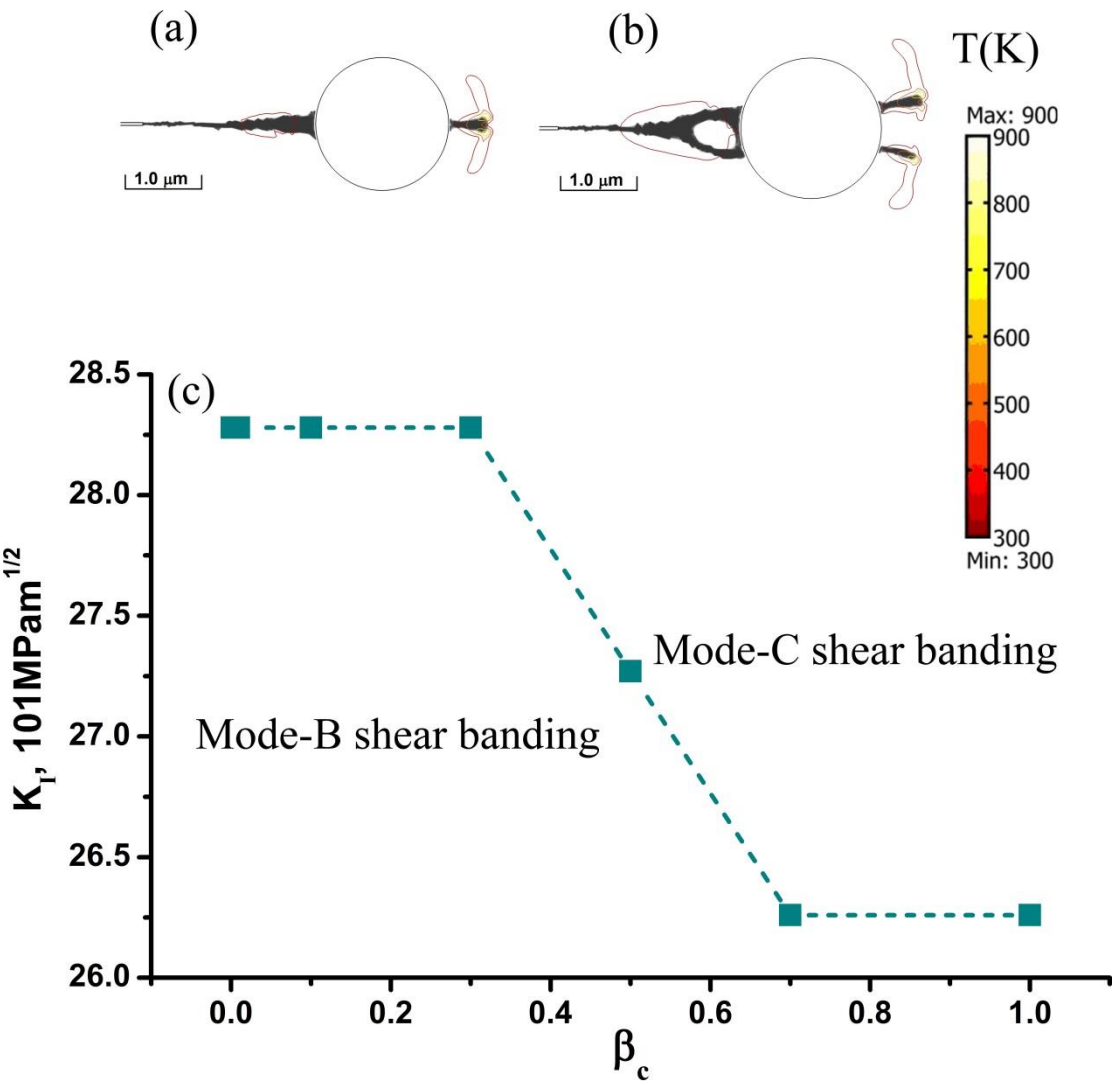

Figure 3. 6 (a) Brittle porous BMGs in mode-B shear banding. (b) Ductile porous BMGs in mode-C shear banding. (c) Brittle to ductile transition controlled by the coefficient β of mechanical work to heat conversion in porous BMGs with vacuum pores. The critical β (denoted as β_c) at which mode-B shear banding transforms into mode-C shear banding under a stress intensity factor K_I is plotted as diamond symbols. The color bar is for the contour plots of temperatures.

In the case that the pores are vacuum holes, it is found that the shear banding modes are related to a parameter β which is the percentage of mechanical work to heat conversion. There are two shear banding modes, named as mode-B and mode-C as

shown in Figures 3.6 (a) and (b) respectively. From the figures, it can be seen that the shear band is initiated directly from the side of the pore opposite to where the shear band touches the pore for mode-B. For the mode-C shear banding, the pore acts as sink and source of shear bands, resulting in shear band multiplication. Hence, porous BMG deformed in mode-C shear banding could have better ductility compared with that in mode-B shear banding. The decreases of β from 1 to 0 will change the shear banding from mode C to mode B under a fixed stress intensity factor.

To determine the conditions that porous BMG is deformed in mode-C shear banding, we plot diamond symbols in Figure 3.6 (c) indicating the critical β (denoted as β_c) at which mode-B shear banding transforms into mode-C shear banding under different stress intensity factors $K_I = \sigma\sqrt{\pi l_0}$. Hence the curve of $K_I \sim \beta_c$ denotes the boundary of brittle to ductile transition, and distinguishes modes-B and mode-C shear banding as discussed above.

3.3.3.2 Shear banding around pores filled with helium

In the previous section the pores in the porous BMG are considered as vacuum holes. While in fact those pores are made by blowing gas bubbles such as helium bubbles into the melts of alloys in producing porous BMG. Thus the pores could contain gas

which provides conduction paths for the heat generated by shear banding around the pores. Under this condition, the shear banding is studied in this part.

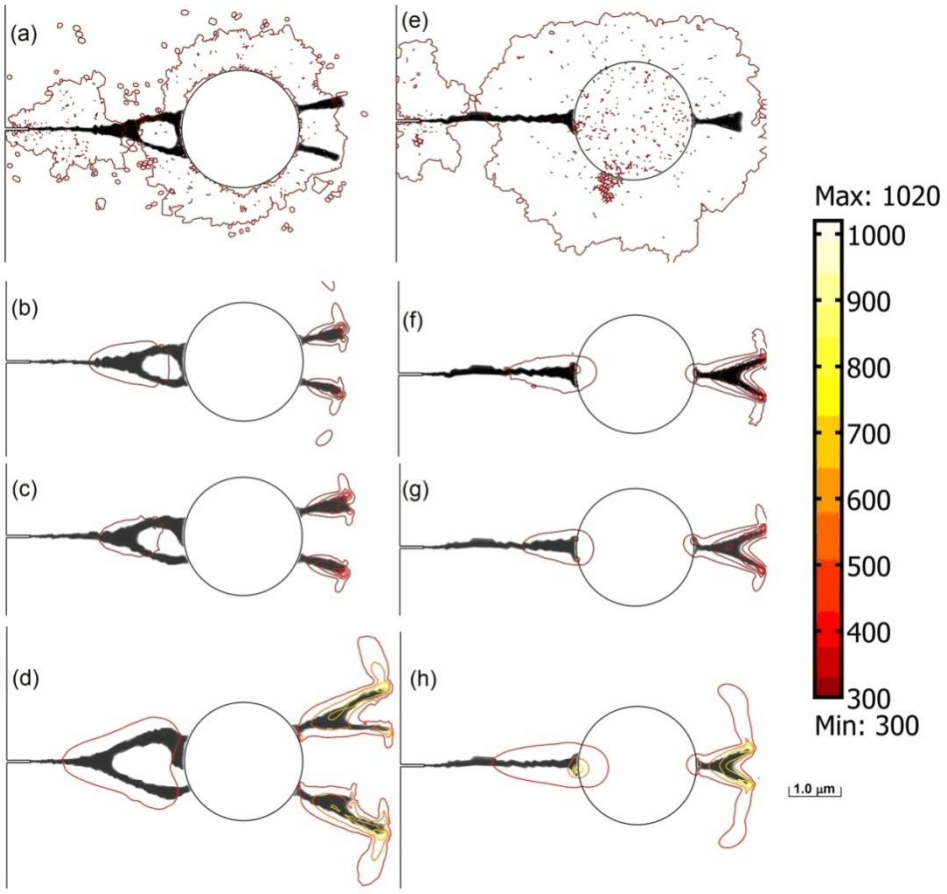

Figure 3. 7 Shear banding in BMGs with vacuum pores ((a)~(d) with β=0, 0.001, 0.1, and 1, respectively);and shear banding in BMGs with pores filled with helium ((e)~(h) with β=0, 0.001, 0.1, and 1, respectively). The color bar is for the contour plots of temperatures.

We consider porous BMG consisting of pores with a diameter of 2.0 μm. The pores are filled with helium at 100 kPa which has the physical properties as follows, thermal conductivity 0.152 W/(m ·K), heat capacity 5193 J/(kg ·K), and density 0.178 kg/m^3. The shear banding around pores filled with helium is shown in Figures 3.7 (e) ~ (h),

assuming the percentage of mechanical work to heat conversion to be β=0, 0.001, 0.1, and 1, respectively. The stress intensity factor is K_I=32 MPam$^{1/2}$ and surface roughness of the pore is $\rho_c(\boldsymbol{r})$=0.48. Under the same pore surface roughness condition and the same stress load, the shear bandings in porous BMG with vacuum pores are shown in Figures 3.7 (a) ~ (d) for comparisons when the percentages of mechanical work to heat conversion are β=0, 0.001, 0.1, and 1, respectively. The color bar represents the temperature value and the contour lines are shown in Figure 3.7. Comparing the features of shear banding and the temperature distribution around shear bands in porous BMGs with vacuum pores and with pores filled with helium, we can find that the helium filled in the pores significantly affects the shear banding behaviors in porous BMG, while the temperature distribution around shear bands is not much affected. Obviously, porous BMG with pores filled with helium deforms in mode-B shear banding and its ductility could be less than that of porous BMG with vacuum pores.

3.4 Discussions

It should be noted that the introduction of the pores into the BMG can significantly change the stress distribution, which is obvious around the pore [Inoue et al. 2007].

The main function of the pore is to confine the instable shear band propagation and increase the shear band densities, resulting in the improved ductility of the porous BMG. It should be noted that the asymmetry of tension and compression around the pores should affect the deformation mode. It is well known that compressive stress could prevent the crack extension. The failure of materials is usually caused by the combination of the normal and shear stresses in porous BMGs under tensile loading. There are two kinds of porous BMGs, i.e. the open-cell [Brothers & Dunand 2005a; Brothers & Dunand 2005b; Brothers et al. 2005] and the closed cell porous BMGs [Inoue et al. 2007]. The deformation mechanism should be different for these two kinds of porous BMGs, since the surface roughness and the heat conduction of these porous BMGs are different. The local heating is another important factor affecting the deformation mechanism. Thus in the present phase-field modeling, the roughness of the pore surface, the gas filled in the pore and local heating are chosen as the factors rather than the fraction of pores to investigate the deformation mechanisms of the porous BMGs, which are different with those used in other numerical simulation and experimental investigations. For example, in this work, the surface smoothness is reflected through the definition of boundary condition. The results successfully describe the deformation behaviors of the pores in the BMGs,

which is consistent with the results in the experiments [Brothers & Dunand 2005b].

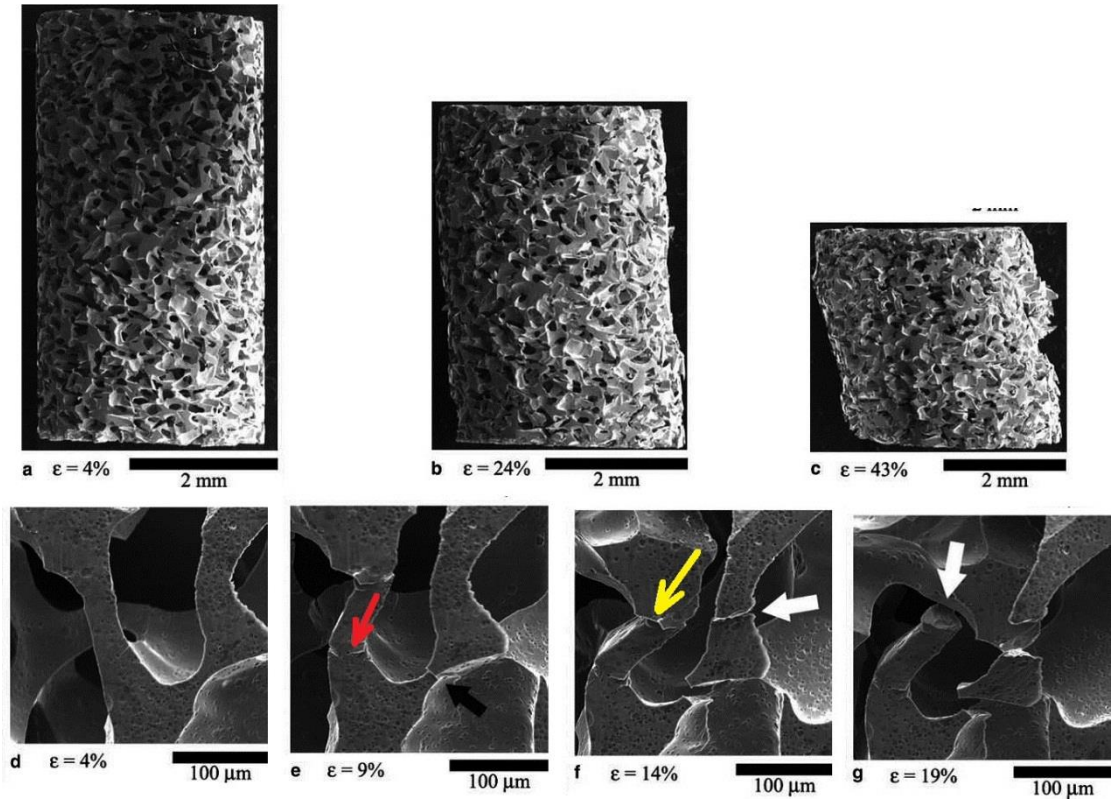

Figure 3. 8 SEM micrographs illustrating mechanisms of compressive deformation in Vit106 foam (pore size 230 μm and relative density 23%). Low-magnification images show foam structure following unloading from various applied macroscopic strains: (a) low strain (4%); (b) intermediate strain (24%); (c) high strain (43%). Also shown are deformed structures within the sample following unloading from: (d) 4% strain; (e) 9% strain; (f) 14% strain; (g) 19% strain. Visible fractures are indicated by arrows where they first appear [Brothers and Dunand 2005b].

In Figure 3.8 (e), we can see several cracks occur during the compressive deformation of the porous BMGs sample. Besides the shear fracture marked by the black heavy arrow, the crack marked by the red arrow should be caused from the surface of the pore, similar with the mode-B shear banding (as shown in Figure 3.4 (b)) observed in our simulation which could be affected significantly by the surface

roughness of the pore. It can be found in Figures 3.8 (e) and (d) that, the deformation of pores under larger strains (at the arrival of the crack initiation at the left hand side of the pore) is consistent with the simulation results (as shown in Figure 3.5 (c)). When the strain is further increased, the crack at its left hand side marked by yellow arrow in Figure 3.8 (f) gets through the pore and results in the crack at the right hand side of the pore which is marked by the white heavy arrow. Different from mode-B shear banding in our simulation, this crack is accompanied by other cracks as denoted by the heavy black arrow in Figure 3.8 (e).

3.5 Conclusions

Shear banding in porous BMG is investigated by phase-field modeling. The surface roughness of the pores, the gas filled in the pores and the elastic limit and strain energy at the elastic limit in the matrix may affect the shear banding in porous BMG. The modeling provides quantitative measures on these parameters that determine different modes of shear banding. Under different preparation methods, the pores in the porous BMGs shall be greatly different, which may affect the plasticity of the materials by various mechanisms. The investigation on these factors can play an important role in the design of new kinds of BMG materials with improved ductility

for structural applications.

During the simulation, two main modes of shear banding are found to be responsible for the improved ductility in porous BMGs. One is the prevention of shear banding when the closed pores possess smooth surfaces. The other is the occurrence of the new shear bands due to the heterogeneous local heating when the closed or open pores are filled with gases which are less effective in conducting heat. In this study, it is quantitatively determined that the characteristics of BMG such as the strain energy at the elastic limit should be combined with features of the pores such as their surface roughness to achieve ductility of the porous BMG.

Chapter 4 Simulation of shear banding in BMG composites containing *in-situ* formed dendrite phases

4.1 Introduction

During the development of BMGs, considerable efforts have been devoted to cope with the catastrophic fracture resulting from the occurrence of the shear banding. Even some BMGs exhibit high strength and fracture toughness, the brittle failure pattern caused by the absence of ductility would also occur in unconstraint loading geometries [Rao et al. 2001]. Various kinds of BMG composites containing quasicrystals, intermetallic or ductile dendrites have been developed, such as Ti-based [He et al. 2003a; Louzguine et al. 2004], Zr-based [Das et al. 2003] and Fe-based BMGs [Gu et al. 2006; Yao and Zhang 2007]. Especially it was noted that significant improvements on the ductility were reported from the experiments by introducing microstructural dendrite phases [Pekarskaya et al. 2001; Hays et al. 2001, Hofmann et al. 2008a]. It was suggested that the restriction and bifurcation of shear bands caused by the dendrites may play an important role in the improved ductility. The effects of the volume fraction of dendrites and their distribution

patterns were investigated. The results showed that the properties of the crystalline dendrites could influence the deformation modes of the system by disturbing the shear band evolution paths. Nevertheless, the theoretical studies on the shear banding around the dendrites, which could provide guidelines for the design of BMG composite with *in-situ* formed dendrite phase, are still considerably limited. For example, it is still not clear how the relevant parameters of the dendrites such as their microstructure (patterns of the arms of the dendrites), shape and dispersion pattern (relative rotation angle with respect to the initial shear bands) affect the mechanical properties in the microscopic scales, which are difficult to be detected through the experiments.

In this work, we focus on the evolution of shear band and the interaction between the shear banding and the crystalline dendrite especially when it touches the crystalline phase. The mechanisms of improved ductility and the dynamic evolution of shear band are numerically investigated based on the phase-field models in the Zr-based BMG composite containing *in-situ* formed β-Zr_2Cu dendrites [Zheng and Li 2009]. It is found that there are some factors influencing the shear band propagation, such as the properties of the dendrite phase, especially the rotation

angle, the structural features of the dendrites and the fracture energy of BMG matrix. Some important features can be observed in the microscopic scale, , such as the detouring and branching of shear band due to interactions between the shear bands and the dendrites , , which help us to investigate the origin of improved ductility and provide guidance for the design of BMG- composites with improved fracture toughness and ductility.

4.2 Phase-field models used for the simulation

The phase-field model on the shear banding in BMG matrix is the same as that used in Chapter 3 and has been introduced in Chapter 2. In the present study, Eqs. 2.22(a) and 2.22(b) are used to investigate the shear banding in the BMG matrix and the local heat is not considered.

Since it is an important step to model crystalline dendrite structure formation in our simulation, the phase-field modelling methodology for the dendrite solidification will be presented in the section that follows. We will also present the phase-field modeling method that is used for the simulation of cracking in crystalline dendrites.

4.2.1 Phase-field modeling on solidification of dendrite

Dendritic structure is commonly observed in solidification of alloys. Its shape is usually very complicated. The phase-field model based on Elder's solidification theory [Provatas and Elder 2010] has been successfully developed to describe the dendritic pattern formation.

The order parameter $\varphi(\mathbf{x})$ is employed to represent the phase transformation during the solidification. It ranges from -1.0 to 1.0. The value -1.0 corresponds to the liquid phase while φ=1.0 represents the solid phase. By introducing the order parameter $\varphi(\mathbf{x})$, the free energy of a binary alloy has been proposed as a function of the solid-liquid order parameter field $\varphi(\mathbf{x})$, the usual solute concentration field $c(\mathbf{x})$, and the temperature field $T(\mathbf{x})$. The equation can be described as,

$$\Delta F = \int_v \left\{ \frac{\left|\varepsilon_c \nabla c\right|^2}{2} + \frac{\left|\varepsilon_\varphi \nabla \varphi\right|^2}{2} + f(\varphi, c, T) \right\} dV \quad , \tag{4.1}$$

where $\varepsilon_c = \sqrt{H} W_c$ and $\varepsilon_\varphi = \sqrt{H} W_\varphi$ are the constants used to set the scale of the solid-liquid and compositional domain interface energy, respectively. W_φ and W_c are used to define the length scales of the solid-liquid interface and a compositional boundary, respectively. H is the nucleation barrier which controls the activation

between the liquid and solid phases at the melting temperature. When the components A and B have the similar atomic radius, then H_A=H_B≡H. The first and second terms in the integral represent the interfacial effects from the concentration and different structure state, respectively. The third term is the free energy density from the bulk effects. For alloy with only one solid phase, such as the β-Zr_2Cu, the free energy density $f(\varphi, c, T)$ can be described as,

$$\begin{aligned} f(\varphi,c,T) = & (f_L(T_A)-(T-T_A)s_A^L)(1-c)+(f_L(T_B)-(T-T_B)s_B^L)c \\ & -(\frac{L_A(T_A-T)}{T_A}(1-c)+\frac{L_B(T_B-T)}{T_B}c)P(\varphi) \\ & +Hg(\varphi)+RT\{(1-c)\ln(1-c)+c\ln c\} \end{aligned} \quad , \qquad (4.2)$$

where, T_A and T_B represent the melting temperature of the component A and B, respectively, L_A and L_B are the latent heats of constituent A and B, respectively. s_A^L and s_B^L mean the bulk entropy densities of A and B in liquid state, respectively. $P(\varphi)$ is an interpolation function satisfying the limits $P(\varphi=\varphi_L)=0$ and $P(\varphi=\varphi_s)=1.0$. The interpolation function $g(\varphi)$ is a phenomenological expression with limits $g(\varphi\rightarrow\varphi_L=0)=0$ and $g(\varphi\rightarrow\varphi_s=1.0)=1.0$. The logarithmic terms denote the mixing entropy contribution to free energy.

During the kinetic solidification of alloy, it should be noted that the microstructure is govern by the order parameter, concentration of impurity and the temperature.

However, the diffusion of heat occurs much more rapidly than the diffusion of solute impurities in a binary alloy at the low solidification rates. As a result, the temperature can be considered as "frozen" in the timescale of mass transport, which becomes the rate-limiting step in the solidification process. Under these conditions, it is reasonable to consider only the dynamics of solute diffusion and solid-liquid order parameter field. The changes in solute concentration are governed by the well-known mass conservation equation,

$$\frac{\partial c}{\partial t} = D_L \nabla \cdot \left\{ q(\varphi, c) \left(\frac{\partial \overline{f}_{AB}^{mix}(c,\varphi)}{\partial c} - \varepsilon_c^2 \nabla^2 c \right) \right\}, \tag{4.3a}$$

where

$$q(\varphi, c) = Q(\varphi) / \frac{\partial^2 \overline{f}_{AB}^{mix}(c,\varphi)}{\partial c^2}$$

with $Q(\varphi)$ being used to interpolate the mobility between different phases. $f_{AB}^{mix}(c,\varphi)$ is the free energy density of the material consisting of atoms A and B as described by Eq. (4.2). D_L is the diffusivity of the liquid.

According to the assumption of dissipative dynamics and the fact that the order parameter in solidification is a nonconserved quantity (i.e., an undercooling liquid can crystallize), the equation describing the dissipative dynamics of the phase field can be stated by using the variation of the free energy as,

$$\tau \frac{\partial \varphi}{\partial t} = -\frac{\delta F}{\delta \varphi} = W_{\varphi}^{2} \nabla^{2} \varphi - \frac{dg}{d\varphi} - \frac{1}{H} \frac{\partial \bar{f}_{AB}^{mix}(c, \varphi)}{\partial \varphi} \quad , \tag{4.3b}$$

By solving Eqs. 4.3(a) and 4.3(b), the shape of the solid phase formed in the melt of binary alloy could be obtained by extracting the boundary defined as φ =0 between the liquid and solid phase. The growth of dendrite boundary can be efficiently simulated.

In this work, β-Zr_2Cu crystalline dendrite has been developed by numerically solving Eqs. 4.3(a) and 4.3(b). The properties of β-Zr_2Cu crystalline are as follows: the melting temperature T_M=1726 K, the latent heat L=2.311×10^9 J/m^3, the heat capacity c_p=5.313×10^6 J/(m^3K), the diffusivity D_L=10^{-5} m^2/s. By using the numerical methods, e.g., the finite difference method, the growth of dendrite boundary can be efficiently simulated.

4.2.2 Phase-field modeling on crack propagation in crystalline phase

In the BMG composites, the adhesion between the secondary phase and the BMG matrix is assumed perfect, resulting in the continuous displacement at the dendrite-BMG interface. Shear bands in the BMG matrix can be bifurcated or

detoured by the arms of dendrite phase, or can pass through the crystalline phase. Fracture of the crystalline phase should be simulated if shear bands pass through the dendrites. Although the fracture and cracking in crystalline solid are complicated because of the dislocation involved in the process, the dynamic cracking has been modeled successfully by using phase-field approaches [Karama et al. 2001; Karama and Lobkovsky 2004]. The detailed model has been described in Section 2.1. Accordingly, the deformation and fracture in the crystalline phase could be denoted by numerically solving Eqs. 2.6(a) and 2.6(b).

The deformation in the BMG composites can be simulated by combining the equations describing the deformation in BMG matrix and the equations describing the deformation and fracture in the crystalline phase. The simulation of shear banding can be derived by numerically solving the differential equations, Eqs. (2.6) and Eqs. (2.22).

4.3 Simulation details

In the present simulation, Zr-based BMG containing β-Zr_2Cu dendrites will be considered. The simulation details of the Zr-based BMG matrix and β-Zr_2Cu

dendrites will be firstly introduced in this section. Then the simulated results shall be discussed about the patterns of the dynamic evolution of the shear banding.

4.3.1 Simulation details of Zr-based BMG matrix

A Zr-based BMG plate with dimensions of 20×20×2 μm^3 shall be considered and chosen as the matrix in the simulation. An initial crack with length of 0.4 μm, as shown in Figure 4.1 (a), is introduced. The materials properties of Zr-based BMG are as follows. Glass transition temperature: T_g=625 K; Young's modulus: E=95 GPa; Possion's ratio: ν=0.36; Density: ρ_0=6050 kg/m^3. Elastic strain limit under uniaxial tension: ε_{limit}=2%. Characteristic time of deformation defect activation: τ_ρ=0.25 ns. The elastic energy at the elastic limit has been chosen as e_0=38 J/m^2.

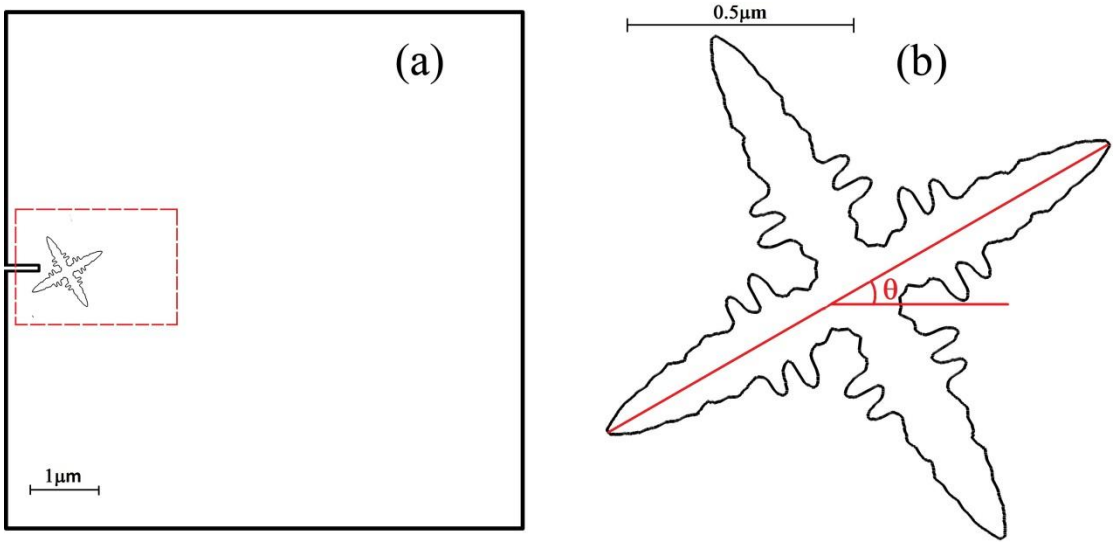

Figure 4. 1 (a) Model system of BMG-composite plate (20 μm ×20 μm×2 μm). The dashed box is the area of the composite to be shown in Figures (4.2) ~ (4.5). (b) The geometry of dendrite phase. θ is the rotation angle.

The coefficients in Eq. (2.20) are given by a_0=4ΔG (2-T/T_g), b_0=-24ΔG, c_0=16ΔG, where the deformation defect activation energy ΔG is estimated as 4.6 eV at room temperature [Lu et al. 2003]. The coefficients a_1=-6 and b_1=6 are chosen to quantitatively present the phase transformation of deformation defects in glassy alloy under deformation. According to the chosen coefficients, the shear modulus tends to zero when $\rho(\boldsymbol{r})\rightarrow 1.0$, which describes the shear softening and fracture in the glassy alloy. Then the critical density of deformation defect is defined as 0.8 to distinguish the shear softening regions from the remaining elastic medium.

The length rescale factor $l_r = \sqrt{\kappa/\mu e_0}$ and time rescale factor $t_0 = l_r/\sqrt{\mu/\rho_0}$ are applied to Eq. (2.22) to make it dimensionless and feature as the length and time scales of the system, respectively. The parameter κ can be estimated from the surface energy γ by $\kappa = \gamma R$, and the characteristic length for Zr-based BMG is R=0.56 μm [Zheng and Li 2009]. For the fracture surface of the $Zr_{41}Ti_{14}Ni_{10}Cu_{12.5}Be_{22.5}$ BMG, the surface energy was calculated as γ~1.97 J/m^2 [Zheng and Li 2009]. The dimensionless equation can be solved numerically. Triangles are used to discrete space domain and the backward differentiation formula (BDF) scheme is employed to discrete and integrate time in the numerical

analysis. The uniaxial tension load is applied on the top and bottom boundaries perpendicular to the initial crack.

4.3.2 Simulation details of dendrite phase

In order to investigate the interaction between the shear band and the crystalline dendrite in microscopic scale, it is necessary to introduce the β-Zr_2Cu dendrite phase into the simulation sample. The framework of the β-Zr_2Cu dendrite phase is formed through the numerical simulation as described in Section 4.2.1. As shown in Figure 4.1 (b), the dendrite with two small secondary arms is developed in the present simulation. The dimension of the dendrite is about 1.2 μm. The properties of β-Zr_2Cu crystalline phase are as follows: Young's modulus: E=121 GPa [Chen et al. 2009], Possion's ratio: ν=0.28. Elastic strain limit under uniaxial tension: ε_{limit}=2%.

In the present study, two values of the fracture energy of the dendrite, i.e., e_c=48.4 J/m^2 and e_c=145.2 J/m^2, have been chosen for analysis. Four rotation angles i.e., 0 º, 15 º, 30 º, and 45 º have been chosen for considerations, which describe the relative position between the initial shear banding and the primary arm in this dendrite phase and are marked θ in Figure 4.1 (b).

4.3.3 Simulated results

4.3.3.1 The morphology of dendrite phase

The typical morphology of the dendrite phase is shown in Figure 4.1 (b). The dendrite structures are characterized by the primary dendrite axes with lengths of 1.2 μm. It is noted that the secondary arms are regularly patterned in spacing of 0.1 μm. It can be found that the patterns of the dendrite phase obtained from phase-field simulation are consistent with the β-Zr_2Cu dendrites observed in electronic microscopy [Hofmann et al. 2008a], in particular the secondary arms can be well distinguished from the primary arms of the dendrites.

4.3.3.2 The shear band evolution

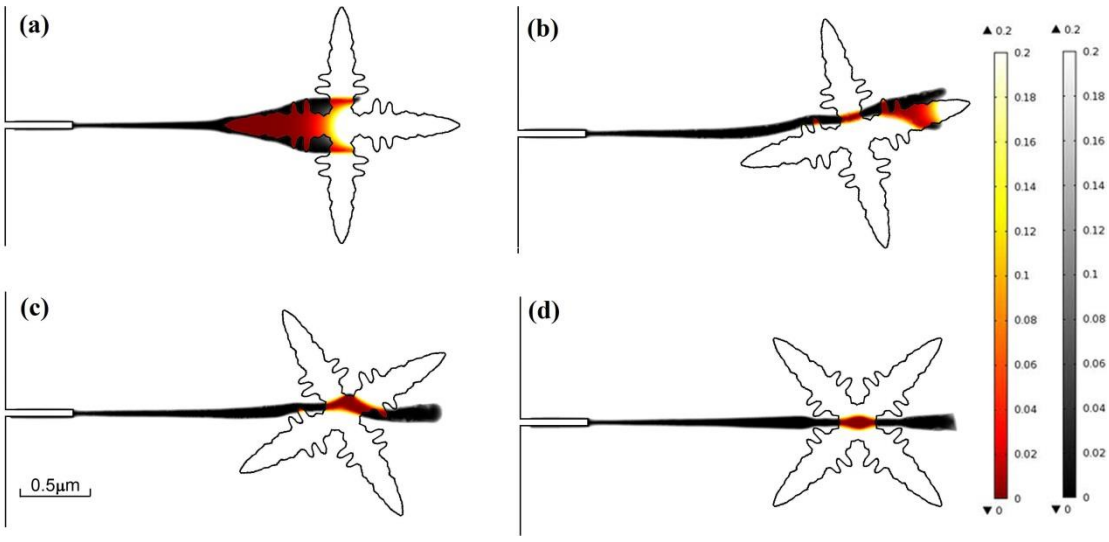

Figure 4. 2 Shear banding in BMG composite containing dendrite phase with a fracture energy e_c=48.4 J/m^2, (a) θ=0 º, (b) θ=15 º, (c) θ=30 º, (d) θ=45 º. The colour bar represents the values of 1-ϕ in the dendrite, and the gray bar corresponds to the values of 1-ρ in the BMG matrix.

For the Zr-based BMG composites containing β-Zr_2Cu dendrite phase whose fracture energy is approximated as e_c=48.4 J/m^2, the interactions between the shear bands and the secondary phases with four different rotation angles (θ=0 º, 15 º, 30 º, and 45 º) which describe the relative positions between the initial shear bands and the primary arms of dendrite, are shown in Figure 4.2. If the rotation angle is θ=0 º, the shear band gets close to the primary arm's tip of the dendrite. Then cracking occurs in the dendrite as shown in Figure 4.2 (a). The cracking area of the dendrite is so large that shear bands are also generated in the BMG matrix close to the tip of the primary arms. It is noted that the interaction results in not only crack propagation in the dendrite, but also the extension of incident shear band in the BMG matrix. This interesting phenomenon suggests that under mechanical deformation the presence of dendrite phase in the BMG matrix leads to more fracture surfaces in the dendrite and more shear bands in the BMG matrix which could accommodate more plastic strains and the ductility of the composite could increase. In the case of the rotation angle θ=15 ºas shown in Figure 4.2 (b), when the shear band gets close to the secondary arms of the dendrite phase, its propagation direction is changed a bit by the secondary arms before it generates fracture surface in the primary arm. The crack passes through one of the primary arms of the dendrite and induces shear banding in the matrix, accompanying

by an additional crack which passes through the other primary arm of the dendrite. More shear bands could also be generated in the BMG matrix close to the cracking areas of the primary arms. Similar with the case of $\theta=0^{\circ}$, the ductility may increase since more fracture surfaces are generated in the dendrite and more shear bands are generated in the BMG matrix. If the rotation angles are $\theta=30^{\circ}$ and 45° as shown in Figures 4.2 (c) and (d), respectively, the shear bands in the BMG matrix and cracks in the dendrite propagate almost along a straight line, without obvious bifurcation and detour. In all four cases, it is found that the cracks can be generated in the dendrite phase and they propagate easily. These phenomena could be caused by the fact that the strain energy at the elastic limit of BMG e_0 (38 J/m^2) and the fracture energy of the dendrite e_c (48.4 J/m^2) are similar. From the simulation, we can conclude that when $\theta<30^{\circ}$, the improved ductility could result from the shear band multiplication near the dendrite and the accommodation of plastic deformation by the dendrite. While the improved ductility only results from the accommodation of plastic deformation by the dendrite when $\theta>30^{\circ}$. These features show good agreement with the experiment results [Pekarskaya et al. 2001; Hays et al. 2001; Hofmann et al. 2008a], which justify the application of phase-field modeling in the analysis of shear banding in BMG composites in the mesoscopic scales.

It could be important in the design of BMG composites with even better ductility if we investigate the shear banding in the BMG composites containing crystalline dendrite phases with larger fracture energy. Hence we further consider the case when the crystalline dendritic phase possesses a fracture energy much larger than that of the BMG matrix, for example, in the Zr-based BMG composite reinforced with secondary phases showing phase transformation induced plasticity such as the Ni-Ti phase. In the simulation we assume these secondary phases possess the same model parameters in Eq. (2.6a) as those of β-Zr_2Cu dendrites except their fracture energy.

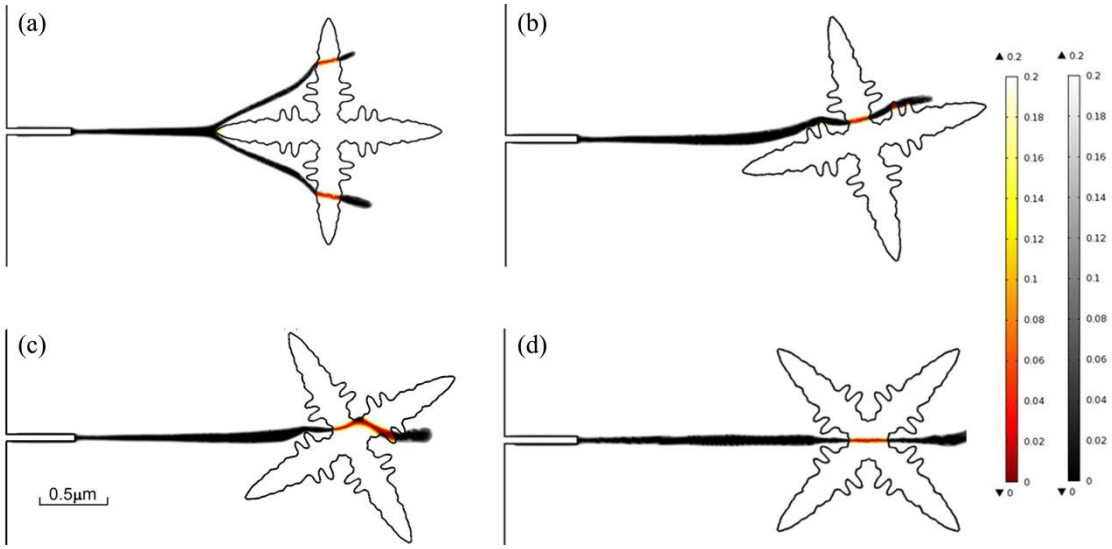

Figure 4. 3 Shear banding in BMG composite containing dendrite phase with a fracture energy e_c=145.2 J/m^2. (a) θ=0 º; (b) θ=15 º; (c) θ=30 º; (d) θ=45 º. The colour bar represents the values of 1-ϕ in the dendrite, and the gray bar corresponds to the values of 1-ρ in the BMG matrix.

When the dendrite has the fracture energy e_c=145.2 J/m^2 much larger than e_0 of BMG

matrix, much obvious bifurcation and detour of shear bands can be seen as shown in Figure 4.3. When the rotation angle is $\theta=0^{\circ}$ as shown in Figure 4.3 (a), shear band branching occurs when the shear band touches the primary arm of the dendrite. The branches of the shear band then induce fractures of other arms. At $\theta=15^{\circ}$, the dendrite's secondary arms could cause the detouring motion of shear band around the dendrite before and after the shear band induces fracture in the dendrite, as shown in Figure 4.3 (b). In the cases of $\theta=30^{\circ}$ and $\theta=45^{\circ}$, no obvious bifurcation and detour of shear band have been observed, as shown in Figures 4.3 (c) and (d), respectively, and there is no shear band multiplication near the dendrite.

From the above-mentioned simulated results, some useful features about the interaction between the shear bands and the dendrites are summarized as follows. First, the tips of the primary and secondary arms of the dendrite play a major role in the branching and the detour of shear bands. Thus, properly controlling the dendrite dispersion pattern could be helpful in accommodating plastic strains by the dendrite and the ductility of the composite could be enhanced. Second, the branching and the detour of shear bands are much obvious in composite containing dendrite with high fracture energy, resulting in the accommodation of more plastic strains by the BMG

matrix. It is difficult for the incident shear bands to induce fractures in the crystalline phase when the fracture energy of the dendrite phase is high and the branching and detour of shear bands could occur. Third, when the fracture energy is low, cracks are easily generated and they propagate in the dendrite phase after the shear bands interact with the dendrites. Cracks at different places of dendrite further promote the shear banding close to the dendrite, resulting in shear band multiplication which also plays a significant role in enhancing the ductility of the BMG composite.

4.3.3.3 The maximum shear stress fields

In order to further reveal the mechanisms of improved ductility in BMG composites, the maximum shear stress fields defined as $\tau = \sqrt{(\sigma_{xx} - \sigma_{yy})^2 + \sigma_{xy}^2}$ are analyzed as shown in Figure 4.4, where σ_{ij} are stress components around the dendrite with fracture energy e_c=145.2 J/m^2.

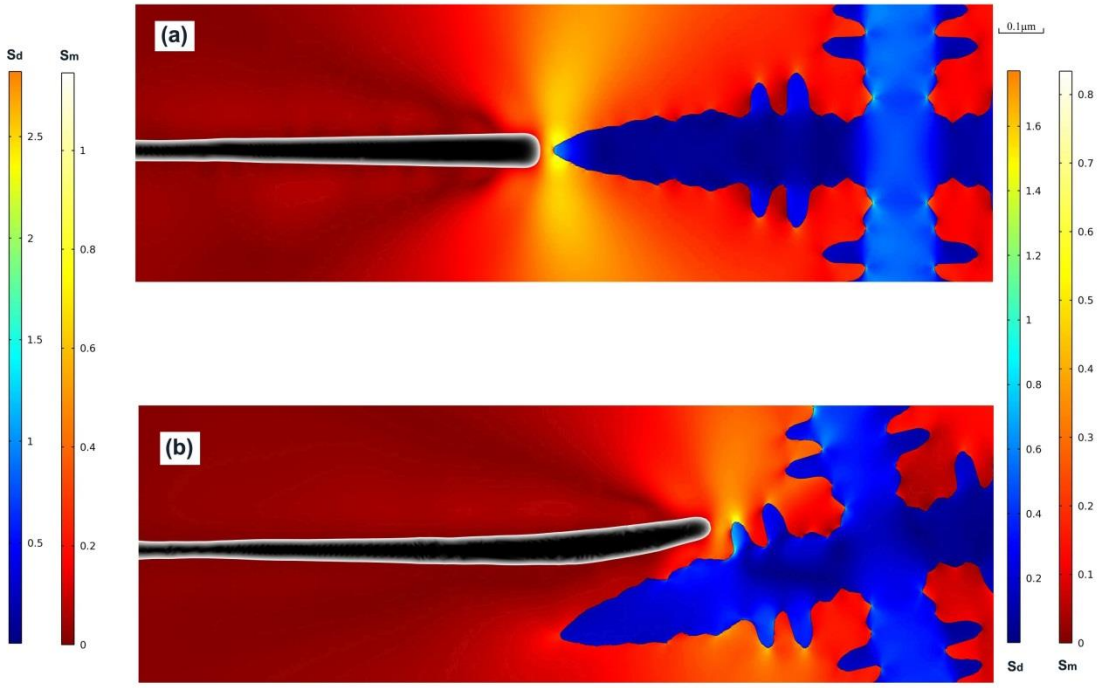

Figure 4. 4 Surface plots of shear stress fields in BMG composite containing dendrites with fracture energy e_c=145.2 J/m^2: (a) The rotation angle θ=0 º. The color bars marked as Sm and Sd at the left are for the maximum shear stresses in unit of (95 GPa) in the BMG matrix and dendrites, respectively; (b) θ=15 ºrotation angles. The color bars marked as Sm and Sd at the right are the maximum shear stresses in the BMG matrix and dendrites, respectively.

Figures 4.4 (a)-(b) show τ around the dendrite with the rotation angles θ=0 ºand θ=15 º, respectively. It can be seen in Figure 4.4 (b) that the un-symmetric shear stress at the tip of incident shear band causes the detour of shear band upon touching the secondary arm of dendrite with a rotation angle θ=15 º. In the contrary the shear stresses are symmetric around the tip of shear band touching the primary arm of dendrite with a rotation angle θ=0 º, resulting in the branching of the incident shear band as shown in Figure 4.4 (a). The effect of fracture energy of dendrite on the

improved ductility is analyzed by showing τ around the dendrite in Figure 4.5. If the dendrite has large fracture energy (e_c=145.2 J/m^2) as shown in Figure 4.5 (b), in the BMG matrix there are large shear stresses only at the front of shear band which drives the shear band to move around the dendrite. If the dendrite has relative low fracture energy (e_c=48.4 J/m^2) as shown in Figure 4.5 (a), several places (marked as the black dashed box) in the BMG matrix could show large shear stresses which could initiate new shear bands. Such shear band multiplication occurs at some places close to the BMG-dendrite interface, and could relate with the fracture surfaces generated in the dendrite after the interaction between dendrite and shear bands, as reflected by the large shear stresses in dendrite shown in Figure 4.5 (a).

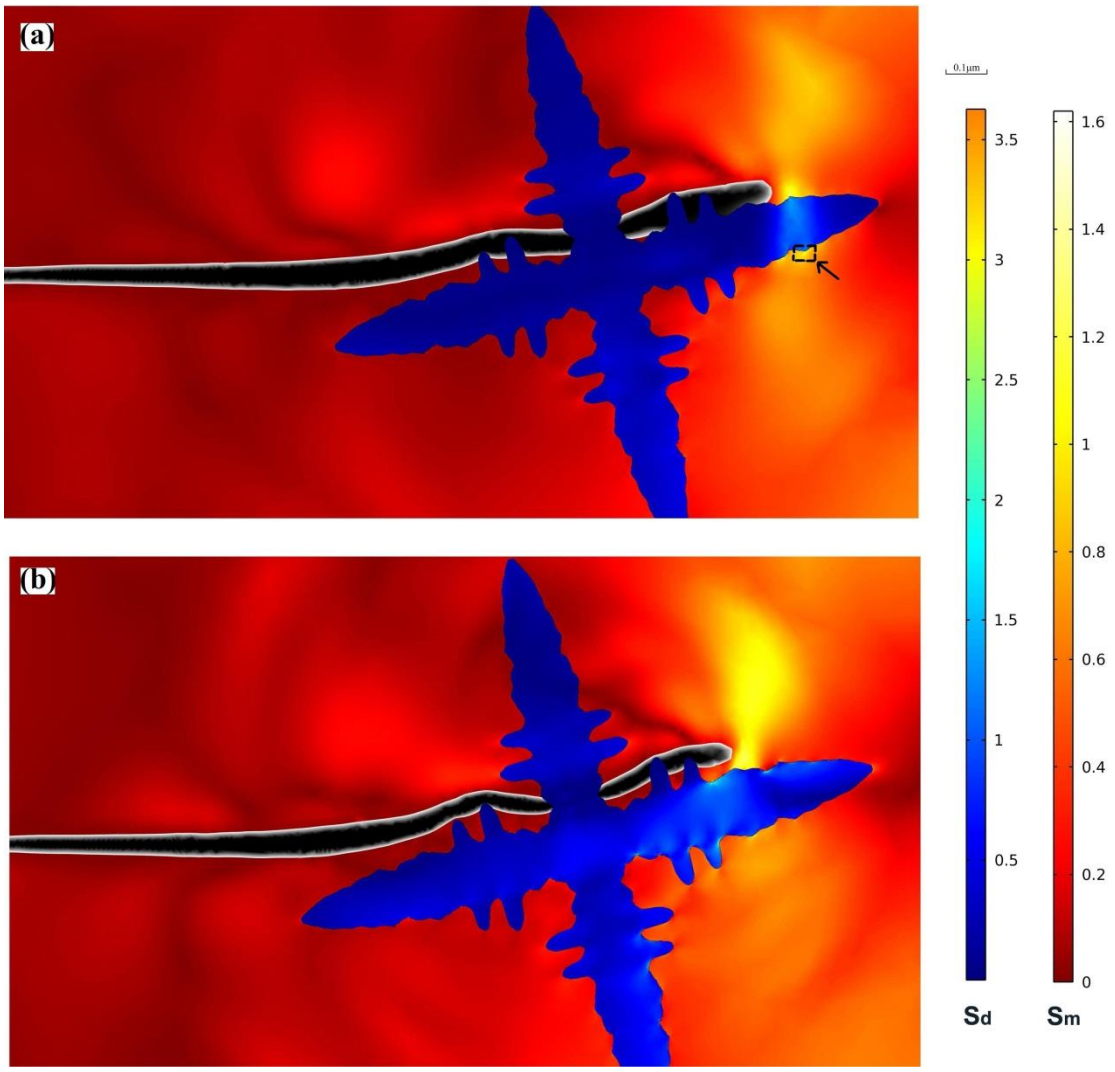

Figure 4. 5 Surface plots of shear stress fields in BMG composite containing dendrites at θ=15 °rotation angles and with (a) fracture energy e_c=48.4 J/m^2 and (b) fracture energy e_c=145.2 J/m^2. The color bars marked as Sm and Sd are for the maximum shear stresses in the BMG matrix and dendrites, respectively. The fracture surfaces in the dendrite are not shown.

4.4 Conclusions

In this work shear banding in the BMG composite is simulated based on the phase-field models. A dendrite phase is first formed by using the phase-field model and then deformation behaviors in the crystalline dendrite phase and BMG matrix

are simulated. Some important features are revealed from the simulation in microscopic scales. Two factors of the dendrites, i.e., the rotation angle representing the dispersion pattern and the fracture energy of the crystalline phase, are discussed.

From the simulation, the bifurcation and detour of the shear bands, which could result in the improved ductility of the composites, are observed when the crystalline dendrite phase is added. From the comparisons of the rotation angles, it is noted that the tips of the dendrite play a major role in the bifurcation and detour of the shear bands. It is found that the dendrite with high fracture energy can provide high crack resistance and then cause more obvious bifurcation and detour of the shear bands. The mechanisms of the bifurcation and detour of the shear bands can be well explained from the studies on the shear stress field.

These features are useful to explain the mechanisms of the improved ductility in the BMG composite and also helpful to guide the design of the composites. Furthermore, the phase-field model on shear banding is successfully applied to investigate the BMG composites containing dendrite phases with complicated microstructures. The numerical model can be employed to explore the even more complicate effects of

the microstructure of dendrites on shear banding in the BMG matrix.

Chapter 5 Phase-field modeling on deformation behaviors of micro- and nano-scale metallic glasses

Although the mechanical strength and the deformation behaviors change significantly when the sizes of metallic glasses decrease, it is very challenging to investigate the deformation mechanisms in micro- and nano-scale metallic glasses using the atomic simulation or the experimental methods. Whether there exist improved ductility and mechanical strength when the size of the metallic glasses decreases still remains unresolved. In this work, we will develop the phase-field model to bridge this gap and investigate the sample size effect on the deformation behaviors of metallic glasses.

5.1 Introduction

In the past several years, there have been a lot of investigations on the mechanisms of sample size effects on the deformation modes of metallic glasses (MGs). Several possible factors affecting the mechanical properties of the micro- and nano- scale MGs were investigated, such as the energy balance between the interface energy and the strain energy, or size effects on the plastic zone [Guo et al. 2007; Jang and Greer

2010] and stress state [Ma et al. 2012], surface constraint effects or surface unevenness effects [Guo et al. 2007; Li and Li 2005; Li and Li 2007; Luo et al. 2010; Wu et al. 2010b], and the effects of surface atoms on the shear transformation zones [Delogu 2009]. However, there were some inconsistent and controversial results noted in theoretical and experimental reports. For the nano-scale samples, some researchers reported that the yield strength was size-independent [Wu F.F. et al. 2009; Dubach et al. 2009; Chen et al. 2010]. Nevertheless, Jang and Greer indicated that the yield strength was size-dependent above 500 nm and size-independent below 500 nm [Jang and Greer 2010], and Lai et al. stated that the yield strength should increase with the decreasing size [Lai et al. 2008]. It was also found that the critical size at which the localized deformation transformed to the homogeneous deformation was significantly divergent. The critical size was reported to change from 40 nm to 400 nm [Guo et al. 2007; Ma et al. 2012; Chen et al. 2010; Volkert et al. 2008]. In the contrary, it was found that the localized shear deformation was less important and global plasticity could be significant when the size decreased to 250 nm [Schuster et al. 2008] or 150 nm [Wu X.L. et al. 2009]. These divergences can be partially understood as the results of the different sample conditions, such as the imperfect sample geometry or the various initial structural states in the MGs. During

the preparation of metallic glass samples, the fractions of free volumes in sample interior are diverse for the as-cast and annealed samples, and the experiments showed that the strength of the sample with less free volumes was higher than that of the samples with more defects [Wu W.F. et al. 2008]. On the other hand, many groups used focus ion-beam (FIB) technique to prepare nano-scale samples [Langford 2006]. Nevertheless, different initial status on the surface of the sample produced by FIB is also unavoidable [Kato 2004]. Thus it is important to investigate how the initial status of the samples, which are difficult to be detected in experiments, affect the deformation mode and the fracture strength, which favors the understanding of the mechanism of the size effect on the mechanical properties of metallic glass systems.

In this study, we conduct the simulations on three-dimensional (3D) nanowire samples with diameter ranging from 30 nm to 400 nm in tensile conditions based upon the phase-field model. The phase-field model in metallic glasses was first developed by Zheng and Li [Zheng and Li 2009] and was successfully applied to model the shear banding in bulk metallic glasses (BMGs) in two-dimensional (2D) simulations. This model can be easily extended to the 3D simulation. The method

and the parameters in the model would be revisited in Section 5.2. The efficiency of this phenomenological theory in studying the fracture in 3D metallic glass systems is elucidated in Section 5.3.1. In Section 5.3.2, two factors of the MG nanowires, i.e., the fractions of initial deformation defects on their surfaces and in the nanowire interior, are considered to investigate their effects on the fracture strength of the specimens. From the simulations, the deformation mode, the fracture strength and the relationship between the fracture strength and the sample size are identified, and the underlying mechanisms are discussed.

5.2 Simulation details

According to the dynamic model [Zheng and Li 2009] as stated in details in Section 2.3, the shear band propagation and the evolution of shear banding in BMG without considering the local heating could be simulated by solving Eqs. 2.22(a) and 2.22(b). Here we solve those equations in fully 3D samples. The samples are chosen as the cylinder with the fixed height of 800 nm as shown in Figure 5.1. The different sample sizes are characterized by the diameter of the cylinder, which ranges from 30 nm to 400 nm. Hence the MG samples could be considered as nanowires. The Vitrelloy 1 ($Zr_{41}Ti_{14}Ni_{10}Cu_{12.5}Be_{22.5}$) is chosen as the material in the present simulations. The

material properties are listed as follows [Bruck et al. 1994; Conner et al. 1997]: Glass Transition Temperature T_g=625 K; Young's modulus E=95 GPa; Poisson's ratio ν=0.35; Mass density ρ_0=6050 kg/m^3. The elastic strain limit under uniaxial tension is ε_f~2%. The characteristic time for deformation defect activation is τ_ρ=0.25 ns [Khonik et al. 2008]. The coefficients in Eq. (2.20) are given by $a_0=4\Delta G(2-T/T_g)$, b_0=-24ΔG, c_0=16ΔG, where the deformation defect activation energy ΔG is estimated as 4.6 eV at room temperature [Lu et al. 2003]. The coefficients a_1=-6 and b_1=6 are chosen to quantitatively present the phase transformation of deformation defects in glassy alloy under plastic deformation. According to the chosen coefficients, the shear modulus tends to zero when $\rho(\boldsymbol{r})\rightarrow 1.0$, which can show the shear softening and fracture in the glassy alloy. Then the critical density of deformation defect is defined as 0.8 to distinguish the shear softening regions from the remaining elastic region of ideal randomly packed solid structures.

The length rescale factor $l_r = \sqrt{\kappa/\mu e_0}$ and time rescale factor $t_0 = l_r/\sqrt{\mu/\rho_0}$ featuring as the length and time scales of the system are applied to Eqs. 2.22(a) and 2.22(b) to rescale them into dimensionless forms. The dimensionless equations can be solved numerically. Tetrahedrons are used to discrete space domain and the

backward differentiation formula (BDF) scheme is employed to discrete and integrate time in the numerical analysis. The uniaxial tension is applied on the top surface. The displacement constraint in Z-direction is imposed on the bottom surface, and the other surfaces are kept free as shown in Figure 5.1. Before calculation, the initial defects (defined as the points with $\rho(\boldsymbol{r})=1.0$) are randomly distributed in interior and on sample surfaces except the top and bottom surfaces. The remaining nanowire regions are defined as the ideal glassy status with $\rho(\boldsymbol{r})=0$.

5.3 Simulated results

It is necessary to validate the phase-field modeling on shear banding in 3D BMG model since in the previous studies the model was applied to simulate the deformation in 2D samples only. Thus we present the simulated results as follows. We shall firstly prove the validation of the phase-field model in the simulation of the 3D MG samples in section 5.3.1. Then the effects of initial defects on nanowire surfaces and in the nanowire interior on the fracture toughness and ductility are analyzed in section 5.3.2. Finally the relation between the fracture strength and the sample sizes, and the deformation modes in nanowires with various diameters are discussed.

5.3.1 Validation of phase-field modeling on the simulation of deformation in 3D MGs

As mentioned above, 3D simulation on MGs based on the phase-field theory has never been reported in literatures. Therefore, we shall first conduct a simple 3D case study for the analysis of structure fracture and shear band propagation in the metallic glasses to verify the effectiveness of the phase-field model in the simulation of mechanical deformation. The sample is in cylinder shape with a diameter of 0.4 μm and a height of 0.8 μm as shown in Figure 5.1. In order to simulate the metallic glass sample with isotropic deformation defects, 6.8% volume fraction of the cylinder interior are randomly chosen before loading to have large density of deformation defects, i.e., $\rho(\boldsymbol{r})=1.0$, which simulates the MG nanowire with 6.8% deformation defects in its interior. The surface of the nanowire is assumed to be perfect.

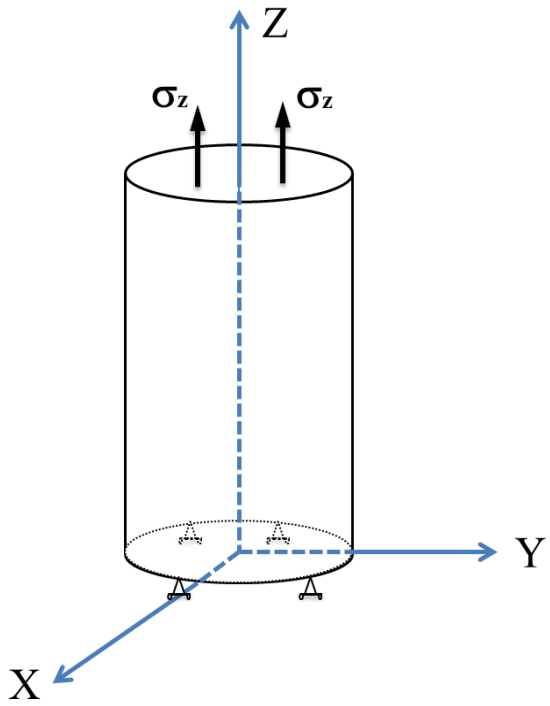

Figure 5. 1 The model system of a MG nanowire. Tensile stress is applied along Z direction.

During simulation, it is found that the MG nanowire sample with a diameter of 400 nm fractures in localized shear banding mode. Figure 5.2 and Figure 5.3 show the equivalent plastic strain in the XZ plane and in the nanowire interior, respectively, at different time. In Figure 5.2 (a), the uniform elastic deformation is found and no plastic strain can be observed at t=4.0 ns, which is consistent with that in Figure 5.3 (a). In Figure 5.2 (b), one localized shear zone with large plastic strain appears at t=10 ns. The area with non-zero plastic strain is larger at t=12.5 ns than that at t=10 ns, as shown in Figure 5.2 (c). One shear band is formed as shown in Figure 5.2 (d) at t=13 ns, which is denoted as S2 in Figure 5.3 and is in yellow color. There are

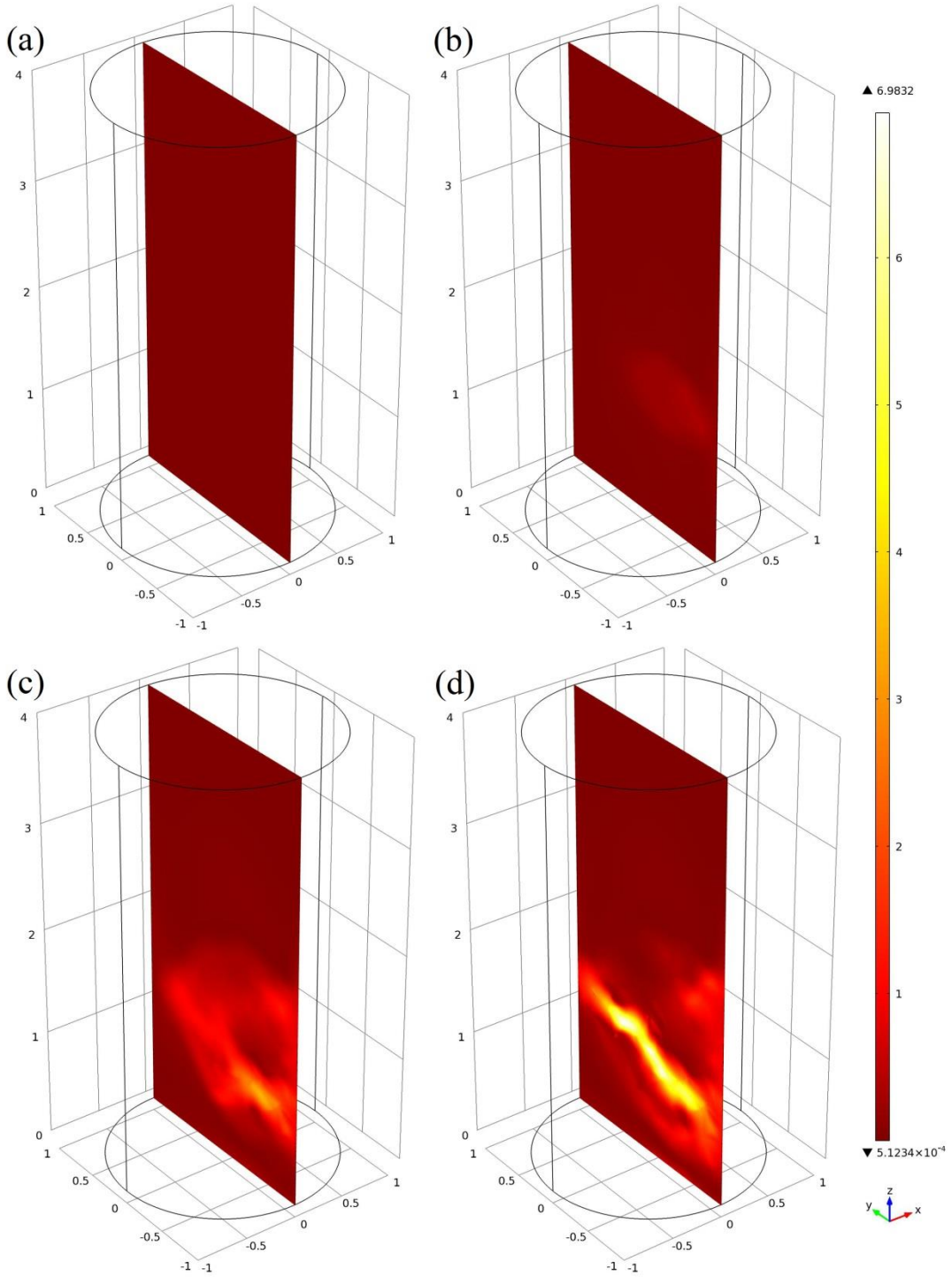

Figure 5. 2 The equivalent plastic strain in the middle cross sectional plane in the nanowire (d=400 nm) at different time. (a) t=4 ns, (b) t=10 ns, (c) t=12.5 ns, (d) t=13 ns. The color bar represents the value of the equivalent plastic strain. The shape of the nanowire before deformation is depicted by the thin solid curves.

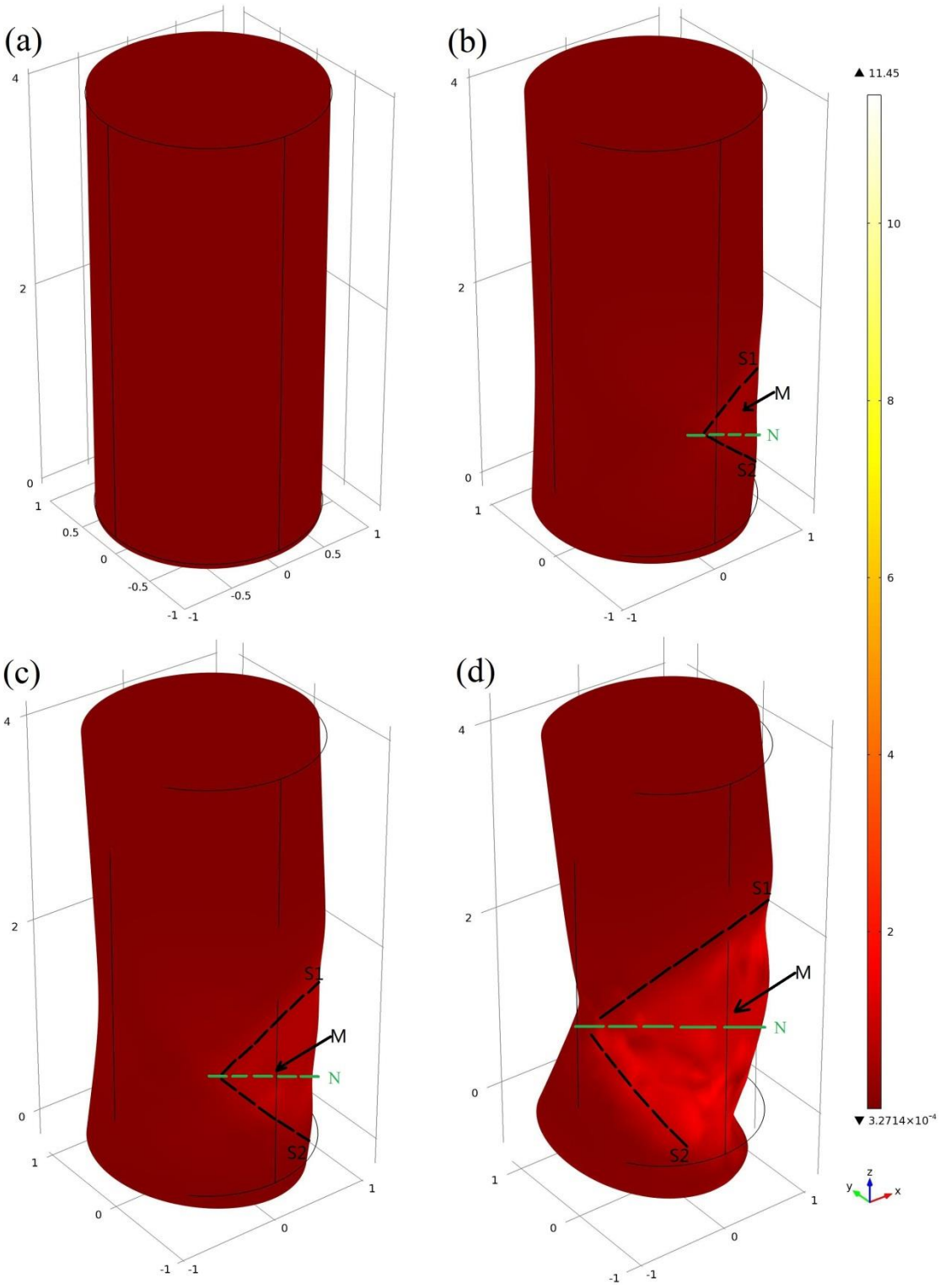

Figure 5. 3 The equivalent plastic strain in the sample (d=400 nm) interior at different time. (a) *t*=4 ns, (b) *t*=10 ns, (c) *t*=12.5 ns, (d) *t*=13 ns. The color bar represents the value of the equivalent plastic strain.

some serration flows in the cracking surface, and we also find that the crack is initiated from the defects in the nanowire interior.

In Figure 5.3, two surfaces are marked as S1 and S2 by dashed lines to identify the regions with significant plastic strains. It seems that these two surfaces rotate about +40° or -40° from the cracking plane denoted as N. From the results shown in Figure 5.2, we can see that the plastic strain around surface S2 is much larger than those in other regions, suggesting that S2 is the shear band dominating the fracture process in the zone marked as M in Figure 5.3. The fracture should be generated from the shear plane associated with the shear band.

This characteristics of fracture, especially that the fracture surface is about 50° with the loading axis, is consistent with the experimental results [Wu F.F. et al. 2009; Jang and Greer 2010]. Thus it is suggested that the phase-field model can effectively describe the dynamic fracture of the MG systems.

5.3.2 Effects of initial deformation defects on the mechanical strength

Surface imperfection is one of the important factors that affect the mechanical properties of the bulk metallic glasses [Li and Li 2005; Guo et al. 2007; Gilbert et al. 1999; Lowhaphandu and Lewandoski 1998]. The imperfections are unavoidable in metallic glasses during the sample preparation. It was reported in literature that through proper treatment on the surfaces to reduce the initial deformation defects, the mechanical properties could be improved [Wu et al. 2010b]. When the MG samples are in small scale, e.g., nano-scale, the effects of deformation defects are much complicated than those in macroscopic scale. Although there was report on the effect of notch on the mechanical strength of MG nanowire [Li and Li 2005], few systematic studies have focused on the effects of initial deformation defects of the nanowire samples on their mechanical properties.

In this section, the effects of initial deformation defects on MG nanowire surface and in the nanowire interior on the mechanical strength shall be studied. The fracture strength is obtained for the MG nanowire with diameters 400 nm and 40 nm and with various fractions of initial defects on its surface and in interior. In order to

discuss the effect of initial defects on nanowire surface, the fraction of initial defects in nanowire interior is kept as a constant. Similarly, to study the influence of the initial deformation defect in the nanowire interior, we will maintain the fractions of initial deformation defects on nanowire surfaces unchanged.

5.3.2.1 The effect of initial deformation defects on nanowire surface on mechanical strength

It was found in several experiments and simulation investigations that the effect of the surface would increase with the decreasing sample size [Li and Li 2005; Li and Li 2006; Li and Li 2007]. It was reported in MD simulations on MG nanowires that whether the shear transformation zones involving the surface atoms or not could significantly affect the deformation modes [Luo et al. 2010]. The experimental results indicated that when the sample diameter decreased below 100 nm the nanowire samples with some unevenness failed through necking while the homogeneous failure was observed in the nanowire samples without defects on their surface [Guo et al. 2007]. Here we shall employ phase-field model to investigate how the initial deformation defects on surface affect the fracture strength of Zr-based MG nanowires.

In the simulations, the nanowire sample with a diameter of 400 nm is the same as that described in Section 5.3.1. For the MG nanowire with a diameter of 40 nm, the height is also kept as 800 nm. We first investigate the influence of the initial deformation defects on nanowire surface by considering the fraction of initial deformation defects in nanowire interior to be fixed as 9.8%. Using the phase-field modeling, we can obtain the relationship between the fracture strength and the fraction of deformation defects on nanowire surfaces.

The quantitative relationships between the normalized fracture strength with respect to the Young's modulus and the fraction of the initial defects on nanowire surface are shown in Figure 5.4. The fraction of defects on the nanowire surface ranges from 0 to 22% for the nanowire with a diameter of 400 nm, while the corresponding fraction changes from 15% to 38.6% for the nanowire with a diameter of 40 nm.

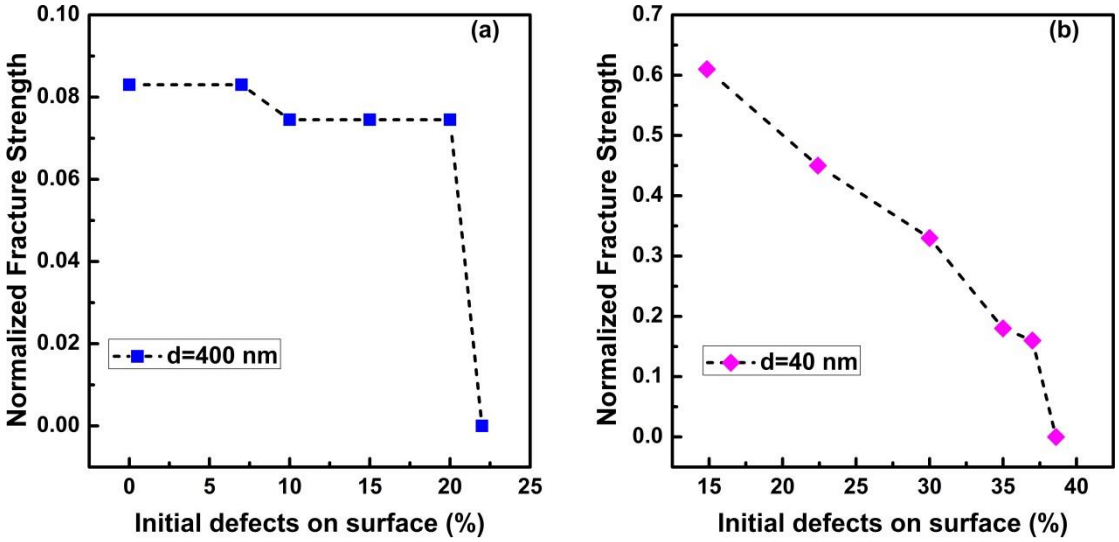

Figure 5. 4 The relationship between the normalized fracture strength and the fraction of initial defects on nanowire surfaces. The nanowire diameter is (a) d=400 nm; (b) d=40 nm.

From Figure 5.4 (a) which shows the normalized fracture strength *vs* fraction of initial defects on nanowire surface of the sample with a diameter d=400 nm, we can see that there is nearly no change in normalized fracture strength when the fraction of the deformation defects on nanowire surface changes from 0 to 20%. The value is estimated as E/15, where E represents the Young's modulus. Then the strength decreases rapidly to zero when the fraction of the deformation defects on nanowire surface increases to 22%. For the MG nanowire with d=40 nm, the fracture strength changes gradually with the decreasing fraction of deformation defects on nanowire surface, as shown in Figure 5.4 (b). When the fraction of initial deformation defects on nanowire surface increases to about 38.6%, the fracture strength decreases to zero.

In nanowire with d=40 nm, the fracture strength decreases significantly (more than 75%) when the fraction of initial deformation defects on the nanowire surface changes from about 15.0% to 37%.

In Figure 5.4, we can see that the fracture strength decreases with the increasing fractions of deformation defects on nanowire surface. It is because the larger fraction of initial deformation defects on the surface leads to higher possibility of activated deformation defects which could induce the local crack or fracture on nanowire surface. Thus the fracture strength could decrease. The correlation between the fracture strength and the surface imperfection is consistent with the experimental results [Wu et al. 2010b].

It is noted that the fracture strength is more sensitive to the initial deformation defects on the nanowire surfaces in the sample with smaller diameter which has a larger surface-to-volume ratio. The volume of the nanowire is proportional to the square of the diameter d^2, while the side surface area of the nanowire is a function of the diameter d. With the decreasing diameter, the sample volume decreases much significantly than the surface area and thus the surface portion of deformation

defects significantly increases. In nanowire with d=400 nm, the number of initial deformation defects on surface is small compared with that in the nanowire interior. Thus the effect of initial defects on surface can be neglected. While for the nanowire with d=40 nm, the amount of deformation defects on the surface cannot be neglected, and their roles as weak points during deformation should be considered. Such argument has been proved in simulations that the deformation defects on surface are easy to be activated when the diameter is in several nanometer scales [Delogu 2009], especially when the fraction of initial deformation defects on surface is several times higher than that in the nanowire interior. Such enhanced surface effects on mechanical deformation are similar with those observed in crystalline solid when the sample size is decreased to the order of 10 nm [Sieradzki et al. 2006].

From the simulated results it is noted that the surface effect is much significant in nanowire with d=40 nm. Keeping the fractions of deformation defects on nanowire surface to be 15% and those in the nanowire interior to be 9.8% for samples with diameters of 400 nm and 40 nm, we can observe that the strength of nanowire with d=40 nm is much higher than that of nanowire with d=400 nm. Such simulated results of size effect in metallic glass systems are consistent with experiments [Ma et

al. 2012].

5.3.2.2 The effect of initial deformation defects in nanowire interior on mechanical strength

As mentioned above, the fraction of deformation defects (such as free volumes) is not a constant for the nanowire samples prepared by different methods. Even if the samples are prepared by the same method, the fractions of deformation defects can still be different for the samples with different sizes [Wu W.F. et al. 2008]. It has also been revealed that the samples with less deformation defects have higher strength than those with more deformation defects. However, it is difficult to detect the fraction of initial deformation defects in nanowire interior and to conduct the tensile experiments when the sample size decreases to tens of nanometers. Thus little attention has been paid to the effect of initial deformation defects of metallic glasses on their deformation behaviors. In this section, how the initial deformation defects in nanowire interior affects the fracture strength of metallic glass system will be studied. The effect of initial deformation defects in nanowire interiors on their deformation behaviors in the nanowires with diameters of 400 nm and 40 nm will be compared. In the simulation, the fraction of initial deformation defects on nanowire surface is fixed as 15.0% and the fraction of initial deformation defects in nanowire

interior changes from 6.8% to 10.9% in nanowire with d=400 nm. For the nanowire with d=40 nm, the fraction of defects on surface is assumed to be unchanged (15.0%) and the fraction in nanowire interior changes from about 10% to 70%.

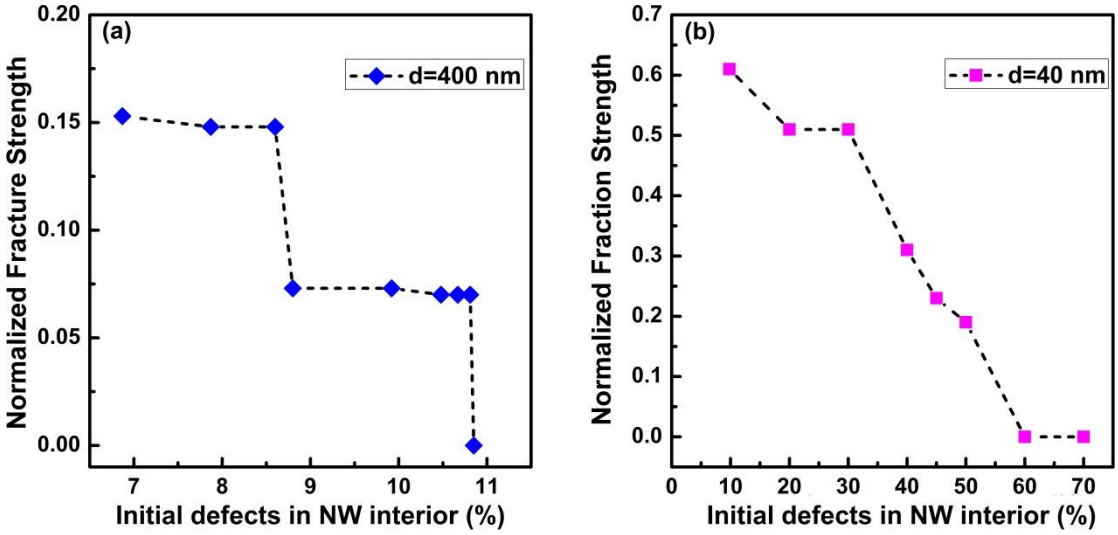

Figure 5. 5 The relationship between the normalized fracture strength with respect to the Young's modulus E and the fraction of initial deformation defects in nanowire (NW) interior. (a) The diameter of the sample is 400 nm; (b) The diameter of the sample is 40 nm.

As shown in Figure 5.5, it is found that the fracture strength is significantly affected by the fraction of initial deformation defects in nanowire interior for the two samples with d=400 nm and 40 nm. In some atomic force microscopy experiments, it is proposed that the structure of the MGs is composed of the ideal regions (densely-packed atomic clusters) and defective locations (loosely packed atomic clusters defined as deformation defects in the phase-field model) [Liu et al. 2011]. Thus it is suggested that the initial deformation defects such as the excess free

volumes could facilitate the formation and propagation of shear bands, resulting in easy and quick fracture. By increasing the fraction of initial deformation defects in the nanowire interior, under external loading, it is highly possible that one location containing higher fraction of initial deformation defects is subjected to higher strains, resulting in the early yield. The lower yield strength in the region with more deformation defects has been verified through measuring the nanohardness of the deformed regions, in comparison with that of the undeformed locations [Yoo et al. 2009].

As shown in Figure 5.5, the critical density of deformation defects in the nanowire interior beyond which the nanowire sample is too soft to support any applied load is about 11% for the sample with d=400 nm and about 60% for the sample with d=40 nm, respectively. Furthermore we can observe that the fracture strengths of the nanowire samples with d=40 nm is much higher than that of the nanowire with d=400 nm when their densities of initial deformation defects in the nanowire interior are the same, indicating that the size effect on the mechanical strength in these nano-scale MG samples is significant.

5.3.3 Size effects on the fracture strength of MG nanowires

In the previous sections, it is shown that the phase-field modeling on the shear banding in MG can effectively describe the dynamic deformation behaviors in 3D nano-scale metallic glass. In this section, we will use the phase-field model to investigate the size effect on the fracture strength and the deformation modes of MG nanowires. With the decreasing diameter, the surface effects could be more significant and dominant in the process of mechanical deformation. Thus the role of surface effects on the size-dependent mechanical deformation will mainly considered in this section.

In the preparation of MG nanowires, for example, using FIB processing, the nanowire surfaces are usually in inhomogeneous status and even crystallization occurs on the nanowire surface [Huang et al. 2005]. Thus, the fraction of initial deformation defect on the nanowire surfaces could diverge significantly in samples prepared by different methods and under different processing conditions. However, it is almost impossible to determine the authentic quantity of the fraction of the deformation defects on the nanowire surfaces of the MG samples. In order to investigate how the initial deformation defects affect the fracture strength among

samples with different diameters, two assumptions concerning the relationship between the initial deformation defects on the nanowire surfaces and the sample diameters are employed. In the first assumption, the fractions of the initial deformation defects on the nanowire surface are assumed to be in an inversed square root function with the diameters. In the second assumption, fractions of initial deformation defects on the nanowire surfaces are kept as a constant for the samples with different diameters. The second assumption as an approximation is reasonable as in some experiments one tries to reduce the discrepancy on samples' initial status by some treatments such as using the low-energy FIB technique, which is suggested to cause less changes of the initial status of the nanowires with different diameters.

In the present simulation, the initial deformation defects in the nanowire interior is assumed to be 9.8% while the fraction of initial deformation defects on the nanowire surface varies. In nanowire with the diameter d=400 nm, 20% initial deformation defects have been assigned randomly on the surface. For the samples with other diameters, the initial deformation defects on the surface can be determined according to the two assumptions mentioned above.

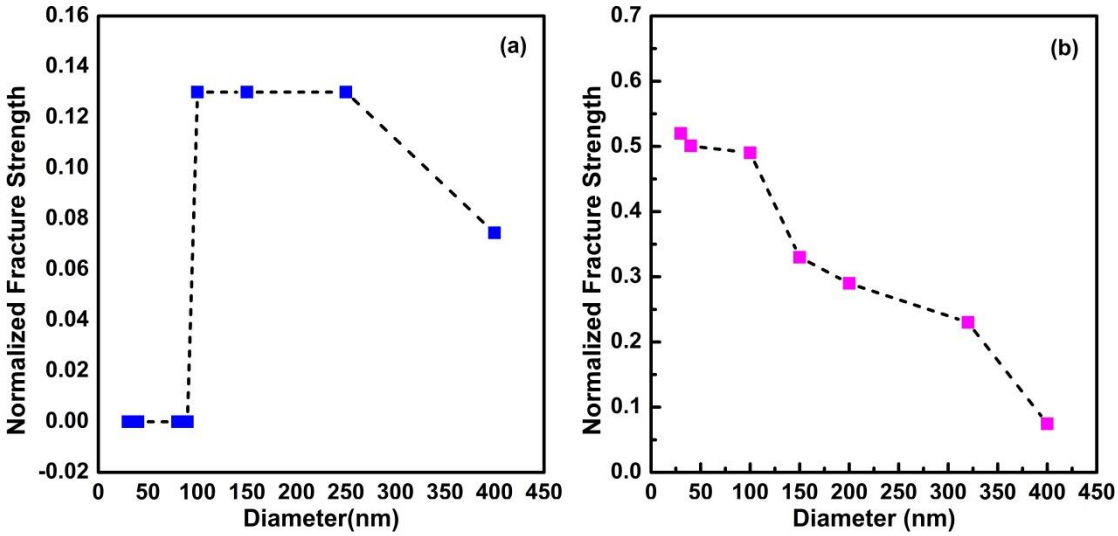

Figure 5. 6 The relationship between the normalized fracture strength and the nanowire diameters. (a) The fraction of initial deformation defects on the nanowire surface is 20% for nanowire with d=400 nm. For nanowires with d<400 nm, the defects density is assumed to be inversed proportional to $d^{1/2}$. (b) The fraction of initial deformation defects on the nanowire surface is 20% for nanowires with various diameters.

The relation between the normalized fracture strength and sample diameter are shown in Figure 5.6. Figures 5.6 (a) and (b) correspond to the first and second assumptions on the initial deformation defects on the nanowire surfaces, respectively. In Figure 5.6 (a), we can see that when the diameter decreases from 400 nm to 250 nm, the fracture strength increases significantly. The fracture strength seems size-independent when the diameter changes from 250 nm to 100 nm. Surprisedly, it is found that the fracture strength drops to zero when the sample diameter reduces to 40 nm. In the nanowire with d=40 nm, the fraction of deformation defects on the surface is as high as 63.25% which is easy to be activated and the sample is unable to withstand any external loading. The maximum fracture strength is achieved and

kept constant when the diameter ranges from 100 nm to 250 nm. In Figure 5.6 (b), we can see the fracture strength increases dramatically when the diameter decreases from 400 nm to 150 nm. No much increases on their fracture strength when their diameter changes from 150 nm to 30 nm. It is noted that the sample with diameter 30 nm has high fracture strength, which is completely different from that of nanowire with the same diameter and large initial deformation defects on surface.

From the simulation, we can find that the size effects on the fracture strengths of nanowires are obviously different if the status of the initial deformation defects on nanowire surfaces is diverse, which may provide explanation for the discrepancies in the previous experiments data describing the size effects on the mechanical strength of MG nanowires.

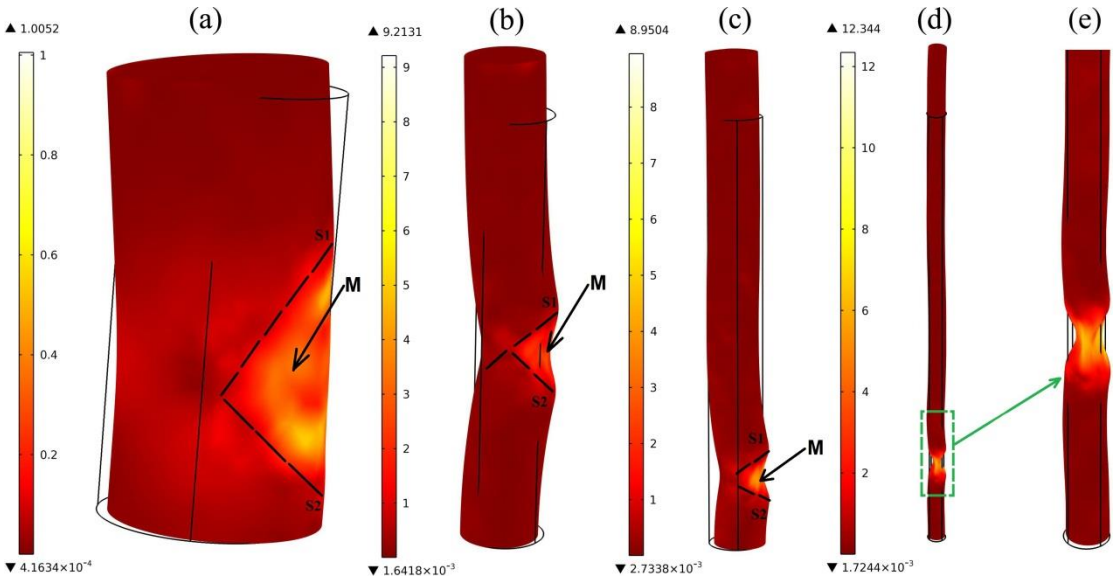

Figure 5. 7 The deformation in nanowires with different diameters d just before fracture. (a) d=400 nm; (b) d=150 nm; (c) d=100 nm; (d) d=30 nm and (e) zoom-in view of the marked region shown in (d). The color bars represent the value of the plastic strain in nanowire. S1 and S2 represent the two shear bands and the black dashed lines correspond to the shear band locations. M marks the cracking region between two shear bands. The fraction of initial deformation defects on the nanowire surface is 20% and the fraction of initial defects in interior is kept as 9.8% for nanowires with various diameters.

Now we assume in the nanowires under tension, the initial deformation defects on the surface and in the nanowire interior are independent of diameter. The tensile deformation behaviors in the nanowires with diameters d=400, 150, 100 and 30 nm just before the fracture occurs are shown in Figure 5.7. It can be seen that the deformation modes vary significantly with the change of sample size. For the nanowire with d=400 nm as shown in Figure 5.7 (a), it can be found that the fracture is caused by two progressive shear bands. The region between these two shear bands withstands high plastic strains. It can also be observed that the plastic strain in the region between these two shear bands is not uniform, suggesting that the

deformation in this sample is localized. Figures 5.7 (b) and (c) represent the deformation in nanowires with 150 nm and 100 nm in diameters, respectively. Different from that shown in Figure 5.7 (a), the plastic strains in the region between those two shear bands are more uniform. It is noted that in the nanowire with d=100 nm there are some new features of deformation behaviors. We can see that the two shear bands tend to spread individually during their evolutions and will not meet inside the nanowire if they can further propagate, resulting in the small elongation of the nanowire with d=100 nm in comparison with those of nanowires with d=200 nm and d=150 nm. When the nanowire diameter decreases to 30 nm, some interesting phenomena can be observed. As shown in Figure 5.7 (e), which is the zoom-in view of the deformed region shown in Figure 5.7 (d), necking of the nanowire under plastic deformation can be seen.

5.4 Discussions

From the simulated results, it can be observed that the initial status of the deformation defects on the nanowire surface is the most significant factor that influences the fracture strength. The phase-field modeling is very helpful in the quantitative description of such surface effects on the mechanical properties of

nanowires, which is difficult to be handled by experiments. In the following sections, some possible factors causing the discrepancies among the previous experiments shall be discussed. We will quantitatively describe the fracture strength as a function of the nanowire diameter, which is helpful in unveiling the deformation mechanisms in nanowires with different diameters.

5.4.1 The possible factors affecting experimental results

Different from those of BMGs, MG nanowires exhibit tensile ductility and mechanical strength reaching the theoretical ideal strength of amorphous solid as observed in experiments [Guo et al. 2007; Jang and Greer 2010; Wu et al. 2010a]. Due to the complexity and the limitation of current experimental techniques, the factors affecting such novel mechanical properties of MG cannot be quantitatively reflected through experiments. In the previous sections, two possible factors, the initial deformation defects on the nanowire surface and those in the nanowire interior which could affect the mechanical properties of the MG nanowires, have been chosen to supplement the experiments. The effects of these two factors on the mechanical properties of MG nanowires are quantitatively investigated and they could be meaningful in both fundamental research and engineering applications.

Some surface treatment technologies have been introduced in the preparation of MG nanowires, e.g., drawing surface handling was conducted on the MG samples [Wu et al. 2010b]. In the experiments, it was found that the surface handling could reduce the flaws in MG sample (including the reductions of micro-cracks, the flow defects and the interstitial holes), and the residual stresses on the MG surface. All of these changes can improve the tensile fracture strength of the MG nanowires. The simulation in this work provides valuable supplemental information for the experiments data from the view of numerical analysis. The simulated results show that the size effects on fracture strength result mostly from the initial deformation defects on the nanowire surface.

5.4.2 The relationship between the normalized fracture strength and the nanowire diameter

The stress required to drive the shear band to propagate increases as the sample size decreases [Jang and Greer 2010]. It was also indicated that the shear banding in nano-scale metallic glass was not completely suppressed but required higher load to initiate. This may be the main reason for the observation in our simulation that the fracture strength increases as the nanowire diameter decreases from 400 nm to 100

nm when shear banding is the typical deformation mode. On the other hand, some new deformation mode may occur in the nanowires with diameters smaller than 100 nm when the shear banding is not the dominant deformation mechanism. It is well known that the strength increases directly from the extra radial compressive stress which is estimated as γ/d (γ is the surface energy of the material) from the nanowire surface [Luo et al. 2010] when the diameter d is decreased to 100 nm or below. A certain amount of applied tensile stresses is used to counteract these extra stresses due to the surface stresses. The suppression on cracking due to the existence of these compressive stresses also leads to the increasing fracture strength [Zhang et al. 2003; Shan et al. 2008; Hofman et al. 2008a].

From the simulations and other experimental reports, it is found that with the size decreasing, the size effects are more obvious. The feature called "smaller is stronger". In Figure 5.8, we fit the fracture strength of nanowire with d>100 nm with respect to *d* using a Hall-Petch-like relation

$$\sigma_N(d) = \sigma_N^0 + kd^{-\alpha}, \tag{5.1}$$

where σ_N^0, k and α are d-independent constants and α is an exponent.

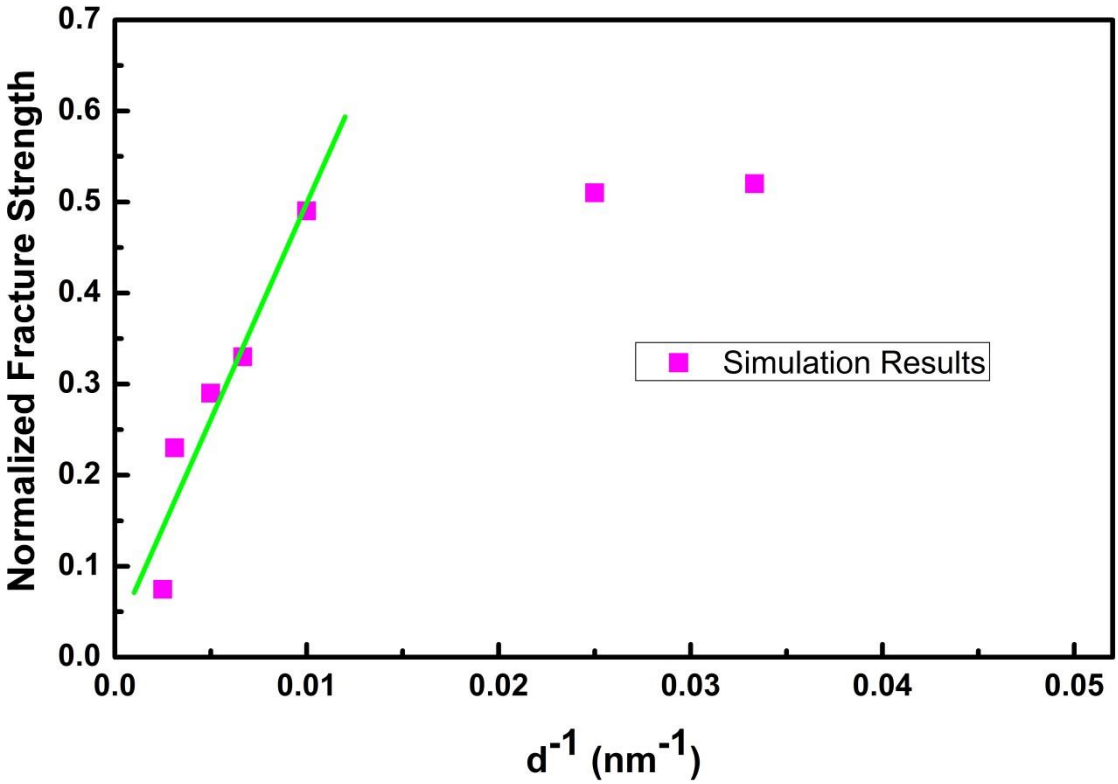

Figure 5. 8 The fitting of normalized fracture strength with respect to d^{-1}. The squares in purple represent simulated results in nanowires with the diameter ranging from 400 nm to 30 nm. The green line represents the fitting using Eq. (5.2).

In Figure 5.8, we can see that the normalized fracture strength can be fitted as the function of the reciprocal of the nanowire diameter, and the expression can be written as,

$$\frac{\sigma_N}{E} = 0.0235 + 47.521 d^{-1} \quad , \tag{5.2}$$

where the diameter d ranges from 100 nm to 400 nm. The d-independent normalized fracture strength σ_N^0 is estimated as 0.0235E, which is about 2.2 GPa if the Young's modulus is 95 GPa for the Zr-based BMG. It is also noted that the trend of change of σ_N deviates from Eq. (5.2) when the diameter decreases below 100 nm (such as

d=40 nm and 30 nm in the simulation). Compared with the Hall-Petch relation for yield stress of the polycrystalline solids [Hall 1951], the simulated results show that the mechanical strength as a function of nanowire diameter is similar in describing the size effects. When the diameter changes from 400 nm to 100 nm, the fracture strength just deviates from the Hall-Petch like relationship rather than follows an inverse Hall-Petch relationship, which is usually observed as grain size softening in nanocrystalline solids when their grain sizes is below 50 nm [Kim and Okazaki 1992].

5.4.3 Changes of deformation mode in nanowires with d<100 nm

From the simulated results, we can see that the shear-band deformation also occurs in the nanowires with diameters ranging from 400 nm to 100 nm, consistent with the results observed in experiments [Jang and Greer 2010]. The shear banding mechanism was not completely suppressed, and the fracture strength ranges from about E/15 at d=400 nm to nearly E/2 at d=100 nm. The size effects can be reflected as the localized plastic zone in nanowire with larger diameter (d=400 nm), and the more uniform plastic deformation between the shear bands due to the uncrossing

shear bands inside the nanowire with small diameter (d=100 nm). In particular it is found that the two uncrossing shear bands in the nanowire with d≤100 nm could improve the ductility and the fracture strength, compared with those of nanowire with d>100 nm.

When the diameter continues to decrease to 30 nm, the necking deformation occurs. This may be caused by the new mechanism, i.e., the surface effect, when the sample diameter is decreased to the order of 10 nm [Luo et al. 2010]. In the nanowire interior the stresses exerted by the nanowire surface are estimated as γ/d [Luo et al. 2010; Sieradzki et al. 2006]. Under tension conditions, certain amount of applied tensile stresses should be used to counterbalance the compressive stresses caused by the surface effect, preventing the initiation of shear bands. What is more important is that this extra compressive stress makes the strains in the nanowire interior tensile in longitudinal direction (Z) and compressive in the other two directions (X and Y), which hinders the cracking or the shear band propagation. With the increasing compressive stress due to the reduction on nanowire diameter, it is highly possible that the initiation and extension of the crack are hindered, resulting in the higher fracture strength of the nanowire. At the same time, the strains on the nanowire

surface will be tensile in hoop direction. Thus the deformation on the surface are tensile in two directions (Z and hoop) resulting in large strains in locations near the surface and the easy activation of surface deformation defects, as observed also from MD simulation [Delogu 2009]. The severe plastic strains from nanowire surface, combined with the complex stress status for some locations with initial deformation defects in the nanowire interior, lead to the necking deformation behaviors which dominate the fracture process in the nanowires with smaller diameters ($d<40$ nm).

The change in deformation modes is the striking feature observed in experiments when the sample size decreases to nano-scale. Especially, the large macroscopic plasticity due to the homogeneous deformation is the key discovery on the deformation of MG nanowires. For bulk metallic glass, the homogeneous deformation can only take place around the glass transition temperature [Schuh et al. 2007; Inoue 2000]. However, for the nano-scale MGs, it was found that the metallic glass in dimensions below 100 nm can fail in shear offset after large homogeneous deformation when the surface is free of notches [Guo et al. 2007]. Otherwise, it will fail as necking like that observed in experiment when the surface has notches [Guo et al. 2007]. Our simulated results provide deep insight into the process of

homogeneous plastic deformation in MG nanowires.

5.5 Conclusions

In this work, the phase-field model is extended to 3D simulation on the fracture behaviors in metallic glasses. The fracture process and the deformation mechanisms of MG nanowires with different diameters can be accounted. The size effect of the mechanical properties of metallic glass nanowires has been considered based on two factors, i.e., the fractions of initial defects in nanowire interior and on its surfaces. Some meaningful features are revealed from the simulations and are found to be consistent with the experimental results. With the decreasing diameter, it is found that the initial status of the nanowire surfaces play a dominant role on the fracture strength. If the fraction of initial deformation defects on nanowire surface follows a linear relationship with $d^{-1/2}$, the fracture strength shows a maximum at $d \cong 200$ nm and suddenly drops to zero due to so large fraction of initial deformation defects on the surface. If the fraction of initial deformation defects on the surface is in-dependent of nanowire diameter, the fracture strength increases significantly with the decreasing diameter ranging from 400 nm to 100 nm, and slightly increases when the diameter decreases from 100 nm to 30 nm. It is also found that the fracture

strength increases in a similar trend as the Hall-Petch relation when the diameter is larger than 100 nm. When the nanowire diameter is below 100 nm, the typical necking deformation is observed. These modeling results indicate that the discrepancies among the previous reports in literature could be caused by the different initial status of deformation defects in the samples. The simulated results provide quantitative understanding on the size effects on the mechanical properties of MG nanowires

Chapter 6 Conclusions and remarks

The phase-field model of shear banding in MGs is successfully applied to investigate the improved ductility in porous BMG, the BMG composites and the MG nanowires. Some valuable results such as the factors and the possible mechanisms affecting the improved ductility are derived through the phase-field simulation in this thesis, which could assist the experimental studies and also provide guidance for the design of MGs with good ductility.

Both porous BMGs and BMGs containing *in-situ* formed dendrite are found to show improved ductility. Porous BMG with closed pores are more effective in detouring the shear bands, and the lack of local heat conduction across the pores is helpful in inducing more shear bands from pore surface in porous BMGs containing closed or open pores. The BMGs composites containing dendrites with low fracture energy show improved ductility since more fracture areas (not only in BMG matrix but also in crystalline dendrites) could be generated, while the dendrites with higher fracture energy can effectively bifurcate the shear bands when their rotation angle is within 0° and 15°, which could avoid the brittle failure. These two types of BMG alloys are

potential in engineering application as their ductility could be improved by controlling the related factors elucidated in the simulation.

Compared with porous BMGs and BMG composites, the improved ductility is more effectively enhanced through decreasing the sample size. It is observed that the ductility can be improved through two interacting shear bands and the zone between them sustaining large plastic strain when the diameter is below 100 nm. It is found that the nanowire surface plays a main role in the size effect on the mechanical properties of MG nanowire since the surface could impede shear band initiation and extension. Thus the improved ductility is more obviously observed in the nano-scale MGs.

The mechanisms of improved ductility in MGs have been investigated through the phase-field modeling, which are important supplements to those obtained from experimental and theoretical results. However, only a few issues concerning the improved ductility of MGs are touched in my simulation work due to the limited PhD study period. Further studies are needed to explore those un-resolved issues concerning the deformation mechanisms in these novel materials. Firstly, the actual

shape of deformation defects should be considered accurately. In the theoretical and numerical studies, the shape of the deformation defects is usually considered as sphere, which has not been determined by the experiments or atomic simulations. It is necessary and meaningful to analyze what the shape of the deformation defect is, since the shape approximation on the deformation defects considered in our phase-field modeling was found to affect the deformation mechanisms of MGs. Secondly, the issues concerning the size effects on the mechanical properties of MGs, in particular the brittle-to-ductile transition in micro- or nano-scaled MGs, should be further studied. The critical size of MGs distinguishing the transition between the brittle and ductile plastic deformations is an important parameter influencing the application of MGs. Although the experiments have provided useful information on such critical size of MGs, the results were found to contradict with each other. Last but not least, the computational efficiency of phase-field modeling should be improved through introducing the parallel computing algorithms, to cope with the increasing sizes of the sample systems and enormous amount of degrees of freedoms in the governing equations. Thus in the future work, it is recommended to focus on the above-mentioned aspects to further understand the deformation mechanisms in MGs.

Bibliography

Allen, S.M. and Cahn, J.W., (1979), “A microscopic theory for antiphase boundary motion and its application to antiphase domain coarsening”, *Acta Metll.* 27: 1085-1095.

Apfel, R.E. and Qiu, N., (1996), "Principle of dynamic decompression and cooling for materials processing", *J. Mater. Res.* 11: 2916-2920.

Argon, A.S., (1979). "Plastic deformation in metallic glasses", *Acta Metall.* 27: 47-58.

Ashby, M.F., Evans, T., Fleck, N.A., Gibson, L.J., Hutchinson, L.W. and Wadley, H.N.G., (2000), Metal foams: a design guide. Butterworth-Heineman, Oxford, UK.

Ashby, M.F. and Greer, A.L., (2006), “Metallic glasses as structural materials”, *Scripta Mater.* 54: 321-326.

Bae, D.H., Park, J.M., Na, J.H., Kim, D.H., Kim, Y.C. and Lee, J.K., (2004), "Deformation behavior of Ti-Zr-Ni-Cu-Be metallic glass and composite in the supercooled liquid region", *J.Mater. Res.* 19: 937-942.

Bei, H., Xie, S. and George, E.P., (2006), "Softening caused by profuse shear banding

in a bulk metallic glass", *Phys. Rev. Lett.* 96: 105503.

Bennett, C.H., Chaudhari, P., Moruzzi, V. and Steinhardt, P., (1979), "On the stability of vacancy and vacancy clusters in amorphous solids", *Phil. Mag.* A 40: 485-495.

Bernal, J.D. and Mason, J., (1960), "Packing of spheres: co-ordination of randomly packed spheres", *Nature* 188: 910-911.

Bian, Z., Chen, G.L., He, G. and Hui, X.D., (2001), "Microstructure and ductile-brittle transition of as-cast Zr-based bulk glassy alloys under compressive testing", *Mater. Sci. Eng*. A316: 135-144.

Bletry, M., Guyot, P., Brechet, Y., Blandin, J.J. and Soubeyroux, J.L., (2004), "Homogeneous deformation of bulk metallic glasses in the super-cooled liquid state", *Mater. Sci. Eng.* A387-389: 1005-1011.

Brothers, A.H. and Dunand, D.C., (2004), "Syntactic bulk metallic glass foam", *Appl. Phys. Lett.* 84: 1108-1110.

Brothers, A.H. and Dunand, D.C., (2005a), "Plasticity and damage in cellular amorphous metals", *Acta Mater.* 53: 4427-4440.

Brothers, A.H., Scheunemann, R., DeFouw, J.D. and Dunand, D.C., (2005), "Processing and structure of open-celled amorphous metal foams", *Scripta*

Mater. 52: 335-339.

Brother, A.H. and Dunand, D.C., (2005b), "Ductile bulk metallic glass foams", *Adv. Mater.* 17: 484-486.

Brothers, A.H. and Dunand, D.C., (2006), "Amorphous metal foams", *Scripta Mater.* 54: 513-520.

Bruck, H.A., Christman, T., Rosakis, A.J. and Johnson, W.L., (1994), "Quasi-static constitutive behavior of $Zr_{41.25}Ti_{13.75}Ni_{10}Cu_{12.5}Be_{22.5}$ bulk amorphous alloys", *Scripta Metall. Et Mater*. 30: 429-434.

Cahn, J.W. and Hilliard, J.E., (1958), "Free energy of a nonuniform system. I. Interfacial free energy", *J. Chem. Phys.* 28: 258-267.

Cahn, J.W., (1961), "On spinodal decomposition", *Acta Metall*. 9: 795-801.

Cahn, J.W., (1962), "On spinodal decomposition in cubic crystals", *Acta Metall.* 10: 179-183.

Cahn, J.W., (1965), "Phase separation by spinodal decomposition in isotropic systems", *J. Chem. Phys.* 42: 93-99.

Cao, Q.P., Li, J.F., Zhou, Y.H., Horsewell, A. and Jiang, J.Z., (2005). "Free-volume evolution and its temperature dependence during rolling of $Cu_{60}Zr_{20}Ti_{20}$ bulk metallic glass." *Appl. Phys. Lett.* 87: 101901.

Chaudhari, P., Levi, A. and Steinhardt, P., (1979), "Edge and screw dislocations in an amorphous solid", *Phys. Rev. Lett*. 43: 1517-1520.

Chen, H.S., (1978), "The influence of structural relaxation on the density and Young's modulus of metallic glasses", *J. Appl. Phys*. 49: 3289-3291.

Chen, H., He, Y., Shiflet, G.J. and Poon, S.J., (1994), "Deformation-induced nanocrystal formation in shear bands of amorphous alloys", *Nature* 367: 541-543.

Chen, G., Bei, H., Cao, Y., Liu, C.T. and George, E.P., (2009), "Ehanced plasticity in Zr-based bulk metallic glass composite with in situ formed intermetallic phases", *Appl. Phys. Lett*. 95: 081908.

Chen, C.Q., Pei, Y.T. and De Hosson, J.T.M., (2010), "Effects of size on the mechanical response of metallic glasses investigated through in situ TEM bending and compression experiments", *Acta Mater*. 58: 189-200.

Chen, C.Q., Pei, Y.T., Kuzmin, O., Zhang, Z.F., MA, E. and De Hosson, J.T.M., (2011), "Intrinsic size effects in the mechanical response of taper-free nanopillars of metallic glass", *Phys. Rev. B* 83: 180201.

Cheng, Y.Q., Han, Z., Li, Y. and Ma, E., (2009), "Cold verse hot shear banding in bulk metallic glass", *Phys. Rev. B* 80: 134115.

Cheng, S.C., Wang, X.L., Choo, H. and Liaw, P.K., (2007), “Global melting of $Zr_{57}Ti_5Ni_8Cu_{20}Zl_{10}$ bulk metallic glass under microcompression”, *Appl. Phys. Lett.* 91: 201917.

Chiang, C.L., Chu, J.P., Lo, C.T., Nieh, T.G.,Wang, Z.X. and Wang, W.H.(2004), "Homogeneous plastic deformation in a Cu-based bulk amorphous alloy", *Intermetallics* 12: 1057-1061.

Choi-Yim, H., Conner, R.D. and Johnson, W.L., (2005), "In situ composite formation in the Ni-(Cu)-Ti-Zr-Si system", *Scripta Mater.* 53: 1467-1470.

Chu, J.P., Chiang, C.L., Mahalingam, T. and Nieh, T.G., (2003), "Plastic flow and tensile ductility of a bulk amorphous $Zr_{55}Al_{10}Cu_{30}Ni_5$ alloy at 700K", *Scripta Mater.* 49: 435-440.

Chu, J.P., Chiang, C.L., Wijaya, H., Huang, R.T., Wu, C.W., Zhang, B., Wang, W.H. and Nieh, T.G., (2006), "Compressive deformation of a bulk Ce-based metallic glass", *Scripta Mater.* 55: 227-230.

Conner, R.D., Rosakis, A.J., Johnson, W.L. and Owen, D.M., (1997), “Fracture toughness determination for a beryllium-bearing bulk metallic glass”, *Scripta Mater*. 37: 1373-1378.

Conner, R.D., Dandliker, R.B. and Johnson, W.L., (1998), "Mechanical properties of

toungsten and steel fiber reinforced $Zr_{41.25}Ti_{13.75}Cu_{12.5}Ni_{10}Be_{22.5}$ metallic glass matrix composites", *Acta Mater.* 46: 6089-6102.

Dai, L.H., Yan, M., Liu, L.F. and Bai, Y.L., (2005), "Adiabatic shear banding instability in bulk metallic glasses", *Appl. Phys. Lett.* 87: 141916.

Das, J., Loser, W., Kuhn, U., Eckert, J., Roy, S.K. and Schultz, L., (2003), "High-strength Zr-Nb-(Cu, Ni, Al) composites with enhanced plasticity", *Appl. Phys. Lett*. 82: 4690-4692.

Delogu, F., (2009), "Molecular dynamic study of size effects in the compression of metallic glass nanowires", *Phys. Rev. B* 79: 184109.

Dubach, A., Raghavan, R., Loffler, J.F., Michler, J. and Ramamurty, U., (2009), "Micropillar compression studies on a bulk metallic glass in different structural states", *Scripta Mater*. 60: 567-570.

Eastgate, L.O., Sethna, J.P., Rauscher, M., Cretegny, T., Chen, C.-S. and Myers, C.R., (2002), "Fracture in mode I using a conserved phase-field model", *Phys. Rev. E* 65: 036117.

Egami, T., (1978), "Structural relaxation in amorphous $Fe_{40}Ni_{40}P_{14}B_6$ studied by energy dispersive X-ray diffraction", *J. Mater. Sci.* 13: 2587-2599.

Evans, A.G., Hutchinson, J.W. and Ashby, M.F., (1998), "Multifunctionality of

cellular metal system", *Prog. Mater. Sci*. 43: 171-221.

Falk, M.L. and Langer, J.S., (1998), "Dynamic of viscoplastic deformation in amorphous solids", *Phys. Rev. E* 57: 7192-7205.

Falk, M.L., Langer, J.S. and Pechenik, L., (2004), "Thermal effects in the shear-transformation-zone theory of amorphous plasticity: comparisons to metallic glass data", *Phys. Rev. E* 70: 011507.

Flores, K.M. and Dauskardt, R.H., (1999), "Local heating associated with crack tip plasticity in Zr-Ti-Ni-Cu-Be bulk amorphous metals", *J. Mater. Res.* 14: 638-643.

Flores, K.M., Suh, D., Dauskardt, R.H., Asoka-Kumar, P., Sterne, P.A. and Howell, R.H., (2002), "Characterization of free volume in a bulk metallic glass using positron annihilation spectroscopy", *J. Mater. Res.* 17: 1153-1161.

Frank, F.C., (1952), "A discussion on theory of liquids: supercooling of liquids", *Proc. R. Soc.* A215, 43-46.

Freund, L.B., (1990), *Dynamic fracture mechanics*, Cambridge University Press, Cambridge, UK.

Gibson, L.J. and Ashby, M.F., (1997), *Cellular solids: structure and properties*. 2nd ed. Cambridge University Press, Cambridge, UK.

Gilbert, C.J., Schroeder, V. and Ritchie, R.O., (1999), “Mechanisms for fracture and fatigue-crack propagation in a bulk metallic glass”, *Metall. Mater. Trans. A* 30: 1739-1753.

Gilman, J.J., (1973). "Flow via dislocations in ideal glasses." *J. Appl. Phys.* 44: 675-679.

Goodier, J.N., (1933), “Concentration of stress around spherical and cylindrical inclusions and flaws”, *J. Appl. Mech*. 55: 39-44.

Gu, X.J., McDermott, A.G., Poon, S.J. and Shiflet, G.J., (2006), "Critical poisson's ratio for plasticity in Fe-Mo-C-B-Ln bulk amorphous steel", *Appl. Phys. Lett*. 88: 211905.

Guo, S.F., Liu, L., Li, N. and Li, Y., (2010), "Fe-based bulk metallic glass matrix composite with large plasticity", *Scripta Mater.* 62: 329-332.

Guo, H., Yan, P.F., Wang, Y.B., Tan, J., Zhang, Z.F., Sui, M.L. and Ma, E., (2007), “Tensile ductility and necking of metallic glass”, *Nat. Mater*. 6: 735-739.

Gurtin, M.E., (2000), "On the plasticity of single crystals: free energy, micro-force, plastic-strain gradients", *J. Mech. Phys. Solids* 48: 989-1036.

Haasen, P., (1974). *Physikalische Metallkunde*, Kap. 8. Springer-Verlag.

Hall, E.O., (1951), “The deformation and ageing of mild steel: III Discussion of

Results", *Proc. Phys. Soc.* B64: 747-753.

Hays, C.C., Kim, C.P. and Johnson, W.L., (2000), "Microstructure controlled shear band pattern formation and enhanced plasticity of bulk metallic glasses containing *in situ* formed ductile phase dendrite dispersions", *Phys. Rev. Lett.* 84: 2901-2904.

Hays, C.C., Kim, C.P. and Johnson, W.L., (2001), "Improved mechanical behavior of bulk metallic glasses containing in situ formed ductile phase dendrite dispersions", *Mater. Sci. Eng*. A304-306: 650-655.

Han, Z., Wu, W.F., Li, Y., Wei, Y.J. and Gao, H.J., (2009), "An instability index of shear band for plasticity in metallic glasses", *Acta Mater.* 57: 1367-1372.

He, G., Eckert, J., Loser, W. and Schultz, L., (2003a), "Novel Ti-based nanostructure-dendrite composite with enhanced plasticity", *Nat. Mater*. 2: 33-37.

He, G., Zhang, Z.F., Loser, W., Eckert, J. and Schultz, L., (2003b), "Effect of Ta on glass formation, thermal stability and mechanical properties of a $Zr_{52.25}Cu_{28.5}Ni_{4.75}Al_{9.5}Ta_5$ bulk metallic glass", *Acta Mater*. 51: 2383-2395.

Huang, R., Suo, Z., Prevost, J.H. and Nix, W.D., (2002), "Inhomogeneous deformation in metallic glasses", *J. Mech. Phys. Solids* 50: 1011-1027.

Huang, Y., Cockayne, D.J.H., Marsh, C., Titchmarsh, J.M. and Petford-Long, A.K.,

(2005), “Self-organised amorphous material in silicon (001) by focused ion beam (FIB) system”, *Appl. Surf. Sci*. 252: 1954-1958.

Huang, J.C., Chu, J.P. and Jang, J.S.C., (2009), "Recent progress in metallic glasses in Taiwan", *Intermetallics* 17: 973-987.

Hofmann, D.C., Suh, J.Y., Wiest, A., Duan, G., Lind, M.L., Demetriou, M.D. and Johnson, W.L., (2008a), "Designing metallic glass matrix composites with high toughness and tensile ductility", *Nature* 451: 1085-1090.

Hofmann, D.C., Suh, J.Y., Wiest, A., Lind, M.L., Demetriou, M.D. and Johnson, W.L., (2008b), "Development of tough, low-density Titanium-based bulk metallic glass matrix composites with tensile ductility", *Proc. Nat. Acad. Sci. USA* 105: 20136-20140.

Hu, X., Ng, S.C., Feng, Y.P. and Li, Y., (2003), "Glass forming ability and in-situ composite formation in Pd- based bulk metallic glasses", *Acta Mater.* 51: 561-572.

Inoue, A., Zhang, T. and Masumoto, T., (1989), "Al-La-Ni amorphous alloys with a wide supercooled liquid region", *Mater. Trans., JIM* 30: 965-972.

Inoue, A., (2000), “Stabilization of metallic supercooled liquid and bulk amorphous alloys”, *Acta Mater*. 48: 279-306.

Inoue, A. and Takeuchi, A., (2004), “Recent progress on bulky glassy, nanoquasicrystalline and nanocrystalline alloys”, *Mater. Sci. Eng. A*375-377: 16-30.

Inoue, A., (2005), “Bulk glassy and nonequilibrium crystalline alloys by stabilization of supercooled liquid: fabrication, functional properties and applications”, *Proc. Japan Acad 81(B)*: 172-188.

Inoue, A., Wada, T. and Louzguine-Luzgin, D.V., (2007), "Improved mechanical properties of bulk glassy alloys containing spherical pores", *Mater. Sci. Eng. A* 471: 144-150.

Jang, D.C. and Greer, J.R., (2010), “Transition from a strong-yet-brittle to a stronger-and-ductile state by size reduction of metallic glasses”, *Nat. Mater*. 9: 215-219.

Jayaraj, J., Park, B.J., Kim, D.H., Kim, W.T. and Fleury, E., (2006), “Nanometer-sized porous Ti-based metallic glass”, *Scripta Mater.* 55: 1063-1066.

Johnson, W.L., (1998), "Bulk glass-forming metallic alloys: science and technology", [1998 Mrs Medal Award Lecture, Presented at Symposium Mm]. *MRS Proceedings* 554: 311-342.

Johnson, W.L., Lu, J. and Demetriou, M.D., (2002), "Deformation and flow in bulk

metallic glasses and deeply undercooled glass forming liquids- a self consistent dynamic free volume model", *Intermetallics* 10: 1039-1046.

Johnson, W.L., (2002). "Bulk amorphous metal- an emerging engineering material", *JOM*, 54: 40-43.

Kanungo, B.P., Lambert, M.J. and Flores, K.M., (2003). "Free volume changes and crack tip deformation in bulk metallic glass alloys and their composites." *MRS Proceedings* 806: MM7.1.

Karma, A., Kessler, D.A. and Levine, H., (2001), "Phase-field model of mode III dynamic fracture", *Phys. Rev. Lett.* 87: 045501.

Karama, A. and Lobkovsky, A.E., (2004), "Unsteady crack motion and branching in a Phase-field model of brittle fracture", *Phys. Rev. Lett*. 92: 245510.

Kato, N.I., (2004), "Reducing focused ion beam damage to transmission electron microscopy samples", *J. Electron Microsc*. 53: 451-458.

Kawamura, Y., Shibata, T., Inoue, A. and Masumoto, T., (1996), "Deformation behavior of $Zr_{65}AL_{10}Ni_{10}Cu_{15}$ glassy alloy with wide supercooled liquid region", *Appl. Phys. Lett.* 69: 1208-1210.

Kessler, D.A., Koplik, J. and Levine, H., (1988), "Pattern selection in fingered growth phenomena", *Adv. Phys.* 37: 255-339.

Khonik, V.A. and Spivak, L.V., (1996), “On the nature of low temperature internal friction peaks in metallic glasses”, *Acta Mater.* 44: 367-381.

Khonik, V.A., (1996), “Internal friction of metallic glasses: mechanisms and conditions of their realization”, *J. De Phys. IV France* 6: 591 -600.

Khonik, S.V., Granato, A.V., Joncich, D.M., Pompe, A. and Khonik, V.A., (2008), “Evidence of distributed interstitialcy-like relaxation of the shear modulus due to structural relaxation of metallic glasses”, *Phys. Rev. Lett*. 100: 065501.

Kim, D.K. and Okazaki, K., (1992), “Nano-crystalline consolidation of MA powders by EDC”, *Mater. Sci. Forum* 88-90: 553-560.

Klement, W., Willens, R.H. and Duwez, P., (1960), “Non-crystalline structure in solidified gold-silicon alloys”, *Nature* 187: 869-870.

Krishnanand, K.D. and Cahn, R.W., (1975), "Recovery from plastic deformation in a Ni/Nb alloy glass", *Scripta Metall.* 9: 1259-1261.

Kuhn, U., Eckert, J., Mattern, N. and Schultz, L., (2002), "ZrNbCuNiAl bulk metallic glass matrix composites containing dendritic bcc phase precipitates", *Appl. Phys. Lett.* 80: 2478-2480.

Kunzi, H.U., Agyeman, K. and Guntherodt, H.J., (1979), “Internal friction peaks in metallic glasses”, *Solid State Commun.* 32: 711-714.

Ladadwa, I. and Teichler, H., (2006), “Low-frequency dynamical heterogeneity in simulated amorphous $Ni_{0.5}Zr_{0.5}$ below its glass temperature: Correlations with cage volume and local order fluctuations”, *Phys. Rev. E* 73: 031501.

Lai, Y.H., Lee, C.J., Cheng, Y.T., Chou, H.S., Du, X.H., Chang, C.I., Huang, J.C., Jian, S.R., Jang, J.S.C. and Nieh, T.G., (2008), “Bulk and microscale compressive behavior of a Zr-based metallic glass”, *Scripta Mater.* 58: 890-893.

Landau, L. D. (1937a). “Theory of phase transformations. I”, Phys. Z. Sowjun. 11, 26-30.

Landau, L. D. (1937b). “Theory of phase transformations. II”, Phys. Z. Sowjun. 11, 545-549.

Langer, J.S. (1980), “Instabilities and pattern formation in crystal growth”, *Rev. Mod. Phys.* 52: 1-28.

Langer, J.S., (2006), “Shear-transformation-zone theory of deformation in metallic glasses”, *Scripta Mater.* 54: 375-379.

Langford, R.M., (2006), “Focused ion beams techniques for nanomaterials characterization”, *Microsc. Res. Tech*. 69: 538-549.

Leamy, H.J., Chen, H.S. and Wang, T.T., (1972), "Plastic flow and fracture of metallic

glass", *Metall. Trans.* 3: 699-708.

Lee, M.L., Li, Y. and Schuh, C.A., (2004), "Effect of a controlled volume fraction of dendritic phases on tensile and compressive ductility in La-based metallic glass matrix composites", *Acta Mater.* 52: 4121-4131.

Lee, M.H. and Sordelet, D.J., (2006), "Nanoporous metallic glass with high surface area", *Scripta Mater.* 55: 947-950.

Lee, C.J., Huang, J.C. and Nieh, T.G., (2007), "Sample size effect and microcompression of $Mg_{65}Cu_{25}Gd_{10}$ metallic glass", *Appl. Phys. Lett.* 91: 161913.

Lewandowski, J.J., Shazly, M. and Nouri, A.S., (2006), "Intrinsic and extrinsic toughening of metallic glasses", *Scripta Mater.* 54: 337-341.

Li, Q.K. and Li, M., (2005), "Effects of surface imperfection on deformation and failure of amorphous metals", *Appl. Phys. Lett*. 87: 031910.

Li, Q.K. and Li, M., (2006), "Molecular dynamic simulation of intrinsic and extrinsic mechanical properties of amorphous metals", *Intermetallics* 14: 1005-1010.

Li, Q.K. and Li, M., (2007), "Assessing the critical sizes for shear band formation in metallic glasses from molecular dynamics simulation", *Appl. Phys. Lett*. 91:

231905.

Li, J., Wang, Z.L. and Hufnagel, T.C., (2002), “Characterization of nanometer-scale defects in metallic glasses by quantitative high-resolution transmission electron microscopy”, *Phys. Rev. B* 65: 144201.

Liu, L., Chan, K.C., Sun, M. and Chen, Q., (2007), "The effect of the addition of Ta on the structure, crystallization and mechanical properties of Zr-Cu-Ni-Al-Ta bulk metallic glasses", *Mater. Sci. Eng. A* 445-446: 697-706.

Liu, C.T., Heatherly, L., Easton, D.S., Carmichael, C.A., Schneibel, J.H., Chen, C.H., Wright, J.L., Yoo, M.H., Horton, J.A. and Inoue, A., (1998), "Test environment and mechanical properties of Zr-based bulk amorphous alloys", *Metall. Mater. Trans.* A 29: 1811-1820.

Liu, Y.H., Wang, D., Nakajima, K., Zhang, W., Hirata, A., Nishi, T., Inoue, A. and Chen, M.W., (2011), “Characterization of nanoscale mechanical heterogeneity in a metallic glass by dynamic force microscopy”, *Phys. Rev. Lett*. 106: 125504.

Louzguine, D.V., Kato, H. and Inoue, A., (2004), “High strength and ductile binary Ti-Fe composite alloy”, *J. Alloys Compd*. 384: L1-L3.

Lowhaphandu, P. and Lewandowski, J.J., (1998), “Fracture toughness and notched toughness of bulk amorphous alloy: Zr-Ti-Ni-Cu-Be”, *Scripta Mater*. 38:

1811-1817.

Lu, J., Ravichandran, G. and Johnson, W.L., (2003), “Deformation behavior of the $Zr_{41.2}Ti_{13.8}Cu_{12.5}Ni_{10}Be_{22.5}$ bulk metallic glass over a wide range of strain-rates and temperatures”, *Acta Mater*. 51: 3429-3443.

Luo, J.H., Wu, F.F., Huang, J.Y., Wang, J.Q. and Mao, S.X., (2010), “Superelongation and atomic chain formation in nanosized metallic glass”, *Phys. Rev. Lett.* 104: 215503.

Ma, Y., Cao, Q.P., Qu, S.X., Zhang, D.X., Wang, X.D. and Jiang, J.Z., (2012), “Stress-state-dependent deformation behavior in Ni-Nb metallic glassy film”, *Acta Mater.* 60: 4136-4143.

Manning, M.L., Langer, J.S. and Carlson, J.M., (2007), "Strain localization in a shear transformation zone model for amorphous solids", *Phys. Rev. E* 76: 056106.

Mukai, T., Nieh, T.G., Kawamura, Y., Inoue, A. and Higashi, K., (2002b), "Effects of strain rate on compressive behavior of $Pd_{40}Ni_{40}P_{20}$ bulk metallic glass", *Intermetallics* 10: 1071-1077.

Mukai, T., Nieh, T.G., Kawamura, Y. , Inoue, A. and Higashi, K., (2002a), "Dynamic response of a $Pd_{40}Ni_{40}P_{20}$ bulk metallic glass in tension", *Scripta Mater.* 46: 43-47.

Nieh, T.G., Mukasi, T., Liu, C.T. and Wadsworth, J., (1999), "Superplastic behavior of a Zr-10Al-5Ti-17.9Cu-14.6Ni metallic glass in the supercooled liquid region", *Scripta Mater.* 40: 1021-1027.

Nishiyama, N., Amiya, K., Inoue, A., (2007), "Novel application of bulk metallic glass for industrial products", *J. Non-Cryst. Solids* 353: 3615-3621.

Onsager, L., (1931a), "Reciprocal relations in irreversible processes. I", *Phys. Rev.* 37: 405-426.

Onsager, L., (1931b), "Reciprocal relations in irreversible processes. II", *Phys. Rev.* 38: 2265-2279.

Pampillo, C.A., (1975), "Flow and fracture in amorphous alloys", *J. Mater. Sci.* 10: 1194-1227.

Pekarskaya, E., Kim, C.P. and Johnson, W.L., (2001), "In situ transmission electron microscopy studies of shear bands in a bulk metallic glass based composite", *J. Mater. Res*. 16: 2513-2518.

Provatas, N. and Elder, K., (2010), *Phase-field methods in materials science and engineering*, Wiley, Weinheim, Germany.

Raabe, D., (1998), *Computational materials science: the simulation of materials mocrostructures and properties*. Wiley-VCH Verlag GmbH. D-69469

Weinheim.

Rao, X., Si, P.C., Wang, J.N., Xu, S., Wang, W.M. and Wang, W.H., (2001), “Preparation and mechanical properties of a new Zr-Al-Ti-Cu-Ni-Be bulk metallic glass”, *Mater. Lett*. 50: 279-283.

Reger-Leonhard, A., Heilmaier, M. and Eckert, J., (2000), "Newtonian flow of $Zr_{55}Cu_{30}Al_{10}Ni_5$ bulk metallic glassy alloys", *Scripta Mater.* 43: 459-464.

Saotome, Y., Hatori, T., Zhang, T. and Inoue, A., (2001a), "Superplastic micro/nano-formability of $La_{60}Al_{20}Ni_{10}Co_5Cu_5$ amorphous alloy in supercooled liquid state", *Mater. Sci. Eng*. A304: 716-720.

Saotome, Y., Itoh, K., Zhang, T. and Inoue, A., (2001b), "superplastic nanoforming of Pd-based amorphous alloy", *Scripta Mater.* 44: 1541-1545.

Schroers, J., Veazey, C. and Johnson, W.L., (2003), "Amorphous metallic foam", *Appl. Phys. Lett.* 82: 370-372.

Schroers, J., Veazey, C., Demetriou, M.D. and Johnson, W.L., (2004), “Synthesis method for amorphous metallic foam”, *J. Appl. Phys*. 96: 7723-7730.

Schroers, J., Lohwongwatana, B., Johnson, W.L. and Peker, A., (2007), "Precious bulk metallic glasses for jewelry applications", *Mater. Sci. Eng. A* 449-451: 235-238.

Schroers, J., Kumar, G., Hodges, T.M., Chan, S. and Kyriakides, T.R., (2009), "Bulk metallic glasses for biomedical applications", *JOM* 61: 21-29.

Schuh, C.A. and Lund, A.C., (2003), "Atomistic basis for the plastic yield criterion of metallic glass", *Nat Mater.* 2: 449-452.

Schuh, C.A., Hufnagel, T.C. and Ramamurty, U., (2007), "Mechanical behavior of amorphous alloys", *Acta Mater.* 55: 4067-4109.

Schuster, B.E., Wei, Q., Hufnagel, T.C. and Ramesh, K.T., (2008), "Size-independent strength and deformation mode in compression of a Pd-based metallic glass", *Acta Mater*. 56: 5091-5100.

Scott. G.D., (1960), "Packing of spheres: Packing of equal spheres", Nature 188: 908-909.

Shan, Z.W., Li, J., Cheng, Y.Q., Minor, A.M., Syed Asif., S.A., Warren, O.L. and Ma, E., (2008), "Plastic flow and failure resistance of metallic glass: Insight from *in situ* compression of nanopillars", *Phys. Rev. B* 77: 155419.

Shen, Y. and Zheng, G.P., (2010), "Modeling of shear band multiplication and interaction in metallic glass matrix composite", *Scripta Mater.* 63: 181-184.

Shen, Y., (2013), *Characterization of deformation defects in metallic glasses and metallic glass composites: from experiment to computer modeling*. Ph.D thesis.

The HongKong Polytechnic University.

Shi, L.T., (1986), “Dislocation-like defects in an amorphous Lennard-Jones solid”, *Mater. Sci. Eng*. 81: 509-514.

Sieradzki, K., Rinaldi, A. Friesen, C. and Peralta, P., (2006), “Length scales in crystal plasticity”, *Acta Mater*. 54: 4533-4538.

Spaepen, F., (1977). "A microscopic mechanism for steady state inhomogeneous flow in metallic glasses", *Acta Metall.* 25: 407-415.

Steif, P.S., Spaepen, F. and Hutchinson, J.W., (1982), “Strain localization in amorphous metals”, *Acta. Metall.* 30: 447-455.

Sun, G.Y., Chen, G., Liu, C.T. and Chen, G.L., (2006), "Innovative processing and property improvement of metallic glass based composites", *Scripta Mater.* 55: 375-378.

Sun, G.Y., Chen, G. and Chen, G.L., (2007), "Comparison of microstructures and properties of Zr-based bulk metallic glass composites with dendritic and spherical bcc phase precipitates", *Intermetallics* 15: 632-634.

Szuecs, F., Kim, C.P. and Johnson, W.L., (2001), "Mechanical properties of $Zr_{56.2}Ti_{13.8}Nb_{5.0}Cu_{6.9}Ni_{5.6}Be_{12.5}$ ductile phase reinforced bulk metallic glass composite", *Acta Mater.* 49: 1507-1513.

Tabor, D., (1951), “The hardness and strength of metals”, *J. Inst. Metals* 79: 1-18.

Tan, H., Zhang, Y. and Li, Y., (2002),"Synthesis of La-based in-situ bulk metallic glass matrix composite", *Intermetallics* 10: 1203-1205.

Takeuchi, S., Kamimura, Y., Yoshihara, T. and Edagawa, K., (2010), “Propagation of shear transformation zone at sound velocity in metallic glass”, *Suppl. Proc. Vol. 2: materials characterization, computation, modeling and energy. TMS*: 53-60.

Thamburaja, P. and Ekambaram, R., (2007), "Coupled thermo-mechanical modelling of bulk-metallic glasses: theory, finite-element simulations and experimental verification", *J. Mech. Phys. Solids* 55: 1236-1273.

Volkert, C.A., Donohue, A. and Spaepen, F., (2008), “Effects of sample size on deformation in amorphous metals”, *J. Appl. Phys.* 103: 083539.

Wada, T. and Inoue, A., (2003), “Fabrication, thermal stability and mechanical properties of porous bulk glassy Pd-Cu-Ni-P alloys”, *Mater. Trans., JIM* 44: 2228-2231.

Wada, T., Takenaka, K., Nishiyama, N. and Inoue, A., (2005), "Formation and mechanical properties of porous Pd-Pt-Cu-P bulk glassy alloys", *Mater. Trans*., *JIM* 46: 2777-2780.

Wada, T., Qin, F. X., Wang, X.M., Inoue, A. and Yoshimura, M., (2007), “Preparation

of open-cell porous Zr-based bulk glassy alloy", *Mater. Trans., JIM* 48: 2381-2384.

Wang, Y.U., Jin, Y.M., Cuitino, A.M. and Khachaturyan, A.G., (2001), "Nanoscale phase field microelasticity theory of dislocations: model and 3D simulation", *Acta Mater*. 49: 1847-1857.

Wang, W.H., Dong, C. and Shek, C.H., (2004), "Bulk metallic glasses", *Mater. Sci. Eng. R* 44: 45-89.

Wang, J.T., Hodgson, P.D., Zhang, J.D., Yan, W.Y. and Yang, C.H., (2010), "Effects of pores on shear bands in metallic glasses: A molecular dynamics study", *Comput. Mater. Sci.* 50: 211-217.

Wright, W.J., Saha, R. and Nix, W.D., (2001), "Deformation mechanisms of the $Zr_{40}Ti_{14}Ni_{10}Cu_{12}Be_{24}$ bulk metallic glass", *Mater. Trans., JIM.* 42: 642-649.

Wu, F.F., Zhang, Z,F, Shen, B.L., Mao, S.X.Y. and Eckert, J., (2008), "Size effect on shear fracture and fragmentation of a $Fe_{57.6}Co_{14.4}B_{19.2}Si_{4.8}Nb_4$ bulk metallic glass", *Adv. Eng. Mater.* 10: 727-730

Wu, W.F., Han, Z. and Li, Y., (2008), "Size-dependent 'malleable-to-brittle' transition in a bulk metallic glass", *Appl. Phys. Lett.* 93: 061908.

Wu, F.F., Zhang, Z.F. and Mao, S.X., (2009), "Size-dependent shear fracture and

global tensile plasticity of metallic glasses", *Acta Mater.* 57: 257-266.

Wu, X.L., Guo, Y.Z., Wei, Q. and Wang, W.H., (2009), "Prevalence of shear banding in compression of $Zr_{41}Ti_{14}Cu_{12.5}Ni_{10}Be_{22.5}$ pillars as small as 150 nm in diameter", *Acta Mater.* 57: 3562-3571.

Wu, Y., Li, H.X., Liu, Z.Y., Chen, G.L. and Lu, Z.P., (2010a), "Interpreting size effects of bulk metallic glasses based on a size-independent critical energy density", *Intermetallics* 18: 157-160.

Wu, Y., Wu, H.H., Hui, X.D., Chen, G.L. and Lu, Z.P., (2010b), "Effects of drawing on the tensile fracture strength and its reliability of metallic glasses", *Acta Mater*. 58: 2564-2576.

Yang, Y., Zeng, J.F., Volland, A., Blandin, J.J., Gravier, S. and Liu, C.T., (2012), "Fractal growth of the dense-packing phase in annealed metallic glass imaged by high-resolution atomic force microscopy", *Acta Mater.* 60: 5260-5272.

Yao, K.F. and Zhang, C.Q., (2007), "Fe-based bulk metallic glass with high plasticity", *Appl. Phys. Lett.* 90: 061901.

Yoo, B.G., Park, K.W., Lee, J.C., Ramamurty, U. and Jang, J.I., (2009), "Role of free volume in strain softening of as-cast and annealed bulk metallic glass", *J. Mater. Res*. 24: 1405-1416.

Yu, H.B., Hu, J., Xia, X.X., Sun, B.A., Li, X.X., Wang, W.H. and Bai, H.Y., (2009), "Stress-induced structural inhomogeneity and plasticity of bulk metallic glasses", *Scripta Mater.* 61: 640-643.

Yuan, C.C. and Xi, X.K., (2011), "On the correlation of Young's modulus and the fracture strength of metallic glasses", *J. Appl. Phys.* 109: 033515.

Zhang, Z.F., Eckert, J. and Schultz, L., (2003), "Difference in compressive and tensile fracture mechanisms of $Zr_{59}Cu_{20}Al_{10}Ni_8Ti_3$ bulk metallic glass", *Acta Mater.* 51: 1167-1179.

Zheng, G.P. and Li. M., (2009). "Mesoscopic theory of shear banding and crack propagation in metallic glasses", *Phys. Rev. B* 80: 104201.

Zheng, G. P., (2011), "Application of phase-field modeling to deformation of metallic glasses", *Current Opinion Solid State Mater. Sci.* 15: 116-124.

Zhou, N, Shen, C., Mills, M. and Wang, Y.Z., (2010), "Large-scale three-dimensional phase field simulation of γ' –rafting and creep deformation", *Phil. Mag.* 90: 405-436.

Ziman, J.M., (1961), "A theory of the electrical properties of liquid metals. I: The monovalent metals", *Philos. Mag.* 6: 1013-1034.